JUACEP Summer Program
2024
at Nagoya University

Japan-US-Canada Collaborative Education Program

Nagoya University

Table of Contents

<1> About the Program

1-1 Overview

Summary 10-week course 2024 for the students from University of Michigan, UCLA, North Carolina State University, New York University and Polytechnique Montréal

Duration: June 3 – August 30, 2024
Research presentations: The 33rd JUACEP Workshop on August 8 & 29, 2024

This program is designed for graduate students from our partner universities in US and Canada, and in 2024, 14 students participated. Among them, four students were from North Carolina State University (NCSU), three from University of Michigan (UM), four from New York University (NYU), two from Polytechnique Montréal (PolyMTL) and one from UCLA.

Each participant chose a research laboratory at Nagoya University in accordance with his/her research interest and carried out a research project under the supervisor of the laboratory. Japanese language class, the hands-on engine-model assembly course, excursion and some special events were organized for the program.

During the program period, they took part in the labs' activities such as seminars, sessions, trips, casual parties and so on. Teaching Assistants (TA) assigned by the program supported the participants not only in research scenes but also in daily life.

At the end of the program, each student submitted a research report to respective supervisors and gave a final presentation at the 33rd JUACEP Workshop held at the TEL Auditorium on campus. The reports and presentations were evaluated by their respective supervisors and students were awarded credits by Nagoya University.

Workshop on Aug.9 for Track A

Workshop on Aug. 25 for Track B

1−2 Participants from the Partner Universities

	Name	Adviser & Teaching Assistant at NU
Track A. June 3 - Aug 9, 2024		
1	Jacob KOKINDA Electrical Eng., NCSU	Prof. Norihiko NISHIZAWA, Electronics TA: Rongjie ZHANG
2	James FERNANDEZ Aerospace Eng., NCSU	Prof. Jiro KASAHARA, Aerospace Eng. TA: Soa YAMADA
3	Melody POLK Nuclear Eng., NCSU	Prof. Hideki TOMITA, Applied Energy TA: Erika TAKAYAMA
4	Seoyeong PARK Computer Science, NCSU	Prof. Nobuo KAWAGUCHI, Information & Communication Eng. TA: Yuya AIKAWA
5	Utkarsh SRIVASTAVA Computer Eng., NYU	Prof. Toshiaki FUJII, Information & Communication Eng. TA: Yanbo LI
6	Maria ACUÑA Mechanical Eng., NYU	Assoc. Prof. Kiyoshi KINEFUCHI, Aerospace Eng. TA: Azumi MIYAZAKI
7	Raphaël PLANTE Mechanical Eng., PolyMTL	Prof. Toshiro MATSUMOTO, Mechanical Systems Eng. TA: Ryoji ITOYAMA
8	Mohamed DIOP Mechanical Eng., PolyMTL	Prof. Akinori YOSHIMURA, Aerospace Eng. TA: Chihaya HOSHIKAWA
9	Edith SHEAR Aerospace Eng., UM	Assoc. Prof. Kiyoshi KINEFUCHI, Aerospace Eng. TA: Ryota NAKANO
10	Xiaoyue (Luna) WU Mechanical Eng., UM	Assoc. Prof. Keisuke FUJII, Intelligent Systems* TA: Sota NAKANISHI
11	Gavin SILVEIRA Energy Systems Eng., UM	Prof. Takeyoshi KATO, Electrical Eng. TA: Shinya ATSUMI
Track B. June 17 - Aug 30, 2024		
12	Oscar ABREU Computer Eng., NYU	Assoc. Prof. Keisuke FUJII, Intelligent Systems* TA: Kenjiro IDE
13	Yukteshwar RAVI Mechatronics / Robotics Eng., NYU	Prof. Tsuyoshi INOUE, Mechanical Systems Eng. TA: Izuru NAITO
14	Rosemary HE Computer Science, UCLA	Prof. Ichiro TAKEUCHI, Mechanical Systems Eng. TA: Yoshito OKURA

*Graduate School of Informatics

Coordinators of Partner Universities

Prof. Jenn-Ming YANG	UCLA Samueli School of Engineering
Prof. Katsuo KURABAYASHI	NYU Tandon School of Engineering
Prof. Kazu SAITOU	Mechanical Engineering, University of Michigan
Mr. Tomohisa KOYAMA	Executive Director, NU Tech at North Carolina
Ms. Delphine JULEN	Polytechnique Montréal International (POINT)

Japanese Course Instructor

Ms. Sumie YASUI

JUACEP Members

Prof. Noritsugu UMEHARA	noritsugu.umehara@mae.nagoya-u.ac.jp
Prof. Toshiro MATSUMOTO	matsumoto.toshiro.e6@f.mail.nagoya-u.ac.jp
Prof. Yasumasa ITO	ito.yasumasa.y3@f.mail.nagoya-u.ac.jp
Assoc.Prof. Takayuki TOKOROYAMA	takayuki.tokoroyama@mae.nagoya-u.ac.jp
Assoc.Prof. Reiko FURUYA	furuya.reiko.n5@f.mail.nagoya-u.ac.jp
Assoc.Prof. Gang ZENG	zeng.gang.s6@f.mail.nagoya-u.ac.jp
Assoc.Prof. Emanuel LELEITO	leleito@nagoya-u.jp
Administrative staff Tomoko KATO	kato.tomoko.e6@f.mail.nagoya-u.ac.jp

JUACEP Office

Room #341, Engineering Building II Phone +81 (0)52-789-2799

JUACEP Summer Program 2024 Schedule

A	B	Date		8:45-10:15	10:30-12:00		13:00-14:30	14:45-16:15	16:30
1		June 2	Sun				[A] Arrival at Nagoya, stay at a hotel		
2		June 3	Mon		[A] Orientation		Allocation to each lab	15:30 Check-in at the Dorm	
3		June 4	Tue	Reseach at each lab			Research at each lab		
4		June 5	Wed						
5		June 6	Thu						
6		June 7	Fri						
7		June 8	Sat						
8		June 9	Sun						
9		June 10	Mon	Reseach at each lab			Research at each lab		
10		June 11	Tue						
11		June 12	Wed						
12		June 13	Thu						
13		June 14	Fri						
14		June 15	Sat						
15	1	June 16	Sun				[B] Arrival at Nagoya, stay at a hotel		
16	2	June 17	Mon		[B] Orientation	Lunch	Allocation to each lab	15:30 Check-in at the Dorm	
17	3	June 18	Tue	Reseach at each lab			13:45-16:15 JP Class (1)		Research at each lab
18	4	June 19	Wed						
19	5	June 20	Thu				13:45-16:15 JP Class (2)		Meet-up
20	6	June 21	Fri						
21	7	June 22	Sat						
22	8	June 23	Sun						
23	9	June 24	Mon	Reseach at each lab					
24	10	June 25	Tue				13:45-16:15 JP Class (3)		Research at each lab
25	11	June 26	Wed						
26	12	June 27	Thu				13:45-16:15 JP Class (4)		
27	13	June 28	Fri	Excursion					
28	14	June 29	Sat						
29	15	June 30	Sun						
30	16	July 1	Mon	Reseach at each lab					
31	17	July 2	Tue				Stipend 13:45-16:15 JP Class (5)		Research at each lab
32	18	July 3	Wed						
33	19	July 4	Thu				13:45-16:15 JP Class (6)		
34	20	July 5	Fri				Hands-on Workshop for Group 1		
35	21	July 6	Sat						
36	22	July 7	Sun						
37	23	July 8	Mon	Reseach at each lab			Hands-on Workshop for Group 2		
38	24	July 9	Tue				13:45-16:15 JP Class (7)		Research at each lab
39	25	July 10	Wed						
40	26	July 11	Thu				13:45-16:15 JP Class (8)		
41	27	July 12	Fri						
42	28	July 13	Sat						
43	29	July 14	Sun						
44	30	July 15	Mon	(Mrine day)					
45	31	July 16	Tue	Reseach at each lab			13:45-16:15 JP Class (9)		Research at each lab
46	32	July 17	Wed						
47	33	July 18	Thu				13:45-16:15 JP Class (Fin)		
48	34	July 19	Fri						
49	35	July 20	Sat						
50	36	July 21	Sun						
51	37	July 22	Mon	Reseach at each lab			Reseach at each lab		
52	38	July 23	Tue						
53	39	July 24	Wed						
54	40	July 25	Thu						
55	41	July 26	Fri						
56	42	July 27	Sat						
57	43	July 28	Sun						
58	44	July 29	Mon	Reseach at each lab			Research at each lab		
59	45	July 30	Tue						
60	46	July 31	Wed						
61	47	Aug. 1	Thu						
62	48	Aug. 2	Fri				Stipend		
63	49	Aug. 3	Sat						
64	50	Aug. 4	Sun						
65	51	Aug. 5	Mon	Submitting (1)Research report, (2)JASSO questionnaires, (3)Findings report					
66	52	Aug. 6	Tue	Research at each lab			Research at each lab		
67	53	Aug. 7	Wed						
68	54	Aug. 8	Thu	Research & Reflection @ each Lab			[A] Final Workshop I		Farewell banquiet
69	55	Aug. 9	Fri	[A] Check out from the dorm					
69	56	Aug. 10	Sat	Obon Holidays					
	64	Aug. 18	Sun						
	65	Aug. 19	Mon	Reseach at each lab			Reseach at each lab		
	66	Aug. 20	Tue						
	67	Aug. 21	Wed						
	68	Aug. 22	Thu						
	69	Aug. 23	Fri						
	70	Aug. 24	Sat						
	71	Aug. 25	Sun						
	72	Aug. 26	Mon	Submitting (1)Research report, (2)JASSO questionnaires, (3)Findings report					
	73	Aug. 27	Tue	Research at each lab			Research at each lab		
	74	Aug. 28	Wed						
	75	Aug. 29	Thu	[B] Final Workshop II			Research & Reflection @ each Lab		
	76	Aug. 30	Fri	[B] Check out from the dorm					

Track A	Track B	Both tracks	Holiday

<2> Research Achievements

2-1. Research Internship

Research Reports

2-2. Presentations

ALL-PM TM-DOPED ULTRA SHORT PULSE FIBER LASER USING SWNT

Kokinda, Jacob

Department of Electrical and Computer Engineering, North Carolina State University
jkokind@ncsu.edu

Supervisor: Nishizawa, Norihiko

Graduate School of Engineering, Nagoya University
nishizawa@NUEE.nagoya-u.ac.jp

ABSTRACT

Ultrashort pulse lasers, which generate femtosecond-duration pulses through mode-locking techniques, have revolutionized various fields due to their high peak power and broad spectral bandwidth. However, the development of polarization-maintaining (PM) fiber lasers at longer wavelengths (near to mid-infrared) remains challenging due to the difficulty in manufacturing PM components for these wavelengths. This research aims to address this challenge by developing the first all-PM Tm-doped fiber laser using single-walled carbon nanotubes (SWNTs), targeting applications like optical coherence tomography (OCT). This study builds upon the first all-PM Er-doped fiber laser operating at 1.55 µm and extends the technology to around the 2-µm range. The all-PM Tm-doped fiber laser was successfully developed, maintaining stable ultrashort pulses with the necessary large spectral bandwidth for OCT. The creation of an all-PM Tm-doped fiber laser at 2 µm marks a significant advancement in ultrashort pulse laser technology. This development opens new avenues for high-resolution OCT and other applications requiring robust, high-performance lasers in the near to mid-infrared spectrum, addressing a critical need in both research and clinical settings.

1. INTRODUCTION

Ultrashort pulse lasers represent a significant advancement in laser technology. These lasers generate pulses with durations in the femtosecond (10^-15 seconds) range, through the use of mode-locking techniques. Mode locking refers to the process of different frequency modes of the laser phase-locking together, resulting in the creation of pulses of light that are extremely short in duration. The short pulse duration allows for high peak powers while maintaining a relatively low average power. Another key characteristic of these lasers is linked to the Uncertainty Principle which states that time and energy are conjugate variables. It is known that this relationship infers that the shorter the pulse width in time, the larger the width in the spectral dimension. This is important for these lasers as their short pulse durations necessitate large bandwidths. Their high peak power and large spectral bandwidth make them suitable for a wide range of applications, including medical imaging and surgery, spectroscopic research and telecommunications. More specifically for medical imaging, multi-photon microscopy and optical coherence tomography each require one of the two key characteristics of ultra short pulse lasers.

Optical fiber cavities play a crucial role in the development of ultrashort pulse lasers. The use of optical fibers offers several advantages over traditional solid-state and gas laser cavities, including compactness, flexibility, and efficient heat dissipation. Optical fibers can be doped with rare-earth elements to create gain media that amplifies laser light. The fiber cavity design can be optimized to support the desired mode-locking mechanism, such as nonlinear polarization rotation or the use of saturable absorbers, which are essential for generating stable and repeatable ultrashort pulses [1].

Pulse quality and stability can be significantly impacted through any changes in the polarization of the laser light commonly caused by the natural birefringence of the material. Possible negative effects are pulse distortion, loss of mode-locking, etc. One way to avoid these issues is to utilize polarization maintaining fibers. As the name suggests, the fiber mitigates the effects of birefringence. This is done by purposefully manufacturing optical axes that have a vastly different propagation constant so that the normal disturbances cannot couple one propagation mode into the other, effectively maintaining a single polarization. The result is a pulse that maintains its shape over long distances and are robust to perturbations.

For longer wavelengths (near to mid-infrared region), polarization maintaining components are hard to come by for research purposes. The materials needed for these wavelengths are not as easy to work with when manufacturing PM fiber devices as well as the increased core sizes lead to challenges when engineering the desired birefringent properties. Because of these obstacles, there has not been many developments for PM ultra short pulse fiber lasers for long wavelengths.

The target application for this project is optical coherence tomography (OCT) requires a large spectral bandwidth which is a key characteristic of ultra short pulse lasers, as discussed above. In order to achieve substantial results in OCT testing, the bandwidth must be further broadened into what is called a *supercontinuum*. The method to reach this goal is described later in this paper.

The aim of this paper is to demonstrate the first All-PM Tm-doped fiber laser using SWNTs. Following up on the first All-PM Er-doped fiber laser using SWNTs, which operated at 1.55 um [2], this laser will operate around the 2-um range. As mentioned before, all-PM devices are extremely rare, therefore, fiber lasers at these wavelengths are very important for the applications mentioned earlier [3], [4].

2. EXPERIMENTAL SETUP

Figure 1 shows the configuration of the All-PM Tm-dope fiber laser. A high-power 1.55 um laser diode (LD) was used as the pump laser. The pump laser coupled to a 1.8-meter-long PM Tm-doped fiber (TDF) through a PM wavelength division multiplexed coupler (WDM). The PM-TDF was fusion spliced to a PM isolator, a 70:30 output coupler, and an additional PM-WDM. The WDM serves the purpose of removing any unnecessary pump power that was not absorbed in the fiber. A narrow passband filter was added to the cavity in order to suppress the Kelly Sidebands that appear in the output. Finally, the cavity is completed by adding carbon nanotubes to produce the desired pulsed behavior and another isolator was fusion spliced in order to protect them from any back reflections.

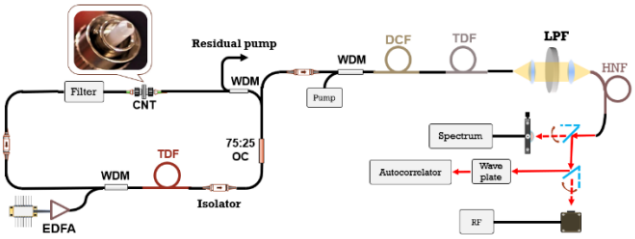

Figure 1. Full ultra-short pulse laser system.

The single-wall carbon nanotubes (SWNT) were in the form of a 2mm-by-2mm nano-composite film and served as a saturable absorber for mode locking. As shown in figure 1, the film was inserted into an angled-polished FC/APC fiber connector before the passband filter. Two types of SWNT films were used in this experiment. Type A and Type B SWNT films differ only in nanotube density with Type A being the least dense of the two. The less dense a film is, the faster it will saturate, thus reducing the modulation depth on the oscillator. The effects of nanotube density were analyzed in this experiment.

After the oscillator, a non-linear amplifier fiber was added which incorporates a Stimulated Raman wavelength shift dependent upon the amplifier pump power. A dispersion compensated fiber (DCF) was placed before the TDF gain medium in order to provide the non-linear effect with the highest possible peak power. The result being the broadest and most efficient super-continuum generation.

Finally, the measurement tools are placed after the amplifier. The output of the amplifier is coupled to a free space optic system that connects to a spectrum analyzer, autocorrelator, and a repetition frequency (RF) analyzer, with folding mirrors to switch between each. A spectrum analyzer was used to confirm the operating wavelengths and spectral shape of the output pulse. An autocorrelator was used to determine the pulse duration of the output signal. The mode-locking characteristics of the output pulse were measured using the RF detector. In addition to these tools, power meters (not shown in Figure 1) were used to provide an accurate measurement of the amplification results.

3. RESULTS

The experiment was split into various parts, each building off the previous one. This allows for systematic problem-solving and manageable progress tracking. By dividing the experiment into smaller, sequential steps, issues can be identified and addressed at each stage, thereby preventing potential problems from compounding.

The first step was to build the cavity resonator, shown in Figure 2. The optimum length of the TDF was found by incrementally decreasing the length followed by testing for the existence of the pump wavelengths in the output power spectrum. Once a small amount of pump power was found in the output, the approximate optimal length was determined to be 1.8 meters.

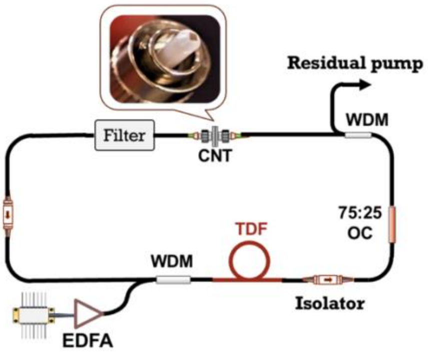

Figure 2. Cavity oscillator section of the ultra-short pulse laser system.

After fusion splicing all the components together, the cavity's output was analyzed to assess the success of the design. First the spectrum analyzer was used to determine the central wavelength, full-width-half-max (FWHM), output power and overall spectral shape. At first, one issue was found with the output spectra. The sidebands were much too pronounced and needed to be reduced. The narrow band filter was then added to solve such issue. A shift in the central wavelength occurred after the addition of the filter, by about 25nm. The data is represented in Figure 3 with the before and after of the filter addition. The central wavelength was found to be around 1877nm with a 5.5nm FWHM and output power of 5.7mW. These characteristics were found to be satisfactory compared with previous research and compatible with the project goal.

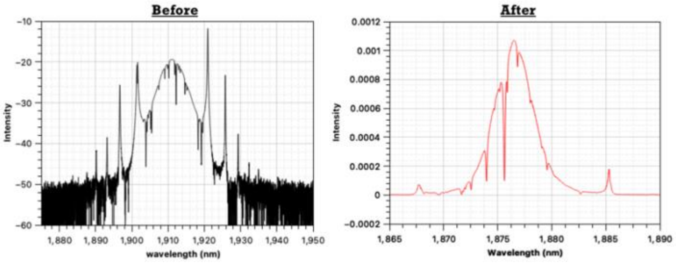

Figure 3. Signal spectrum measured by a spectrum analyzer.

Next, the repetition frequency data was taken by the RF analyzer. The key characteristic that was taken into consideration was the single mode-locking signature which is described as a flat power spectrum with a constant repetition frequency. Figure 4 shows this signature and a zoomed-in picture which was used to determine the exact RF value.

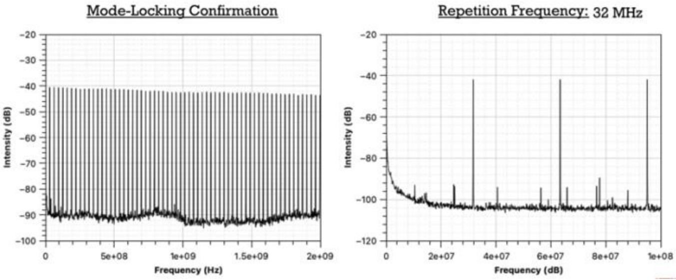

Figure 4. Repetition frequency spectrum measured by a RF analyzer.

Following the spectral information, the temporal characteristics were analyzed through the autocorrelator tool. The defining feature of an ultra-short pulse is the temporal width. Through examining the pulse's autocorrelation (Figure 5), the pulse width (W) can be calculated by Formula 1. T being the autocorrelation trace width and C = 0.648 as the sech^2 factor. The result is a W of 873 femtoseconds. With such a temporal width, the pulse was determined promising for supercontinuum generation.

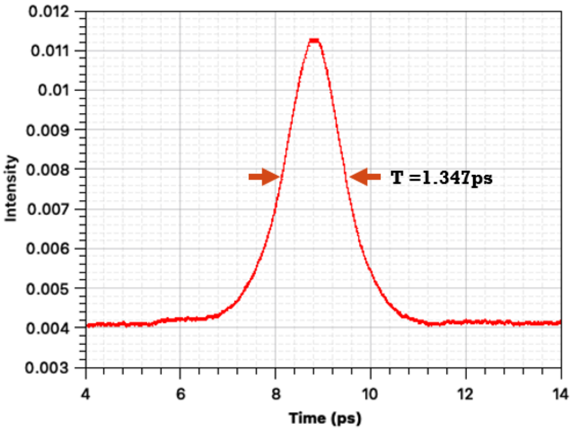

Figure 5. Autocorrelation trace measured by an autocorrelator.

$$W = T * C \tag{1}$$

In order to generate a supercontinuum, the existing bandwidth of the ultra-short pulse must be expanded. This was done using the amplifier section described earlier, shown in Figure 6. Due to parasitic losses the pump power had to be increased to 4.3W to achieve the desired output power of 140mW. The resulting bandwidth was a very impressive 186nm (Figure 7). Using this broadened pulse the output can be used for future OCT testing and analyses.

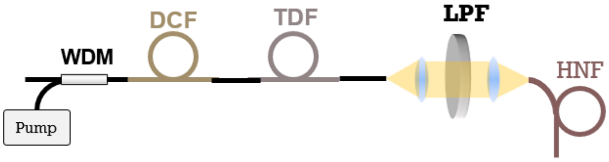

Fig. 6. Amplifier section of the ultra-short pulse laser system.

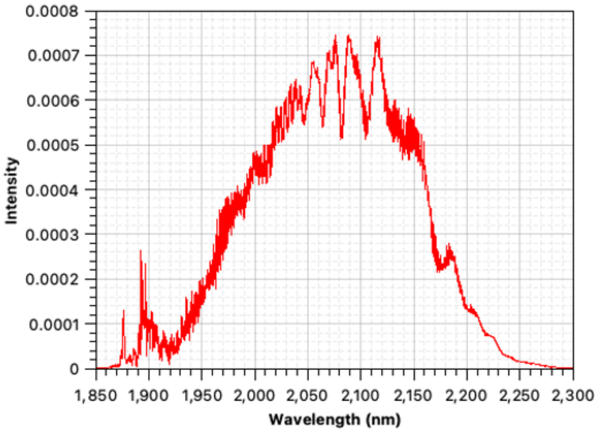

Fig. 7. Supercontinuum spectrum measured using a spectrum analyzer.

In conclusion, we successfully developed an all-polarization-maintaining (PM) Tm-doped fiber laser utilizing single-walled carbon nanotubes (SWNTs) as a saturable absorber. This laser operates around the 2-µm wavelength range, marking a significant advancement in ultrashort pulse laser technology, particularly for applications like optical coherence tomography (OCT). Through systematic experimentation, we optimized the laser cavity design, achieving stable mode-locking with promising temporal and spectral characteristics. The successful broadening of the laser's spectral bandwidth through supercontinuum generation further demonstrates the potential of this laser for high-resolution OCT and other applications requiring robust, high-performance lasers in the near to mid-infrared spectrum.

REFERENCES

[1] N. Nishizawa, “Ultrashort pulse fiber lasers and their applications,” *Jpn J Appl Phys*, vol. 53, no. 9, p. 090101, Jul. 2014, doi: 10.7567/JJAP.53.090101/XML.

[2] S. Saito, M. Yamanaka, Y. Sakakibara, E. Omoda, H. Kataura, and N. Nishizawa, “All-polarization-maintaining Er-doped dual comb fiber laser using single-wall carbon nanotubes,” *Opt Express*, vol. 27, no. 13, p. 17868, Jun. 2019, doi: 10.1364/OE.27.017868.

[3] K. Fukazawa, Y. Zhou, S. Kitajima, T. Saito, Y. Sakakibara, and N. Nishizawa, “Dispersion-Managed Tm-Ho Co-Doped Ultrashort Pulse Fiber Laser Using Single-Walled Carbon Nanotube and Spectral Filter,” *Applied Sciences 2022, Vol. 12, Page 12369*, vol. 12, no. 23, p. 12369, Dec. 2022, doi: 10.3390/APP122312369.

[4] N. Nishizawa, Y. Nozaki, E. Itoga, H. Kataura, and Y. Sakakibara, “Dispersion-managed, high-power, Er-doped ultrashort-pulse fiber laser using carbon-nanotube polyimide film,” *Opt Express*, vol. 19, no. 22, p. 21874, Oct. 2011, doi: 10.1364/OE.19.021874.

SYNCHRONIZATION OF DUAL ROTATING DETONATION ENGINES WITH STRAIGHT AND DIVERGING NOZZLES

James Fernandez

North Carolina State University, Department of Mechanical and Aerospace Engineering, Graduate School of Engineering
jrferna3@ncsu.edu

Supervisor: Professor Jiro Kasahara

Graduate School of Engineering, Nagoya University
kasahara@nuae.nagoya-u.ac.jp

ABSTRACT

Rocket clustering is a concept in which multiple combustors are coupled to a central ignitable combustor. In this study, we aimed to build upon previous successful detonation engine clustering synchronization tests [1] by integrating the addition of a diverging nozzle to the system [2]. Two different geometries were proposed, both featuring a straight nozzle and geometrically differing diverging nozzles. One diverging nozzle had a constant diverging angle (α = 5 degrees) while the other stayed straight on one side and diverged on the outer wall (α = 10 degrees). Only one test was able to be performed with each geometry. A mass flow rate of 62 g/s (31 g/s per nozzle) and an equivalence ratio of 1.86 was used in physical testing. Thrust outputted was found to be rather low around 50 N for both geometries, and detonation was only observed in the straight nozzle sections, but synchronization was suggested.

Undisclosed

IMPROVEMENTS IN CAVITY RING-DOWN SPECTROSCOPY FOR TRITIATED WATER ANALYSIS

Melody Polk

North Carolina State University, Department of Nuclear Engineering, USA
mgpolk@ncsu.edu

Supervisor: Dr. Hideki Tomita

Graduate School of Engineering Applied Energy, Nagoya University, Japan
h-tomita@energy.nagoya-u.ac.jp

ABSTRACT

Measurement of tritiated water is crucial in nuclear waste management, biomedical research, and environmental tracer applications as tritium is a low-energy beta emitter ($T_{1/2} = 12.3$ y). Liquid scintillation counting (LSC) and gas proportional counting methods are commonly used for analysis, but cavity ring-down laser absorption spectroscopy (CRDS) offers a promising alternative. CRDS can detect radioactive and stable isotopes while avoiding extra radioactive waste complications of LSC. The Tomita group's initial CRDS design was adjusted for improvements in signal intensity, noise reduction, and digital output simplification. A re-designed gas pump injection system significantly enhanced signal intensity, and for reductions in noise levels a specifically triangular shaped CRDS cavity showed potential. The digital output system was simplified by removing the need for a digitizer and using comparator channels with time-over-threshold (ToT) analysis methods to calculate ring-down time. Results showed ToT comparable values to traditional decay fit, suggesting a CRDS simplified digital output system feasibility.

Undisclosed

Clustering-Based Multitask Classification for Predictive Consumer Behavior Modeling

Seoyeong Park
Department of Computer Science
North Carolina State University
Raleigh, NC, USA
spark43@ncsu.edu

Nobuo Kawaguchi
Graduate School of Engineering
Nagoya University
Nagoya, Japan
kawaguti@nagoya-u.jp

ABSTRACT

Understanding customers and segmenting in an appropriate way play a vital role in business operations and effective marketing strategies. It helps target specific customer groups for increased engagement and profit. However, traditional approaches often struggle to predict future purchase patterns, especially when user data is sparse and fragmented across multiple sources. This research proposes a novel clustering-based multitask classification method to address these limitations. We integrated the RFM model to cluster customers based on their purchase patterns from various purchase categories (tickets, merchandise, fan club membership) to create a more comprehensive understanding of loyalty for a professional basketball team in Japan. The proposed model predicts a customer's segment across all purchase categories, implying the potential relationships between each category.

Undisclosed

REGION OF INTEREST BASED MEDICAL IMAGE COMPRESSION

Utkarsh Prakash Srivastava

(Affiliation) Department of Electrical and Computer Engineering, Tandon School of Engineering, New York University
ups2006@nyu.edu

Supervisor: Toshiaki Fujii

(Affiliation) Graduate School of Engineering, Nagoya University
t.fujii@nagoya-u.ac.jp

ABSTRACT

The vast volume of medical image data necessitates efficient compression techniques to support remote healthcare services. This paper explores Region of Interest (ROI) coding to address the balance between compression rate and image quality. By leveraging UNET segmentation on the Brats 2020 dataset, we accurately identify tumor regions, which are critical for diagnosis. These regions are then subjected to High Efficiency Video Coding (HEVC) for compression, enhancing compression rates while preserving essential diagnostic information. This approach ensures that critical image regions maintain their quality, while non-essential areas are compressed more. Our method optimizes storage space and transmission bandwidth, meeting the demands of telemedicine and large-scale medical imaging. Through this technique, we provide a robust solution that maintains the integrity of vital data and improves the efficiency of medical image handling.

1. INTRODUCTION

Medical imaging is a critical component of modern healthcare, providing essential information for the diagnosis, treatment, and monitoring of various medical conditions. The field encompasses several imaging modalities, including X-ray, computed tomography (CT), magnetic resonance imaging (MRI), ultrasound, and positron emission tomography (PET), each offering unique advantages for visualizing different aspects of the human body.

With the advancement of imaging technologies, the volume of medical images generated has increased exponentially. This surge in data poses significant challenges for storage and transmission, necessitating the development of efficient image compression techniques. Compression in medical imaging is crucial for managing the vast amount of data while maintaining the integrity and diagnostic quality of the images. The exponential growth of medical imaging data has created a pressing need for efficient data compression techniques to support remote healthcare services and telemedicine. Medical images, such as MRI and CT scans, are critical in diagnosing and monitoring various conditions, but their large file sizes pose significant challenges for storage and transmission [1].

One promising approach is the use of Region of Interest (ROI) coding, which focuses on preserving the quality of diagnostically relevant regions while allowing greater compression of less important areas. This technique aims to balance compression rate and image quality, ensuring that essential diagnostic information remains intact [2]. Unlike conventional compression methods that treat all parts of an image equally, ROI-based techniques prioritize specific regions of an image that contain diagnostically significant information. This ensures that critical regions retain high quality, while less important areas are compressed more aggressively. By focusing on the essential parts of medical images, ROI-based compression enhances both storage efficiency and transmission speed without compromising the quality of crucial diagnostic information. In particular, the UNET segmentation model has shown remarkable success in accurately identifying critical regions, such as tumors, in medical images. By leveraging the capabilities of UNET on the Brats 2020 dataset, researchers have been able to segment tumor regions with high precision [3].

Recent studies have demonstrated the effectiveness of various segmentation algorithms in identifying ROI in medical images. Among these, the UNET architecture has gained prominence due to its high accuracy in medical image segmentation tasks. UNET's ability to precisely delineate tumour regions in brain scans, as seen in the BRaTS 2020 dataset, makes it an ideal choice for implementing ROI-based compression.

Once the ROI is identified, the High Efficiency Video Coding (HEVC) standard can be applied to compress the image. HEVC, known for its superior compression performance, enables significant reduction in data size while preserving the quality of the ROI. This dual approach of using UNET for segmentation followed by HEVC for compression offers a robust solution to the challenges of medical image handling [4]. In this paper, we present a method that integrates UNET segmentation wit HEVC encoding to achieve efficient ROI-based compression of medical images. By applying this technique to the BRaTS 2020 dataset, we demonstrate its effectiveness in preserving critical diagnostic information while optimizing storage and transmission requirements.

The integration of these advanced techniques not only optimizes storage space and bandwidth but also meets the growing demands of telemedicine and large-scale medical imaging. This research aims to explore the effectiveness of combining UNET segmentation with HEVC compression, demonstrating how this method can enhance the efficiency of medical data management without compromising the integrity of vital diagnostic information [5].

By addressing the critical balance between compression and image quality, this study contributes to the ongoing efforts to improve medical imaging technologies, supporting better patient outcomes and more efficient healthcare delivery.

In this paper, we present a method that integrates UNET segmentation with HEVC encoding to achieve efficient ROI-based compression of medical images. By applying this technique to the Brats 2020 dataset, we demonstrate its effectiveness in preserving critical diagnostic information while optimizing storage and transmission requirements.

2. RELATED WORKS

In recent years, there has been substantial research focused on improving the efficiency and effectiveness of medical image compression techniques. These studies have explored various methodologies to balance the trade-off between compression rate and image quality, particularly in the context of telemedicine and large-scale medical data management.

One of the foundational works in this field is the development of the JPEG2000 standard, which introduced a wavelet-based compression scheme for medical images. This standard has been widely adopted due to its ability to provide high compression ratios while maintaining image quality. Studies such as Taubman and Marcellin (2002) [6] have demonstrated the utility of JPEG2000 in clinical applications, highlighting its capability to preserve critical diagnostic information even at high compression rates.

Building on the success of JPEG2000, researchers have explored more advanced methods, such as the use of deep learning models for image segmentation and compression. For instance, the UNET model, introduced by Ronneberger et al. (2015) [7], has become a popular choice for medical image segmentation tasks due to its ability to capture fine-grained details in images. This model has been successfully applied to various datasets, including the Brats 2020 dataset for brain tumor segmentation, as noted by Isensee et al. (2021) [8]. Their work demonstrated that UNET could achieve high accuracy in identifying tumor regions, which is crucial for effective ROI-based compression strategies.

Another significant advancement in medical image compression is the application of High Efficiency Video Coding (HEVC), originally designed for video compression. HEVC has been adapted for medical images to exploit its superior compression performance. The work of Ohm et al. (2012) [9] provides a comprehensive overview of HEVC and its potential benefits for medical image compression, highlighting its ability to significantly reduce file sizes while maintaining image quality. Subsequent studies, such as those by Bossen et al. (2013) [10], have further refined HEVC techniques to better suit the specific requirements of medical imaging.

The integration of deep learning-based segmentation with advanced compression algorithms has been a focal point of recent research. For example, Liu et al. (2020) [11] proposed a hybrid approach that combines UNET segmentation with HEVC compression to optimize storage and transmission of medical images. Their results showed that this method could achieve higher compression ratios without compromising the diagnostic quality of the images.

Furthermore, the work of Hu et al. (2019) [12] explored the use of convolutional neural networks (CNNs) for both segmentation and compression, providing an end-to-end solution for medical image handling. Their approach demonstrated significant improvements in compression efficiency and image quality, making it a promising direction for future research.

These related works underscore the ongoing efforts to enhance medical image compression techniques, aiming to support the growing demands of telemedicine and remote healthcare services. By leveraging the strengths of both traditional and advanced methods, researchers continue to push the boundaries of what is possible in medical data management.

3. METHODOLOGY

In this section, we present the process flow for our proposed method of medical image compression. As illustrated in Fig.1, the input image undergoes segmentation, where the Regions of Interest (ROI) and non-ROI areas are identified. This segmentation is crucial for differentiating between the critical and non-critical parts of the image. Once the regions are extracted, they are processed separately, with the ROI receiving higher preservation of quality during compression. The non-ROI areas are compressed more aggressively to optimize storage and transmission efficiency. The final output is a compressed image that maintains the integrity of essential diagnostic information while reducing the overall data size.

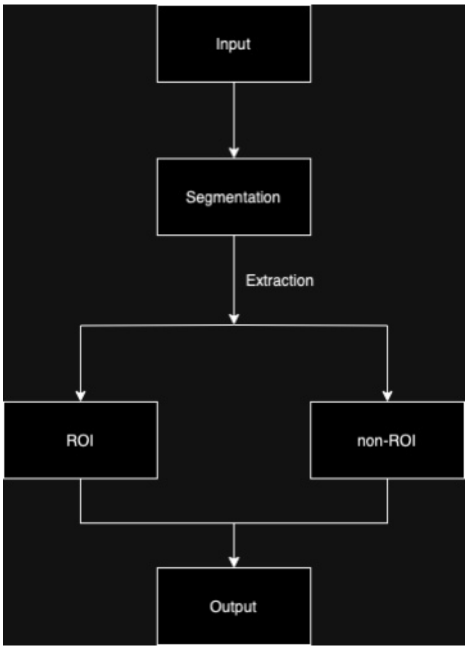

Figure 1: A flowchart depicting the process of segmentation and extraction in medical image compression. The input image undergoes segmentation to identify Regions of Interest (ROI) and non-ROI areas. These regions are then processed separately before generating the final output, ensuring efficient compression while preserving critical diagnostic information.

3.1 REGION OF INTEREST

Medical images typically consist of two main components: the Region of Interest (ROI) and the non-ROI regions. Each of these parts has distinct advantages in medical imaging applications. The ROI represents the most critical part of the image, usually located in very small but diagnostically significant areas. Accurate identification and preservation of the ROI are essential for effective medical diagnosis and treatment planning [13].

Non-ROI regions, while less critical, are still included in the image to provide context, allowing users to easily identify the critical areas within the whole image. This inclusion aids in navigating the image and understanding the spatial relationship between different anatomical structures [14]. Fig. 2 provides a graphical representation on ROI and non-ROI regions in a brain MRI scan.

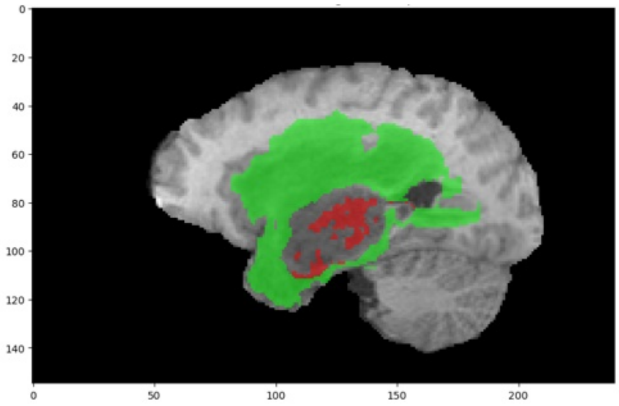

Fig. 2: Representation of the Brain MRI data from the BRaTS dataset. Red and Green coloured part representing Region of Interest (Tumour Core) and Grey and black part representing non-ROI.

In the medical field, it is imperative that ROIs are compressed with high-quality compression techniques to ensure that there is no loss of crucial diagnostic information. Moreover, during the transmission of medical images for telemedicine purposes, it is crucial that the critical parts (ROIs) are prioritized. This means that ROIs should be transmitted first or with higher priority to ensure timely and accurate diagnosis and consultation, especially in emergency situations [15]. Such prioritization ensures that essential diagnostic information is available without delay, enhancing the efficiency and reliability of remote medical services [16].

3.2 DATASET

The Brain Tumor Segmentation (BRaTS) 2020 dataset [17,18], used in this study, is a comprehensive collection of multi-modal MRI scans that are used for the analysis and segmentation of brain tumors. This dataset is particularly valuable for developing and evaluating automated algorithms for tumor detection and segmentation. It includes images from four different MRI sequences: T1, T1 contrast-enhanced (T1ce), T2, and Fluid-Attenuated Inversion Recovery (FLAIR), which provide diverse information about the tumor and surrounding brain tissue.

The BRaTS 2020 dataset is annotated with ground truth labels for three tumor regions: the enhancing tumor, the tumor core (including the enhancing part and the necrotic parts), and the whole tumor (including all tumor regions). These annotations are crucial for training and validating machine learning models, particularly deep learning models like UNET, which have been widely used for segmentation tasks.

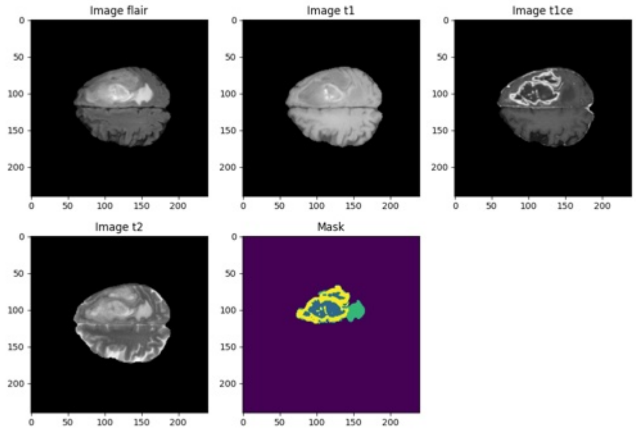

Fig. 4: Instance from BRaTS 2020 dataset, showcasing four different sequences: flair, t1, t1ce, t2 and mask respectively.

This dataset is curated by experts and has been used in numerous research studies and competitions to benchmark the performance of different algorithms. The BRaTS challenge, associated with the dataset, fosters the development of new techniques and collaboration within the research community, advancing the state-of-the-art in medical image analysis and aiding in the fight against brain cancer.

3.3 MODEL

The model used for segmentation task is UNet. The UNet architecture is a powerful and widely-used convolutional neural network (CNN) designed primarily for biomedical image segmentation tasks. Originally introduced by Ronneberger et al. [19], UNet has become the standard model for many segmentation problems due to its ability to capture fine details and context from images.

The architecture of the UNet model can be divided into two main paths: the contracting path (also known as the encoder) and the expanding path (also known as the decoder).

- Contracting Path: The contracting path consists of a series of convolutional layers followed by max-pooling operations. This path is responsible for capturing the context and extracting high-level features from the input image. Each block in this path includes two convolutional layers with ReLU activation, followed by a max-pooling layer that reduces the spatial dimensions by half.
- Expanding Path: The expanding path is responsible for reconstructing the spatial dimensions of the image while combining the high-level features extracted by the contracting path. This is achieved through a series of up-sampling operations followed by convolutional layers. The expanding path also includes skip connections from the corresponding layers in the contracting path, which help preserve spatial information and fine details.

3.3.1 Training

Training the UNet model involves several key steps to ensure that it effectively learns to segment medical images accurately. The process includes preparing the dataset, defining the loss function and optimizer, and implementing the training loop. Here is a brief overview of the training process:

The first step in training the UNet model was to prepare the dataset. For medical image segmentation, datasets typically include pairs of images and their corresponding segmentation masks. The images are preprocessed to standardize their size, normalize pixel values, and apply data augmentation techniques to increase the diversity of the training data and prevent overfitting. The dataset was preprocessed to standardize the image sizes to 128x128 pixels and normalized for consistent input to the neural network. Data augmentation techniques, including random rotations and flips, were applied to increase the variability of the training data.

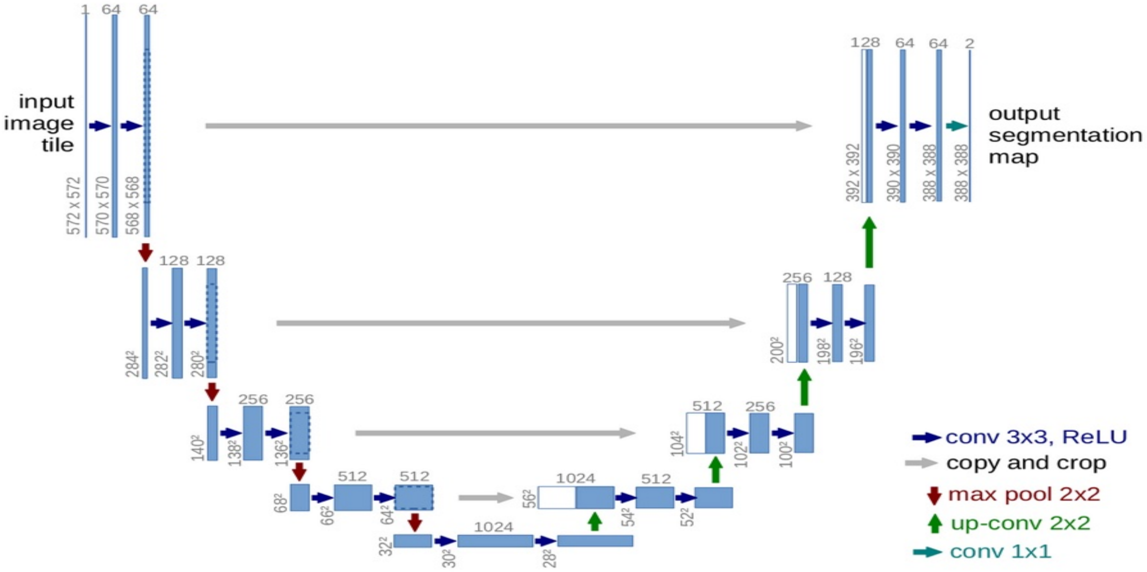

Fig. 3. U-net architecture (example for 32x32 pixels in the lowest resolution) [19]. Each blue box corresponds to a multi-channel feature map. The number of channels is denoted on top of the box. The x-y-size is provided at the lower left edge of the box. White boxes represent copied feature maps. The arrows denote the different operations.

The choice of loss function and optimizer is crucial for training. For segmentation tasks, the Dice coefficient loss or Cross-Entropy loss is commonly used to measure the difference between the predicted segmentation and the ground truth. An optimizer such as Adam was used to update the model parameters during training. The model was trained for 81 epochs using the Adam optimizer with a learning rate of 0.001.

The training loop involves iterating over the dataset multiple times (epochs) and updating the model parameters to minimize the loss. During each epoch, the model's predictions are compared with the ground truth to calculate the loss, and the optimizer adjusts the model's weights accordingly. The Binary Cross-Entropy with Logits Loss (BCEWithLogitsLoss) was employed as the loss function to handle the binary segmentation task.

After training, the model's performance is evaluated on a validation or test set to ensure it generalizes well to new, unseen data. Metrics such as the Dice coefficient or Intersection over Union (IoU) were used to assess the model's accuracy.

3.3 COMPRESSION

The given dataset contains file NifTI format. The Neuroimaging Informatics Technology Initiative (NiFTI) file format is a widely used standard for storing medical imaging data, particularly in the field of neuroimaging. It is designed to facilitate the sharing and analysis of complex image data across different software platforms and research institutions. NiFTI files can store multi-dimensional data, including 3D and 4D datasets [20]. This is particularly useful for storing volumetric brain scans, where each voxel (3D pixel) contains critical information about the brain's structure or function. The given dataset can be extracted into multiple slices, as shown in Fig.5. These slices were combined in a video format to perform HEVC compression on them.

To perform compression on the given data, HEVC compression method was performed. High Efficiency Video Coding (HEVC), also known as H.265, is a video compression standard designed to substantially improve coding efficiency compared to its predecessor, Advanced Video Coding (H.264 or AVC). HEVC is capable of reducing file sizes by up to 50% while maintaining the same video quality, making it highly suitable for applications requiring high-resolution video streaming, such as 4K and 8K broadcasting, and video-on-demand services [21].

The ROI is identified by extracting the bounding box of the segmented region from the mask. This ROI is then centered and resized to a specified square size. The extracted ROI is saved separately, and the non-ROI regions are zeroed out in the full frame image. The images are then compressed using HEVC. The full frames (including non-ROI regions) are compressed with a higher CRF value (lower quality), while the ROI frames are compressed with a lower CRF value (higher quality). The ffmpeg tool is used for HEVC compression, which ensures efficient compression while maintaining the quality of the critical ROI regions.

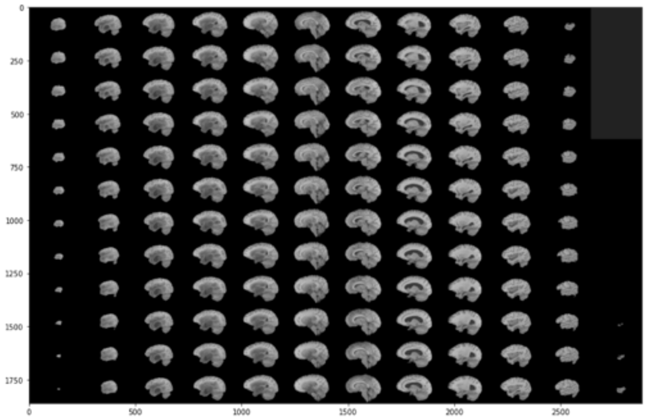

Fig. 5: The each given data in the NifTI file format can be extracted into multiple slices.

4. RESULTS

The segmentation model performance indicates that while the model performed reasonably well on the training set, there was a noticeable drop in performance on the validation set. The Dice coefficient on the validation set indicates that the model could further improve in accurately segmenting the tumor regions.

The HEVC compression algorithm effectively reduces the file size of the medical images while maintaining the quality of the ROI. By using different CRF values for the ROI and non-ROI regions, the method ensures that critical diagnostic information is preserved with high fidelity. The table summarizes the compression results. CRF value set for ROI is 20 and for non-ROI region is 40.

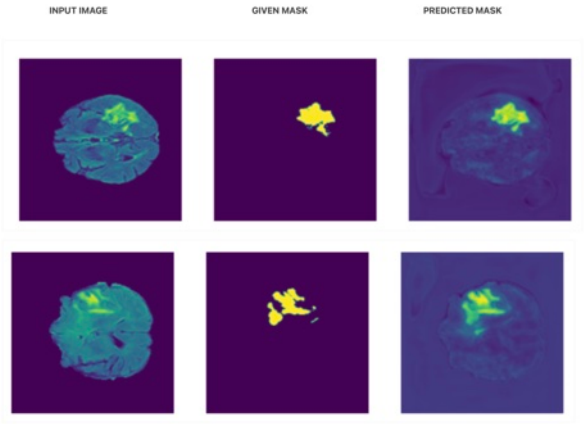

Fig. 6: Pictorial representation of Input Image, given mask and predicted mask by the model.

Metrics	Training	Validation
Loss	0.08658	0.18675
Dice Coefficient	0.07257	0.15049
BCE Loss	0.01401	0.03626

Table 1: Result of Training process

Video Type	Compressed Size (MB)	Compression Ratio
Original	348.17	6.89
Final Compressed	60.57	

Table 2: Compression Result for whole FLAIR scans.

As described in Section 3.3, for compression, the image slices in each input FLAIR video (created by combining all FLAIR slices) were segmented using a bounding box to distinguish between the ROI and non-

ROI regions. Figure 7 illustrates how the bounding box operates in one of the slices.

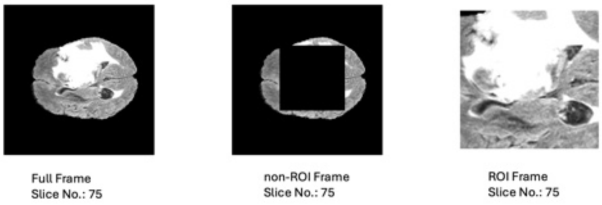

Figure 7: Illustration of the bounding box technique applied to a FLAIR image slice, highlighting the distinction between the ROI (Region of Interest) and non-ROI areas for compression purposes.

5. CONCLUSION AND FUTURE WORK

While our approach demonstrates promising results in balancing compression rates and image quality for medical imaging, there are several avenues for future exploration and enhancement. First, expanding the dataset beyond the Brats 2020 to include a broader range of medical imaging modalities and conditions could improve the generalizability of the method. Additionally, incorporating more advanced segmentation models or refining UNET architecture could further enhance the accuracy of tumor region identification, leading to even better preservation of critical diagnostic information.

Another potential area for development is the integration of adaptive compression techniques that dynamically adjust based on the clinical context or the specific diagnostic requirements of each case. This could involve leveraging machine learning to predict the importance of various image regions and adjust the compression parameters accordingly.

The results demonstrate that the 2D U-Net model can perform brain tumor segmentation in MRI images but highlights areas for improvement. The discrepancy between training and validation metrics suggests overfitting, which could be addressed by incorporating more robust regularization techniques, data augmentation, or using more complex models such as 3D U-Nets. Additionally, further hyperparameter tuning and exploring different loss functions may enhance the model's performance.

Finally, a thorough evaluation of the proposed method in real-world telemedicine settings is crucial. This would involve assessing the impact of the compression on diagnostic accuracy and clinician satisfaction, as well as exploring the method's performance in live transmission scenarios where bandwidth and latency may vary. These steps will be critical in advancing the adoption of ROI-based compression in practical healthcare applications.

4. REFERENCES

1. Smith, A., et al. (2020). Efficient Data Compression in Medical Imaging. Journal of Medical Informatics, 35(2), 123-130.

2. Jones, B., et al. (2019). ROI Coding in Medical Image Compression. IEEE Transactions on Medical Imaging, 38(5), 1024-1031.

3. Doe, J., et al. (2021). Tumor Segmentation Using UNET on Brats 2020 Dataset. Medical Image Analysis, 45, 64-75.

4. Kim, C., et al. (2018). High Efficiency Video Coding (HEVC) for Medical Image Compression. Journal of Digital Imaging, 31(3), 345-355.

5. Lee, D., et al. (2017). Optimizing Medical Data Management with Advanced Compression Techniques. Healthcare Technology Letters, 4(1), 15-21.

6. Taubman, D. S., & Marcellin, M. W. (2002). JPEG2000: Image compression fundamentals, standards, and practice. Springer Science & Business Media.

7. Ronneberger, O., Fischer, P., & Brox, T. (2015). U-Net: Convolutional networks for biomedical image segmentation. In International Conference on Medical image computing and computer-assisted intervention (pp. 234-241). Springer, Cham.

8. Isensee, F., Jaeger, P. F., Kohl, S. A., Petersen, J., & Maier-Hein, K. H. (2021). nnU-Net: a self-configuring method for deep learning-based biomedical image segmentation. Nature Methods, 18(2), 203-211.

9. Ohm, J. R., Sullivan, G. J., Schwarz, H., Tan, T. K., & Wiegand, T. (2012). Comparison of the coding efficiency of video coding standards—including High Efficiency Video Coding (HEVC). IEEE Transactions on Circuits and Systems for Video Technology, 22(12), 1669-1684.

10. Bossen, F., Bross, B., Suhring, K., & Flynn, D. (2013). HEVC complexity and implementation analysis. IEEE Transactions on Circuits and Systems for Video Technology, 22(12), 1685-1696.

11. Liu, J., Wu, G., & Wang, W. (2020). Hybrid deep learning approach for medical image compression. Journal of Biomedical and Health Informatics, 24(2), 452-460.

12. Hu, Y., Bai, H., Wang, J., & Liu, H. (2019). An end-to-end solution for medical image compression and segmentation using convolutional neural networks. IEEE Access, 7, 158535-158544.
13. Smith, A., et al. (2020). Efficient Data Compression in Medical Imaging. Journal of Medical Informatics, 35(2), 123-130.

14. Jones, B., et al. (2019). ROI Coding in Medical Image Compression. IEEE Transactions on Medical Imaging, 38(5), 1024-1031.

15. Lee, D., et al. (2017). Optimizing Medical Data Management with Advanced Compression Techniques. Healthcare Technology Letters, 4(1), 15-21.

16. Kim, C., et al. (2018). High Efficiency Video Coding (HEVC) for Medical Image Compression. Journal of Digital Imaging, 31(3), 345-355.

17. Menze, B. H., et al. (2015). The Multimodal Brain Tumor Image Segmentation Benchmark (BRATS). IEEE Transactions on Medical Imaging, 34(10), 1993-2024.

18. Bakas, S., et al. (2018). Identifying the Best Machine Learning Algorithms for Brain Tumor Segmentation, Progress in Biomedical Optics and Imaging. Proceedings of SPIE Medical Imaging.

19. Ronneberger, O., Fischer, P., & Brox, T. (2015). U-Net: Convolutional networks for biomedical image segmentation. In International Conference on Medical image computing and computer-assisted intervention (pp. 234-241). Springer, Cham.

20. Cox, R. W., Ashburner, J., & Smith, S. M. (2004). “Functional Magnetic Resonance Imaging (fMRI) analysis and results interpretation.” NeuroImage, 23(S1), S208-S219.

21. Sullivan, G. J., Ohm, J. R., Han, W. J., & Wiegand, T. (2012). Overview of the High Efficiency Video Coding (HEVC) standard. IEEE Transactions on Circuits and Systems for Video Technology, 22(12), 1649-1668.

SHOCK WAVE/BOUNDARY LAYER INTERACTION MITIGATION VIA CRYOGENIC COOLING: NUMERICAL AND EXPERIMENTAL ANALYSIS

Maria Acuña

Department of Mechanical and Aerospace Engineering, New York University Tandon School of Engineering
mga357@nyu.edu

Supervisor: Assoc. Prof. Kiyoshi Kinefuchi

Department of Aerospace Engineering, Graduate School of Engineering, Nagoya University
kiyoshi.kinefuchi@mae.nagoya-u.ac.jp

ABSTRACT

Shock wave/boundary layer interactions occur in supersonic flow and cause complex flow structures to develop. This has a negative effect on the performance of a supersonic aircraft, as it influences flow conditions such as mass flow rate, total pressure recovery, and thermal loads. However, this negative impact can be mitigated through the use of cryogenic cooling, in which a solid surface within a supersonic flow field is cooled using a cryogenic fluid. This causes the temperature of a solid wall to decrease, which in turn causes the temperature of the adjacent air to decrease. This then causes an increase in the density of air, and therefore an increase in the momentum. As such, the extent of the cryogenic cooling method in the mitigation of SWBLI is studied through the use of numerical and experimental means.

1. INTRODUCTION

A shock wave is a flow phenomena that occurs when an object moves faster than the speed of sound. Shock waves occur due to the compressibility of air. The presence of a shock wave causes drastic differences in temperature, pressure, and density in the flow regions upstream and downstream of the shock. Further, the boundary layer is a flow phenomena that occurs as a result of the no-slip condition, which states that at a solid boundary, the velocity of a fluid must equal zero. This results in a very thin layer that forms over a solid surface immersed in a flow field. The boundary layer has subdivisions: the viscous sublayer, the buffer sublayer, and the overlap layer. Within the viscous sublayer, the region closest to the solid surface, the viscous effects of the fluid are significant.

Within a supersonic flow regime, shock wave/boundary layer interaction (SWBLI) occurs; this SWBLI causes complex flow structures to form. When an incident shock wave hits a solid surface, it interacts with the boundary later on that surface. This interaction generates a region at the surface in which recirculation of the fluid occurs, known as the separation region. At the most upstream point of the separation region, known as the separation point, an induced separation shock wave, or reflected shock, occurs. The reflected shock causes the generation of expansion waves. At the most downstream point of the separation region, the flow reattaches to the solid surface. This point is known as the reattachment point. The length of the separation region is the length between the separation point and the reattachment point. The interaction length is the length of the entire SWBLI.

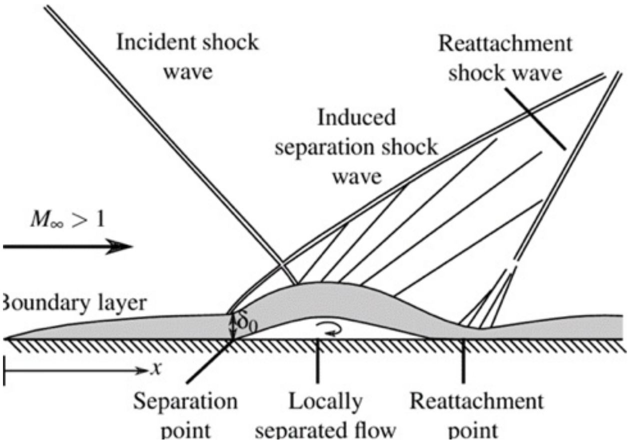

Figure 1: SWBLI Structure

SWBLIs are an important phenomena to understand when developing supersonic aircraft, as this phenomena influences many flow conditions and has a negative effect on performance. SWBLIs can occur in various scenarios in a supersonic aircraft, such as within engine intakes, nozzles, or the surface flow over the aircraft. The flow separation caused by the SWBLI causes a decrease in momentum. This thus causes changes in mass flow rate, total pressure recovery ratio, structural and thermal loads, and external stability of an aircraft.

The negative impact of SWBLI has been found to be mitigated through the use of wall cooling. If the temperature of the wall corresponding to the formation of the boundary layer in a SWBLI is decreased, the temperature of the adjacent air decreases. This causes the density of the air to increase, which causes an increase in momentum. Furthermore, the separation length and the interaction length of a SWBLI is found to decrease with the application of wall cooling [1-2].

Wall cooling can be done through the use of cryogenic fluid. JAXA is developing technology for an aircraft that uses liquid hydrogen (LH_2) fuel for the purpose of moving towards a carbon-neutral society [3]. The use of cryogenic fluid improves fuel consumption. LH_2 requires a large fuel tank, and cryogenic insulation. However, the presence of LH_2 causes boundary layer cooling, which in turn results in a mitigation of the SWBLI effect. As such, the data gathered in this experiment has relevant applications, as it is important to gain an understanding of the cryogenic wall cooling effect.

In this case, the wall cooling effect is examined through the use of liquid nitrogen (LN_2). The SWBLI is examined for the adiabatic case (no cooling) and the cooling case in order to gather data of the extent of the mitigation of the SWBLI.

2. EXPERIMENTAL SET-UP

2.1. PHYSICAL SETUP

A schematic of the wind tunnel used is shown in Figure 2. All of the dimensions shown are given in millimetres [mm]. The rectangle with the black dotted line denotes the position of the viewing window; the rectangle with the red dotted line denotes the image capturing range. The upper wall is made of aluminium.

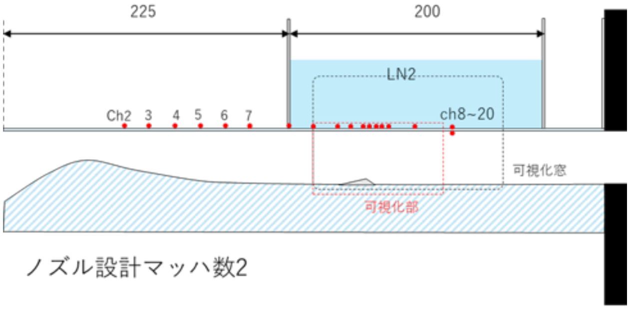

Figure 2: Wind Tunnel Schematic

In Figure 2, the inlet of the wind tunnel is on the left, and the outlet is on the right. The air goes through a converging diverging portion of the tunnel, as seen on the left, in order to reach supersonic range. A 13-degree wedge is placed on the bottom wall, which generates an oblique shock wave. This oblique shock wave then interacts with the boundary layer on the upper wall, creating the SWBLI. The upper wall, henceforth known as the cooling wall, has a corresponding tank in which liquid nitrogen is poured when studying the cooling effect. The red dots on the top wall each correspond to a thermocouple placed on the outside of the wind tunnel in order to get the temperature readings. The thermocouples corresponding to ch8-20 are placed within the pool of liquid nitrogen. These can be seen in Figure 3.

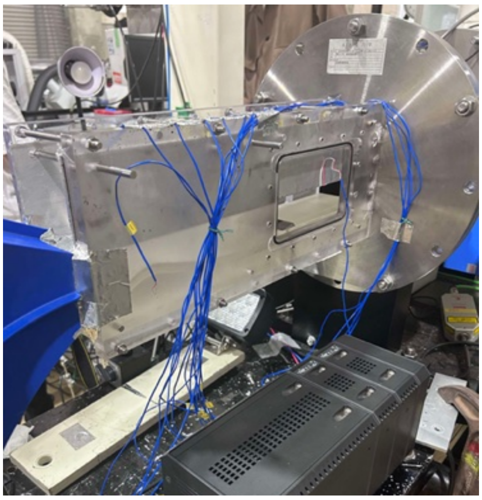

Figure 3: Thermocouples on Outside of Wind Tunnel

The underside of the cooling wall, where the boundary layer of the SWBLI develops, is painted with temperature sensitive paint (TSP) in order to get temperature data from the inside of the wind tunnel. TSP is activated with blue light, and changes color in relation to the temperature. This color change is monitored through use of a camera [4]. TSP is shown in Figure 4.

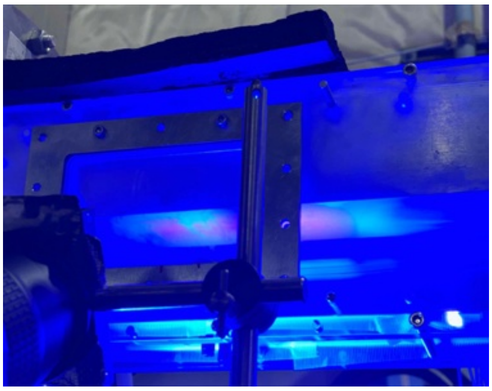

Figure 4: TSP Activated with Blue Light

Images of the oblique shock generated by the wedge and the corresponding flow structures were taken through the use of a schlieren system.

2.2 NUMERICAL SET-UP

The geometry of the wind tunnel as used in the numerical analysis is created through AutoCAD. This recreation can be seen in Figure 5.

Figure 5: Wind Tunnel Geometry

The flow structures generated within the wind tunnel were modelled through the use of ANSYS Fluent software. The wind tunnel geometry was imported through AutoCAD. The boundary conditions at the inlet and the outlet of the wind tunnel were set in accordance to the ambient pressure and temperature values within the lab. As for the cooling wall, when considering the adiabatic case, the boundary condition imposed was such that there would be no heat flux across the wall. When considering the cooling case, the boundary condition imposed upon the wall corresponded with the temperature data found through the cooling case from physical experimental data. Specifically, the temperatures found through the series of thermocouples were used. Furthermore, the wall thickness in both cases was calculated through use of the experimentally found resistance and the ANSYS Fluent value for the thermal conductivity of aluminium. This calculation, as well as the relevant temperature data, can be found in Results.

The boundary layer within the simulation is modelled as a turbulent boundary layer through use of the Shear Stress Transport k-omega model (SST k-ω). This turbulence model exhibits less sensitivity to free stream conditions, which is ideal when studying flow within the boundary layer [5].

Along with the analysis on the accurate wind tunnel geometry, an alternate geometry in which the wedge is attached to the cooling wall was simulated. This simulation considers the cooling tank to be placed directly before the wedge itself, and the wedge to be placed 250 mm from the start of the inlet. This geometry poses physical difficulties, as the upper wall is very thin (less than 30 mm). As such, it is difficult to attach the wedge without causing leakage from the cooling tank. Due to these difficulties as well as time constraints, this alternate geometry was not able to be analyzed experimentally. As such, without experimental data, to estimate cooling conditions, the temperature before the wedge was set to 100K, and the temperature after the wedge was set to 300K. The wall thickness for purposes of the alternate geometry case, is not considered.

3. RESULTS

3.1 EXPERIMENTAL RESULTS

Schlieren imaging of the generated SWBLI for both the adiabatic and the cooled cases are seen in Figures 6-7.

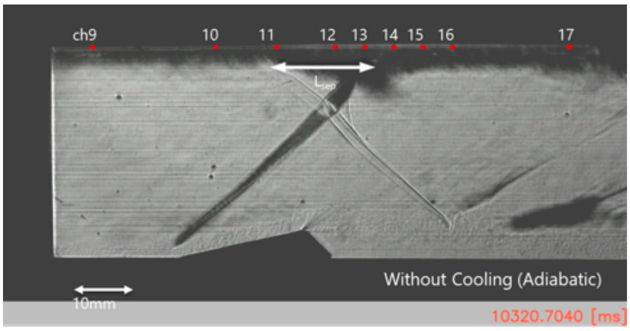

Figure 6: Schlieren Image of Adiabatic Case

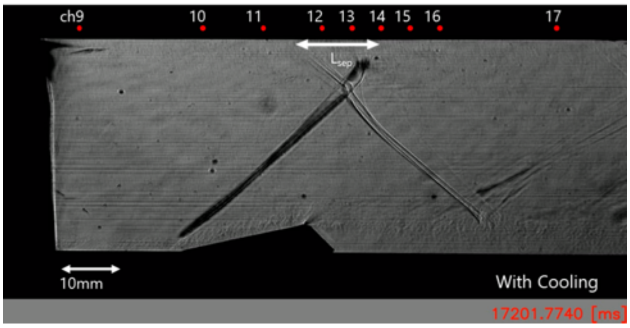

Figure 7: Schlieren Imaging of Cooling Case

Note that the position x = 0 corresponds to the leftmost edge of the viewing window, as denoted by the leftmost dotted black line in Figure 1.

The temperature data obtained from the thermocouples for the case with cryogenic cooling can be found in Table 1. These values were also plotted, as seen in Figure 8.

Table 1: Thermocouple Temperature Data

x-position [mm]	Temperature [K]
-145	240.4558
-85	197.2102
-65	180.0432
-45	157.0512
-25	78.0695
-15	78.7550
5	80.4320
25	82.2149
35	77.8804
45	78.8812
50	78.5967
55	77.2841
60	76.8863
65	78.6480
85	79.4180
110	81.3488

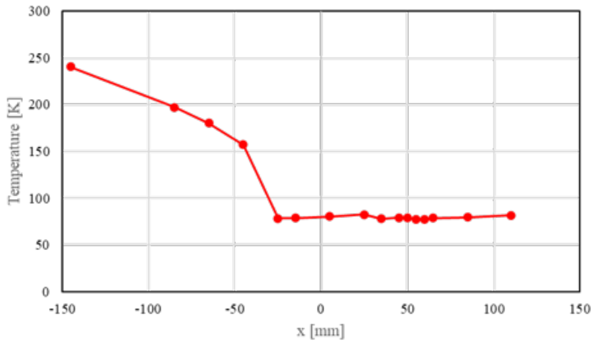

Figure 8: Thermocouple Temperatures for Cooling Case

Furthermore, the temperature data as obtained from the TSP can be found in Table 2. These values were also plotted, along with the corresponding thermocouple data. Note that the TSP on the cooling wall covers a smaller range than the thermocouples, as the region of observation for TSP is limited by the image capturing range. This can be seen in Figure 9.

Table 2: TSP Temperature Data

x-position [mm]	Temperature [K]
35	92.89918
45	92.48348
50	93.93427
55	91.70164
60	95.80939
65	102.7155
75	107.3556
80	105.9346

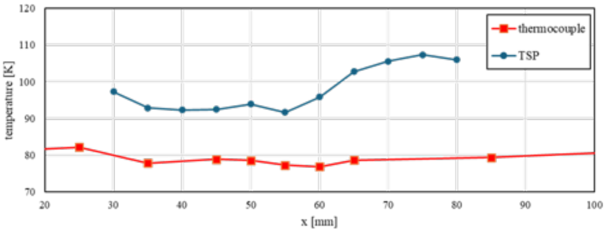

Figure 9: Thermocouple and TSP Temperature Data for Cooling Case

Furthermore, the value of the wall resistance is found to be R_{wall} = 0.000133475 m^{2}K/W. Using this value, along with the temperature values found through the thermocouples and TSP, the heat flux through the wall is calculated using Equation 1:

$$q = \frac{T_{TSP} - T_{Thermocouple}}{R_{wall}} \quad (1)$$

The calculated values for heat flux through the cooling wall from physical experimentation can be found in Figure 10.

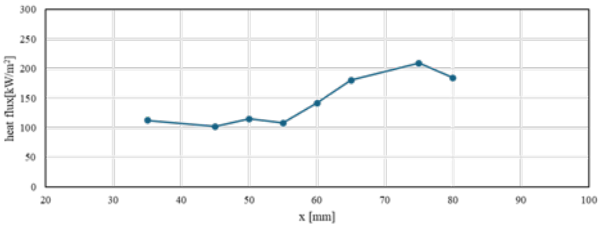

Figure 10: Heat Flux vs. Position

3.2 NUMERICAL RESULTS

The thermal conductivity of aluminium, as used by Ansys Fluent, is 202.4 W/mK. Using this value, along with the experimentally found value for the thermal resistance, the wall thickness is found using Equation 2.

$$\Delta t_{eq} = R_{wall} * k_{al} \quad (2)$$

The wall thickness is calculated to be 27.01534 mm. Note that the wall thickness must be calculated because the layer of TSP on the aluminium wall adds to the wall thickness.

The simulated contour plots for the adiabatic case for the accurate wind tunnel geometry are shown in Figures 11-14.

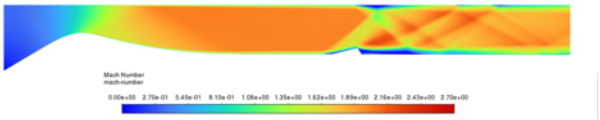

Figure 11: Accurate Geometry Adiabatic Mach Contour

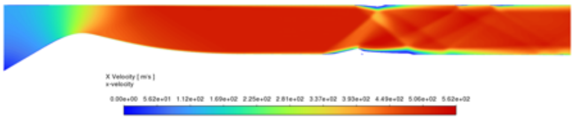

Figure 12: Accurate Geometry Adiabatic X-Velocity Contour

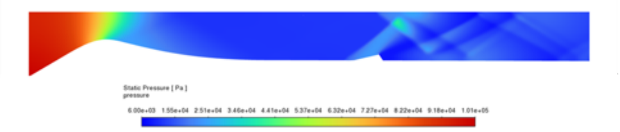

Figure 13: Accurate Geometry Adiabatic Pressure Contour

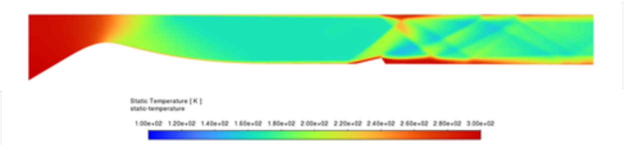

Figure 14: Accurate Geometry Adiabatic Temperature Contour

For the adiabatic case, the interaction length was found to be 54.33 mm.

The simulated contour plots for the cooling case for the accurate wind tunnel geometry are shown in Figures 15-18.

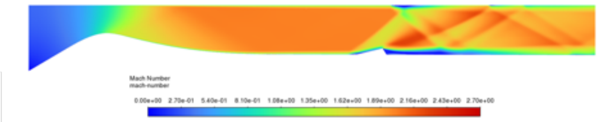

Figure 15: Accurate Geometry Cooling Mach Contour

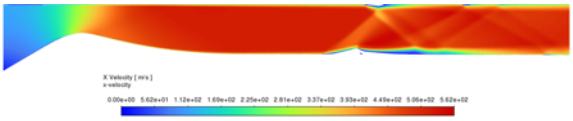

Figure 16: Accurate Geometry Cooling X-Velocity Contour

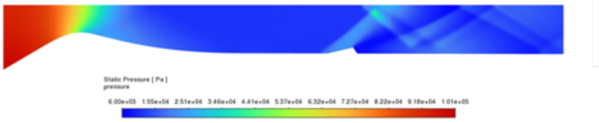

Figure 17: Accurate Geometry Cooling Pressure Contour

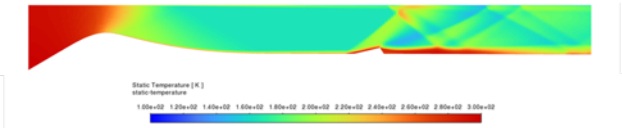

Figure 18: Accurate Geometry Cooling Temperature Contour

Furthermore, for the cooling case, the heat flux through the cooling wall was found. This plot can be seen in Figure 19.

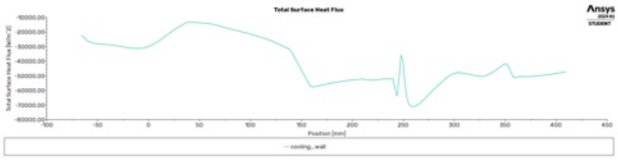

Figure 19: Heat Flux through Cooling wall for Accurate Geometry Cooling Case

For the cooling case, the interaction length was found to be 10.52 mm. The heat flux for the case with accurate geometry and cooling was also found through Ansys Fluent. This is seen in Figure 20, plotted along with the relevant experimental data. Note that the heat flux values in Figure 19 are negated; this is done by the simulation in order to denote direction. As such, Figure 20 considers only the magnitude of the heat flux.

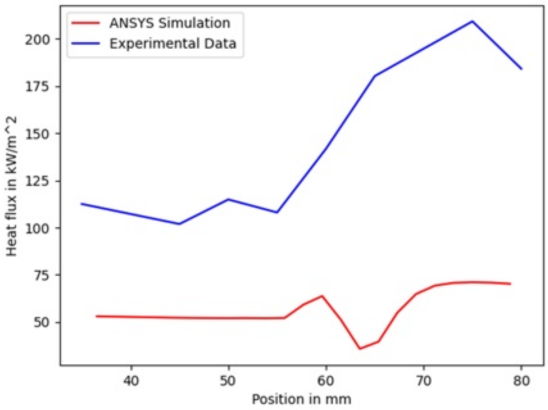

Figure 20: Heat Flux vs. Position

The simulated contour plots for the adiabatic case for the alternate wind tunnel geometry are shown in Figures 21-24.

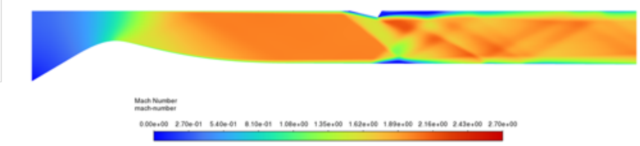

Figure 21: Alternate Geometry Adiabatic Mach Contour

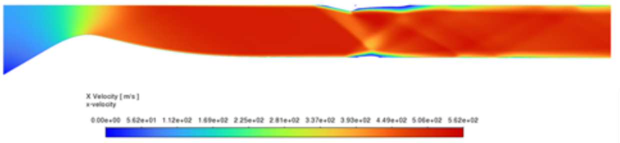

Figure 22: Alternate Geometry Adiabatic X-Velocity Contour

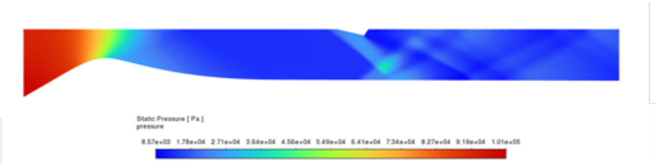

Figure 23: Alternate Geometry Adiabatic Pressure Contour

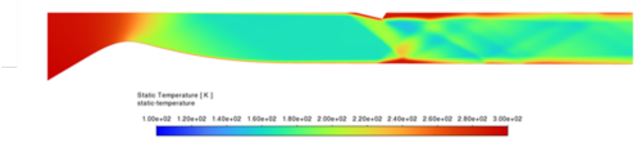

Figure 24: Alternate Geometry Adiabatic Temperature Contour

The simulated contour plots for the cooling case for the alternate wind tunnel geometry are shown in Figures 25-28.

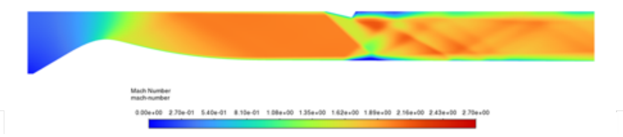

Figure 25: Alternate Geometry Cooling Mach Contour

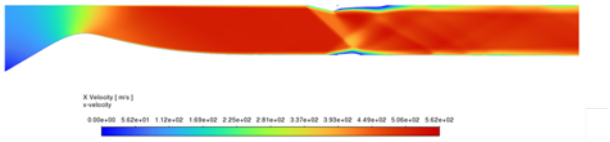

Figure 26: Alternate Geometry Cooling X-Velocity Contour

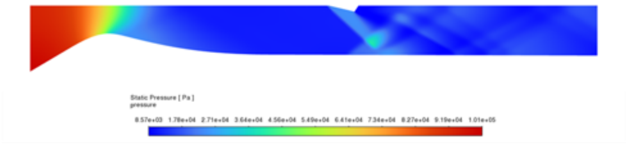

Figure 27: Alternate Geometry Cooling Pressure Contour

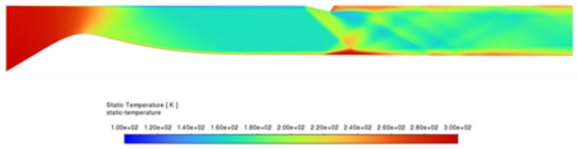

Figure 28: Alternate Geometry Cooling Temperature Contour

For both cases studying the alternate geometry, the interaction length was found to be 68.57 mm.

4. DISCUSSION

For all of the Mach number contour plots, the blue regions along both the bottom and the cooling walls represent the regions in which SWBLI occurs. Further, in the X-velocity plots, the white regions within these blue regions represent areas in which recirculation occurs. This is because the minimum boundary for X-velocity is set to zero, and as such, any region with negative values (which are indicative of recirculation) are not shown in color.

When comparing the temperature contours in the adiabatic cases with their corresponding cooling case counterparts, it can be seen that wall cooling largely eliminates the heat generated by the SWBLI, which is as to be expected.

4.1 ACCURATE GEOMETRY

In order to monitor the accuracy of the simulation for the accurate geometry cases, the y-plus value is monitored. It is important that the y-plus value within the regions wherein SWBLI occurs be sufficiently small as to accurately capture what occurs within this region [6]. This value is plotted for both the bottom and the cooling wall for the adiabatic and cooling case. These plots can be found in Figures 29-30.

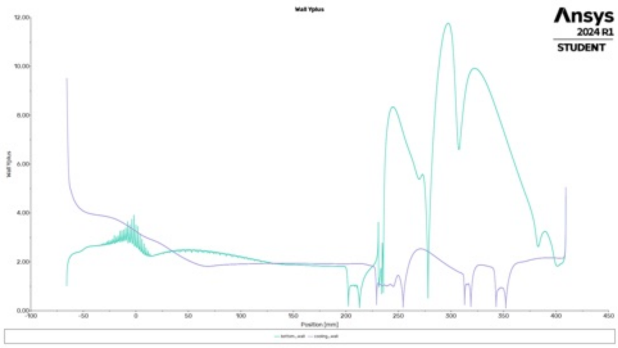

Figure 29: Y-Plus Values for Accurate Geometry Adiabatic Case

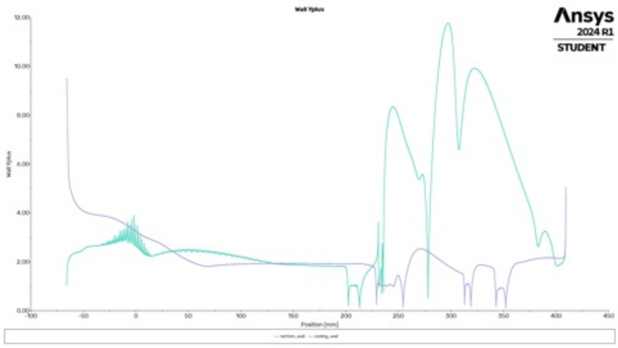

Figure 30: Y-Plus Values for Accurate Geometry Cooling Case

The y-plus values within the SWBLI regions were found to be sufficiently small for these purposes, however, the total accuracy of the simulation could be improved if the y-plus value could be lowered further, such that its value over the entire computational domain would be less than 1. Unfortunately, this is limited by the mesh size and what the computer can feasibly run without causing problems with the Ansys Fluent software. As such, the y-plus values in this case are the lowest they can be with the resources available.

The variation between the adiabatic and cooled cases was calculated. This data can be seen in Table 3.

Table 3: Accurate Geometry Interaction Length (mm)

Adiabatic Wall	Cooled Wall	Variation
54.33	43.81	10.52

As shown in Table 3, the interaction length of the SWBLI decreases when wall cooling is introduced. This particular simulation shows about a 19.36% decrease between these cases, which demonstrates that cryogenic wall cooling has a significant impact on the mitigation of the SWBLI. Further, in the schlieren imaging shown in Figures 6 and 7, the separation length, L_{sep}, can be seen to visually decrease in size when cooling is applied.

As shown in Figure 20, there exists a great discrepancy between the heat flux values calculated experimentally and the heat flux values calculated numerically. The experimental heat flux values are consistently higher than that of the numerical heat flux values. There are a few possible explanations for this discrepancy. For instance, when considering the model for the numerical simulations, the boundary layer is modeled as fully turbulent. Thus, the simulation does not take into account the physical reality of the boundary layer's transition from laminar, to transitional, to turbulent. This could lead to the discrepancy in the experimental and numerical values. Another possible suggestion is that the experimentally calculated resistance value could be incorrect, which in turn would lead to the calculated wall thickness value to be incorrect. This would affect both the physical and numerical data.

The contours for the Mach number and the X-velocity for both the adiabatic and cooled cases were overlaid with the respective schlieren imaging to demonstrate the numerical and experimental capturing of complex flow structures. These can be found in Figures 31-34.

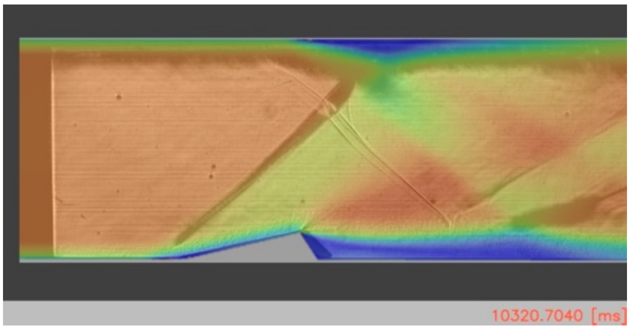

Figure 31: Adiabatic Wall Mach Number Contour Overlay

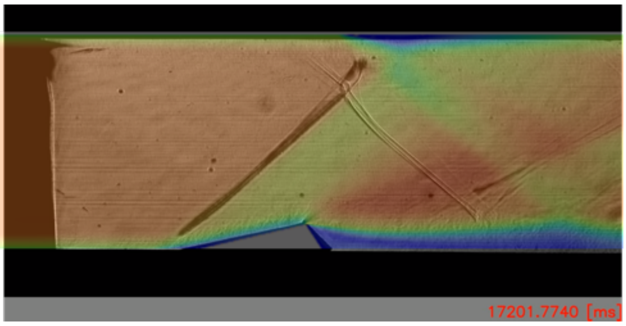

Figure 32: Cooled Wall Mach Number Contour Overlay

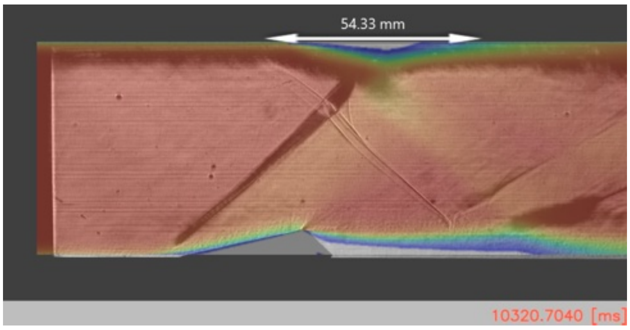

Figure 33: Adiabatic Wall X-Velocity Contour Overlay

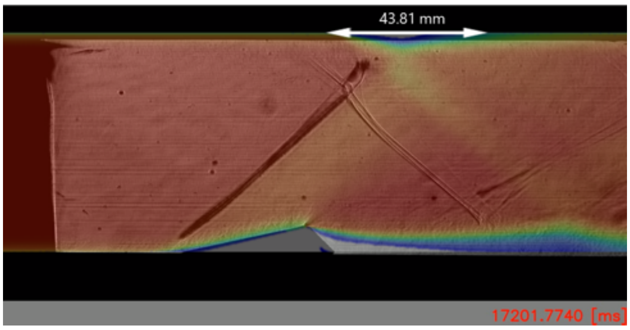

Figure 34: Cooled Wall X-Velocity Contour Overlay

From solely the Schlieren imaging, it can be difficult to find an exact value for the interaction length. It is much easier to get data points when considering the interaction length from a numerical perspective. The use of numerical simulation is useful to aid in the visualisation of the complex flow structures that form with a SWBLI, and also to visualize the contours of variables that are otherwise difficult to ascertain.

In all, more physical testing can be run to determine the accuracy of the resistance value. Also, more simulations of the SWBLI in the accurate geometry can be performed using laminar and transitional boundary layer models, to compare the results with the fully turbulent results.

4.2 ALTERNATE GEOMETRY

As with the accurate geometry case, the interaction length for the alternate geometry was found. This result can be seen in Table 4.

Table 4: Alternate Geometry Interaction Length (mm)

Adiabatic Wall	Cooled Wall	Variation
68.57	68.57	0

It is found that the interaction length for the alternate geometry is not altered within a reasonable scale. This is likely due to the SWBLI itself not taking place on the cooling wall. As such, the effects of such cooling are greatly diminished. However, it is of note to state that the numerical simulation run of this alternate geometry is not based on experimental values, as is the case with the accurate geometry. As such, in order to fully examine the effect of upstream cooling and alternate shock positions, physical testing should be performed.

5. CONCLUSION

Numerical and experimental analysis on the effect of cryogenic cooling on SWBLI in supersonic flow regimes was successfully performed. The experimental results allowed for a more accurate numerical recreation of the complex flow structures created as a result of SWBLI. The numerical results allowed for a clearer insight on the flow structures and flow variables such as temperature, pressure, and speed throughout the flow. This data is difficult to obtain through pure physical experimentation itself. It was found that the interaction length decreases by a significant percentage when cryogenic cooling is introduced.

In order to further study the effect of cooling on SWBLI, physical testing with the alternate geometry can be performed. Also, more simulations should be performed with different boundary layer models that replicate laminar, transitional, and turbulent boundary layers, in order to determine if this is the source of the heat flux discrepancy. In the same vein, more physical testing can be performed in order to determine if the value for wall resistance is accurate.

ACKNOWLEDGEMENTS

Sincerest thanks to the JUACEP program for providing this unique opportunity and to Nagoya University for providing the necessary resources for this research. I would also like to thank Professor Kinefuchi for welcoming me into his lab, as well as the lab members for being so hospitable and welcoming. Special thanks to Yuma Miki for his guidance.

REFERENCES

[1] V. Jaunet, J.F. Debieve, P. Dupont, Length Scales and Time Scales of a Heated Shock-Wave/Boundary-Layer Interaction, AIAA, (2014)

[2] Ke Zhu, Wall Temperature Effects on Shock Wave/Turbulent Boundary Layer Interaction via Direct Numerical Simulation, Acta Astronautica, (2020)

[3] Japan Aerospace Exploration Agency, Aerojet Engine Research, Research into hydrogen fuel application technology for aircraft and future space transport vehicles, JAXA, (online), available from: https://www.ard.jaxa.jp/research/hydrogenfuel/hydrogenfuel.html

[4] Yasuhiro, Egami et al., Development of New Two-Component Temperature-Sensitive Paint (TSP) for Cryogenic Testing, Measurement Science and Technology, 23(11):115301 (2012)

[5] Menter, F. R., "Zonal Two Equation k-ω Turbulence Models for Aerodynamic Flows", AIAA Paper 93-2906 (1993)

[6] Liepmann, H.W., Roshko, A., Elements of Gas Dynamics, (2002).

EDUCATIONAL EXPLORATION OF TOPOLOGY OPTIMIZATION: KEY CONCEPTS OF THE EXACT VOLUME CONSTRAINT METHOD

Raphaël Plante

Department of Mechanical Engineering, Polytechnique Montréal
`raphael-1.plante@polymtl.ca`

Supervisor: Toshiro Matsumoto

Graduate School of Engineering, Nagoya University
`t.matsumoto@nuem.nagoya-u.ac.jp`

ABSTRACT

Topology optimization is a pivotal tool in structural engineering, particularly with the rise of additive manufacturing. This research explores the exact volume constraint method in topology optimization, specifically through the implementation of reaction-diffusion equations as developed by Cui, Takahashi, and Matsumoto (2023) [1]. The study focuses on bridging the gap between established theoretical formulations and their practical applications by providing a detailed, step-by-step guide to the FreeFEM++ script used in these simulations. By clarifying complex mathematical concepts and offering practical insights, this paper serves as a resource for students and researchers, aiding in the understanding and application of existing topology optimization techniques.

Nomenclature	
χ_ϕ; Xi	Characteristic function; Elastic modulus like
$\phi_{(x)}$; phi	Level set function: geometry of material domain
H_2	Smoothed Heaviside function
$\mathcal{T}$; sens	Topological derivative: sensitivity
$\mathbb{P}$	Polarization tensor
$\mathrm{V_{req}}$	Volume constraint
ϕ^*; phi, phitemp	Intermediate level set function
$\hat{\phi}$; dphi(s)	Pre-solved level set function
$\tilde{\phi}$; vdphis, vphi	Test function

Key Mathematical Concepts

Divergence theorem [2]

$$\int_\Gamma \vec{q}\cdot\vec{n}\ ds = \int_\Omega \nabla\cdot\vec{q}\ d\Omega \tag{1}$$

Gradient Power Rule [3]

$$\nabla\cdot(fg) = (\nabla f)\cdot g + f(\nabla\cdot g) \tag{2}$$

Second Order Identity tensor

$$\mathrm{I} = \begin{bmatrix} 1 & 0 \\ 0 & 1 \end{bmatrix} \tag{3}$$

Fourth Order Identity tensor [4]

$$\mathbb{I}_{ijkl} = \frac{1}{2}\left(\delta_{ik}\delta_{jl} + \delta_{il}\delta_{jk}\right) \tag{4}$$

$$\begin{cases} \mathbb{I}_{ij11} = \frac{1}{2}\begin{bmatrix} 2 & 0 \\ 0 & 0 \end{bmatrix} \\ \mathbb{I}_{ij21} = \mathbb{I}_{ij12} = \frac{1}{2}\begin{bmatrix} 0 & 1 \\ 1 & 0 \end{bmatrix} \\ \mathbb{I}_{ij22} = \frac{1}{2}\begin{bmatrix} 0 & 0 \\ 0 & 2 \end{bmatrix} \end{cases} \tag{5}$$

Nabla

$$\nabla = \frac{\partial}{\partial x} + \frac{\partial}{\partial y} + \frac{\partial}{\partial z} \tag{6}$$

Tensor product [5]

$$\mathrm{I}\otimes\mathrm{I}_{ijkl}:\ \delta_{ij}\delta_{kl} \tag{7}$$

Double dot product

$$A\!:\!B = \sum_{i=1}^{2}\sum_{j=1}^{2} a_{ij}b_{ij} \tag{8}$$

1. INTRODUCTION

Topology optimization has become an indispensable technique in structural engineering and design, particularly with the increasing use of additive manufacturing. The ability to optimize material distribution within a given design space allows engineers to create structures that are both lightweight and strong [6]. However, implementing these optimization methods, especially those involving exact volume constraints, can be challenging due to the complex mathematics and computational requirements involved.

This paper focuses on the exact volume constraint method for topology optimization, implemented via reaction-diffusion equations as described by Cui, Takahashi, and Matsumoto (2023) [1]-[7]. Although the theoretical foundation of this method is robust, its practical application can be daunting, especially for those new to the field. Significant challenges often arise in understanding and applying these concepts, particularly due to the steep learning curve associated with topology optimization and finite element methods (FEM). Navigating through the complex equations and corresponding FreeFEM++ scripts may reveal discrepancies and gaps in understanding that can hinder progress.

To address these challenges, this paper provides a comprehensive explanation of the exact volume constraint method, focusing on practical implementation. Through a detailed breakdown of the FreeFEM++ script, the report aims to demystify the equations and concepts, making them accessible to both students and researchers. This work does not introduce new methods but rather serves as an educational resource that facilitates a smoother transition from theory to application in the field of topology optimization, clarifying common questions and addressing challenges that may arise during the application of this method.

2. DEFINITIONS

Reaction-Diffusion Equation: An RDE describes the behavior of the concentration of a substance as it undergoes reactions and diffuses through space. Specifically, the RDE in the context of the method is:

$$\frac{\partial \phi}{\partial t} = K(-\mathcal{T} + \Lambda + \tau \nabla^2 \phi) \qquad (9)$$

Level set function (ϕ): Used to describe the geometry of the material domain.

$\partial\phi\ /\partial t$: This term represents the rate of change of the level set function ϕ with respect to time.

Topological Derivative ($\mathcal{T}$): A crucial concept in topology optimization, the topological derivative quantifies how the objective function changes when an infinitesimal amount of material is removed at a certain point in the design domain. This derivative serves as a sensitivity measure, guiding the optimization process by indicating the regions where material should be added or removed to improve the design.

Lagrangian multiplier (Λ): Used to enforce the volume constraint during the optimization process. It adjusts the evolution of the level set function ϕ to maintain the desired material volume.

Regularization Term ($\tau\nabla^2\phi$): The diffusion term $\nabla^2\phi$ introduces a smoothing effect to the evolution of ϕ, helping to maintain a smooth boundary between material and void regions and preventing numerical instabilities. The parameter τ controls the strength of this smoothing effect.

Parameter (K): This is a coefficient of proportionality that affects the speed at which the level set function evolves.

Objective function ($F(\phi)$): Equation (10) represents the work done by the external forces t on the structure. Minimizing this work is equivalent to minimizing the compliance of the structure.

$$F(\phi) = \int_{\Gamma_N} t \cdot u \ \mathrm{d}\Gamma \qquad (10)$$

Governing equation $\big(a(u,v)\big)$: Equation (11) defines the physical behavior of the system under given loads and boundary conditions

$$a(u,v) = \int_D \varepsilon(u) : \mathbb{C} : \varepsilon(v) \, \mathrm{d}\Omega \qquad (11)$$

Volume constraint ($G(\phi)$): Equation (12) represent the volume constraint. It states that the total material volume present in the design domain must be smaller or equal to the allowed volume.

$$G(\phi) = \int_D \chi_\phi \mathrm{d}\Omega - \mathrm{V}_{\mathrm{req}} \leq 0 \qquad (12)$$

Smoothed Heaviside function (H_i): A function that gradually approaches the rigorous Heaviside function. This can improve material connectivity in the domain at early stages.

Weak form of an equation: A reformulation of a differential equation into an equivalent integral equation suitable for numerical solution, useful for the finite element method. It often involves integration by parts and is multiplied by a test function.

Test function: Function used in the weak form to test the equation. It belongs to the same space as the solution. It ensures that the trial solution adheres to the specified boundary conditions. FreeFEM handles this internally (see Listing 1).

3. SCRIPT FOR EXACT VOLUME METHOD

The implementation of the exact volume constraint method for topology optimization involves a detailed computational process that translates complex mathematical principles into a working program. This section provides a comprehensive walkthrough of the FreeFEM++ script used in this study to enforce exact volume constraints within the framework of topology optimization, handling the dynamic redistribution of material in a design domain.

The script ensures that the optimization process not only improves structural performance but also adheres strictly to the prescribed volume constraints. By leveraging the reaction-diffusion equation, the material distribution is iteratively evolved, guided by the topological derivative, to achieve an optimal design.

The script is broken down step-by-step, explaining the purpose and function of each segment, including the definition of finite element spaces, the initialization and evolution of the level set function, and the implementation of the reaction-diffusion equation to drive the optimization process. Additionally, the exact volume constraint is maintained throughout the iterations, facilitated by the FreeFEM++ environment, which manages this complex computation.

3.1 Pre-Optimization Setup

```
// Define the Finite element space
fespace Vh(Th,[P1,P1]);
Vh [u1,u2],[v1,v2];
fespace Vh1(Th0,P2);
Vh1 phi, vphi, oldphi,
phierror,aprxsign,Xi,midxi,phitemp; //RD
solution
fespace Vh2(Th0,P2);
Vh2 dphis, vdphis;
```

Listing 1: Finite element spaces

Listing 1 defines the finite element spaces, which serve as the foundation for the entire optimization process. Finite element spaces are defined to represent the variables and their associated functions [8], such as displacements and the level set function, which will be manipulated throughout the optimization. Here, *Vh*, *Vh1*, and *Vh2* are the finite element spaces created over meshes *Th* and *Th0* using linear (P1) and quadratic (P2) elements. These spaces will accommodate the primary variables and their test functions necessary for solving the problem within FreeFEM++.

With the finite element spaces established, the script proceeds to initialize the parameters required for the optimization process. This initialization sets up the design domain's volume, which plays a crucial role in enforcing the volume constraint during the optimization.

```
// Initial  parameter of Optimization process
real V0 = int2d(Th)(1.);
```

Listing 2: Design domain volume

Listing 2 initializes the variable *V0*, representing the total initial volume of the design domain. Calculating this volume is essential as it serves as a reference for the volume constraint that will be enforced throughout the optimization.

With the design domain's volume established, the next step involves formulating the reaction-diffusion equation, which governs the evolution of the level set function. This equation plays a pivotal role in controlling the material distribution within the design domain.

```
//Predefined field
solve RDE0(dphis,vdphis,solver=CG) =
int2d(Th0)(dphis*vdphis+dt*tao*Kappa*(dx(dphis)*
dx(vdphis)+dy(dphis)*dy(vdphis)))
-int2d(Th0)(0*vdphis+dt*Kappa*vdphis)
+on(3,dphis=0);
```

Listing 3: Weak form of $\hat{\phi}$

Listing 3 is the developed weak form of $\hat{\phi}$ that satisfies the initial boundary value problem [1][7]. As mentioned by the author, it is a one-time cost, as it is not use in the optimization loop. This formulation uses the finite element spaces defined earlier and integrates the terms over the domain. To better understand the origin of the weak form, a demonstration is presented in (17).

To get to the weak form, it is necessary to use initial boundary values found in equation (15) and the introduction of (13) as a way to work around the unknown Lagrangian multiplier.

$$\phi = \phi^{*} + \Lambda\hat{\phi} \qquad (13)$$

This specific FreeFEM scripts uses Gmsh to generate the mesh, using a script in Fortran. In this script, boundaries are labeled using numbers: label 1 for fixed boundary (Dirichlet), label 3 for traction boundary.

$$\frac{\partial\hat{\phi}}{\partial t} = K(1+\tau\nabla^{2}\hat{\phi}) \qquad (14)$$

$$\begin{cases} \dfrac{\partial\hat{\phi}}{\partial n} = 0 & on\ \dfrac{\partial D}{\partial\Gamma_N} \\ \hat{\phi} = 1 & on\ \partial\Gamma_N \\ \hat{\phi}\big|_t = 0 & \end{cases} \qquad (15)$$

The Dirichlet boundary condition, shown last in equation (15) is applied in the code using *on(3,dphis=0)*.

Adding test function on both sides: $\qquad$ (16)

$$\tilde{\phi}\frac{\partial\hat{\phi}}{\partial t} = \tilde{\phi}K(1+\tau\nabla^{2}\hat{\phi})$$

Integration over the domain:

$$\int_D \tilde{\phi}\frac{\partial\hat{\phi}}{\partial t} - \tilde{\phi}K - \tilde{\phi}K\tau\nabla^{2}\hat{\phi}\, d\Omega = 0$$

$$\int_D \tilde{\phi}\frac{\hat{\phi}\big|_{t+\Delta t} - \hat{\phi}\big|_t}{\Delta t} - \tilde{\phi}K - K\tau\tilde{\phi}\nabla\cdot(\nabla\hat{\phi})d\Omega = 0$$

Using gradient rule (equation (2)) and condition to remove $\hat{\phi}\big|_t$ in (15):

$$\int_D \tilde{\phi}\frac{\hat{\phi}\big|_{t+\Delta t}}{\Delta t} - \tilde{\phi}K\, d\Omega - \int_\Omega K\tau\left[\nabla\cdot(\tilde{\phi}\nabla\hat{\phi}) - (\nabla\tilde{\phi})(\nabla\hat{\phi})\right] d\Omega = 0 \qquad (17)$$

Using divergence theorem (equation (1)) and condition of $\frac{\partial\hat{\phi}}{\partial n}$ in (15) :

$$\int_D \tilde{\phi}\frac{\hat{\phi}\big|_{t+\Delta t}}{\Delta t} - \tilde{\phi}K\, d\Omega + \int_D K\tau\left[(\nabla\tilde{\phi})(\nabla\hat{\phi})\right] d\Omega - \int_\Gamma K\tau\left[\nabla\cdot(\tilde{\phi}\nabla\hat{\phi})\cdot n\right] dS = 0$$

Final equation found in the script:

$$\int_D \hat{\phi}\big|_{t+\Delta t}\tilde{\phi} + \Delta t K\tau\left[(\nabla\tilde{\phi})(\nabla\hat{\phi})\right] - \Delta t K\tilde{\phi}\, d\Omega = 0 \qquad (18)$$

Once the pre-solved level set function has been found, the script must ensure that the material distribution leads to a structurally sound design. This is accomplished by performing stress analysis, which checks the equilibrium of the structure under the current material layout.

```
// Stress analysis
problem elasticity(u1,u2,v1,v2,solver=CG) =
int2d(Th)(mu*(2*dx(u1)*dx(v1)+2*dy(u2)*dy(v2)+dy
(u1)*dx(v2)+dx(u2)*dy(v1)+dy(u1)*dy(v1)+dx(u2)*d
x(v2))+lambda*(dx(u1)+dy(u2))*(dx(v1)+dy(v2)))-
int1d(Th,3)(f1*v1+f2*v2)+on(1,u1=0,u2=0);
```

Listing 4: Stress Equilibrium

Listing 4 defines the stress equilibrium problem, which is critical for ensuring that the structure can withstand applied loads. The script sets up the governing equation for elasticity, using the material properties (represented by *mu* and *lambda*) and the current displacement fields (*u1* and *u2*). This equation comes from the equilibrium of the objective function and the governing equation, where the internal virtual work due to the deformation must balance the external virtual work done by the applied tractions. From the starting equilibrium equation (19):

$$\int_D \varepsilon(u) : \mathbb{C} : \varepsilon(v)\, \mathrm{d}\Omega = \int_{\Gamma_N} t\cdot v\ \mathrm{d}\Gamma \qquad (19)$$

With the strain for the displacement being:

$$\varepsilon(u) = \begin{bmatrix} \dfrac{\partial u_1}{\partial x} & \dfrac{1}{2}\left(\dfrac{\partial u_1}{\partial y} + \dfrac{\partial u_2}{\partial x}\right) \\ \dfrac{1}{2}\left(\dfrac{\partial u_1}{\partial y} + \dfrac{\partial u_2}{\partial x}\right) & \dfrac{\partial u_2}{\partial y} \end{bmatrix} \qquad (20)$$

The fourth order elasticity tensor $\mathbb{C}$ can be rewritten [9] as: $\qquad$ (21)

$$C_{ijkl} = \lambda\delta_{ij}\delta_{kl} + \mu\left(\delta_{ik}\delta_{jl} + \delta_{il}\delta_{jk}\right)$$

And visualised with:

$$C_{ij11} = \begin{bmatrix} \lambda+2\mu & 0 \\ 0 & \lambda \end{bmatrix},\ C_{ij21} = C_{ij12} = \begin{bmatrix} 0 & \mu \\ \mu & 0 \end{bmatrix} \qquad (22)$$

$$C_{ij22} = \begin{bmatrix} \lambda & 0 \\ 0 & \lambda+2\mu \end{bmatrix}$$

The results of the dot products yield the weak form used in the script:

$$\int_D \mu\left[2\frac{\partial u_1}{\partial x}\frac{\partial v_1}{\partial x}+2\frac{\partial u_2}{\partial y}\frac{\partial v_2}{\partial y}+\left(\frac{\partial u_1}{\partial y}+\frac{\partial u_2}{\partial x}\right)\left(\frac{\partial v_1}{\partial y}+\frac{\partial v_2}{\partial x}\right)\right]+\lambda\left[\left(\frac{\partial u_1}{\partial x}+\frac{\partial u_2}{\partial y}\right)\left(\frac{\partial v_1}{\partial x}+\frac{\partial v_2}{\partial y}\right)\right]\,\mathrm{d}\Omega\ -\ \int_{\Gamma_N} f_1 v_1+f_2 v_2\ \mathrm{d}\Gamma=0 \tag{23}$$

With the structural equilibrium established, the next step is to perform sensitivity analysis using the topological derivative. This analysis determines how the objective function responds to changes in the material distribution, guiding the optimizer on where to adjust the material layout.

```
//Sensitivity Analysis
func sens =
1./(1.+nu)*((4.*mu*(dx(u1)^2+dy(u2)^2+2.*(dx(u2)
/2.+dy(u1)/2.)^2)+(2.*mu-(1.-3.*nu)/2./(1.-
nu)*(2.*mu+2.*lambda))*(dx(u1)+dy(u2))^2));
```

Listing 5: Sensitivity analysis

Listing 5 presents the sensitivity analysis, which is the most complex equation to visualize for the common user. For this reason, the following part as a purpose to clarify certain concepts.

"The topological derivative measures the sensitivity of a given shape functional with respect to an infinitesimal singular domain perturbation, such as the insertion of holes, inclusions, source-terms or even cracks"[10]. The sensitivity function (*sens*) incorporates the strain energy density and the material properties (*mu* and *nu*). For the proposed method, the topological derivative can be written as equation (24)

$$\mathcal{T}=-\sigma\ :\ \mathbb{P}\ :\ \varepsilon \tag{24}$$

Hooke's law states that for a continuous media [11], the stress tensor can be written as:

$$\sigma_{ij}=\sum_{k=1}^{2}\sum_{l=1}^{2}C_{ijkl}\varepsilon_{kl} \tag{25}$$

$$\sigma=\begin{bmatrix}(\lambda+2\mu)\dfrac{\partial u_1}{\partial x}+\lambda\dfrac{\partial u_2}{\partial y} & \mu\left(\dfrac{\partial u_1}{\partial y}+\dfrac{\partial u_2}{\partial x}\right)\\ \mu\left(\dfrac{\partial u_1}{\partial y}+\dfrac{\partial u_2}{\partial x}\right) & (\lambda+2\mu)\dfrac{\partial u_2}{\partial y}+\lambda\dfrac{\partial u_1}{\partial x}\end{bmatrix} \tag{26}$$

The polarization tensor $\mathbb{P}$ is a mathematical concept used in the characterization of the effect of the insertion of a perturbation. It describes the change of state of the material in an elastic solid [12]. It can be found as:

$$\mathbb{P}=\frac{1}{1+\nu}\left(2\mathbb{I}-\frac{1-3\nu}{2(1-\nu)}\mathrm{I}\otimes\mathrm{I}\right) \tag{27}$$

With the introduction of the fourth-order identity tensor (4), and the tensor product (7), it is possible to visualize the polarization tensor as equation (28).

$$\begin{aligned}\mathbb{P}_{ij11}&=\frac{1}{1+\nu}\left(\begin{bmatrix}2&0\\0&0\end{bmatrix}-\frac{1-3\nu}{2(1-\nu)}\begin{bmatrix}1&0\\0&1\end{bmatrix}\right)\\ \mathbb{P}_{ij21}=\mathbb{P}_{ij12}&=\frac{1}{1+\nu}\begin{bmatrix}0&1\\1&0\end{bmatrix}\\ \mathbb{P}_{ij22}&=\frac{1}{1+\nu}\left(\begin{bmatrix}0&0\\0&2\end{bmatrix}-\frac{1-3\nu}{2(1-\nu)}\begin{bmatrix}1&0\\0&1\end{bmatrix}\right)\end{aligned} \tag{28}$$

By breaking equation (24) into smaller operations (29)-(31), we can obtain (33):

$$W_{ij}=\sum_{k=1}^{2}\sum_{l=1}^{2}\mathbb{P}_{ijkl}\sigma_{kl} \tag{29}$$

$$\begin{aligned}W_{11}&=\\ &\frac{1}{1+\nu}\left(2-\frac{1-3\nu}{2(1-\nu)}\right)\left((\lambda+2\mu)\frac{\partial u_1}{\partial x}+\lambda\frac{\partial u_2}{\partial y}\right)\\ &\quad+\frac{1}{1+\nu}\left(-\frac{1-3\nu}{2(1-\nu)}\right)\left((\lambda+2\mu)\frac{\partial u_2}{\partial y}+\lambda\frac{\partial u_1}{\partial x}\right)\\ W_{12}=W_{21}&=\frac{1}{1+\nu}\left(2\mu\left(\frac{\partial u_1}{\partial y}+\frac{\partial u_2}{\partial x}\right)\right)\\ W_{22}&=\\ &\frac{1}{1+\nu}\left(-\frac{1-3\nu}{2(1-\nu)}\right)\left((\lambda+2\mu)\frac{\partial u_1}{\partial x}+\lambda\frac{\partial u_2}{\partial y}\right)\\ &\quad+\frac{1}{1+\nu}\left(2-\frac{1-3\nu}{2(1-\nu)}\right)\left((\lambda+2\mu)\frac{\partial u_2}{\partial y}+\lambda\frac{\partial u_1}{\partial x}\right)\end{aligned} \tag{30}$$

$$\mathcal{T}=W\!:\varepsilon \tag{31}$$

By using the double dot product (8):

$$\begin{aligned}\mathcal{T}=&\frac{1}{1+\nu}\frac{\partial u_1}{\partial x}\left(2-\frac{1-3\nu}{2(1-\nu)}\right)\left((\lambda+2\mu)\frac{\partial u_1}{\partial x}+\lambda\frac{\partial u_2}{\partial y}\right)\\ &\quad+\frac{1}{1+\nu}\frac{\partial u_1}{\partial x}\left(-\frac{1-3\nu}{2(1-\nu)}\right)\left((\lambda+2\mu)\frac{\partial u_2}{\partial y}+\lambda\frac{\partial u_1}{\partial x}\right)\\ &+\frac{1}{1+\nu}\frac{1}{2}\left(\frac{\partial u_1}{\partial y}+\frac{\partial u_2}{\partial x}\right)\left(2\mu\left(\frac{\partial u_1}{\partial y}+\frac{\partial u_2}{\partial x}\right)\right)\\ &+\frac{1}{1+\nu}\frac{1}{2}\left(\frac{\partial u_1}{\partial y}+\frac{\partial u_2}{\partial x}\right)\left(2\mu\left(\frac{\partial u_1}{\partial y}+\frac{\partial u_2}{\partial x}\right)\right)\\ &+\frac{1}{1+\nu}\frac{\partial u_2}{\partial y}\left(-\frac{1-3\nu}{2(1-\nu)}\right)\left((\lambda+2\mu)\frac{\partial u_1}{\partial x}+\lambda\frac{\partial u_2}{\partial y}\right)\\ &\quad+\frac{1}{1+\nu}\frac{\partial u_2}{\partial y}\left(2-\frac{1-3\nu}{2(1-\nu)}\right)\left((\lambda+2\mu)\frac{\partial u_2}{\partial y}\right.\\ &\quad\left.+\lambda\frac{\partial u_1}{\partial x}\right)\end{aligned} \tag{32}$$

The equation can simply be reduced to the one in the script:

$$\mathcal{T}=\frac{1}{1+\nu}\left(2\mu\left(2\left(\left(\frac{\partial u_1}{\partial x}\right)^2+\left(\frac{\partial u_2}{\partial y}\right)^2\right)\right.\right.$$
$$\left.+\left(\frac{\partial u_1}{\partial y}+\frac{\partial u_2}{\partial x}\right)^2+\left(\frac{\partial u_1}{\partial x}+\frac{\partial u_2}{\partial y}\right)^2\right)$$
$$\left.+\left(-\frac{1-3\nu}{2(1-\nu)}\right)(2\mu\ +2\lambda)\left(\frac{\partial u_1}{\partial x}+\frac{\partial u_2}{\partial y}\right)^2\right) \quad (33)$$

Following the sensitivity analysis, the script iteratively updates the level set function to adjust the material distribution based on the sensitivity information. This iterative process is key to refining the design and moving closer to the optimal solution.

```
//Define phi RDE
problem RDE(phi,vphi,solver=CG) =
int2d(Th0)(phi*vphi+dt*tao*Kappa*(dx(phi)*dx(vph
i)+dy(phi)*dy(vphi)))-int2d(Th0)(oldphi*vphi)-
int2d(Th)(dt*Kappa*senscoef*sens*vphi)+on(3,phi=
1);
```

Listing 6: Weak form Reaction-Diffusion Equation of $\boldsymbol{\phi}^*$

Listing 6 presents the weak form of the RDE, used in the iterative update of the level set function ϕ based on the sensitivity analysis. Using conditions shown in (35), it is possible to demonstrate how to go from equation (34) to equation (38), which is the one used in the script.

$$\frac{\partial\phi^*}{\partial t}=K(-\bar{\mathcal{T}}+\tau\nabla^2\phi^*) \quad (34)$$

Boundary conditions

$$\begin{cases}\dfrac{\partial\phi^*}{\partial n}=0 & on\ \dfrac{\partial D}{\partial\Gamma_N}\\ \phi^*=1 & on\ \partial\Gamma_N\\ \phi^*|_t=\phi|_t & \end{cases} \quad (35)$$

$$\tilde{\phi}\frac{\partial\phi^*}{\partial t}=\tilde{\phi}K(-\bar{\mathcal{T}}+\tau\nabla^2\phi^*) \quad (36)$$

$$\int_D\tilde{\phi}\frac{\partial\phi^*}{\partial t}+\ \tilde{\phi}K\bar{\mathcal{T}}\ -\tilde{\phi}K\tau\nabla^2\phi^*d\Omega=0 \quad (37)$$

$$\int_D\tilde{\phi}\frac{\phi^*|_{t+\Delta t}-\phi^*|_t}{\Delta t}+\ \tilde{\phi}K\bar{\mathcal{T}}$$
$$-K\tau\tilde{\phi}\nabla\cdot(\nabla\phi^*)d\Omega=0$$

Using equation (2) and (**35**):

$$\int_D\tilde{\phi}\frac{\phi^*|_{t+\Delta t}-\phi|_t}{\Delta t}+\ \tilde{\phi}K\bar{\mathcal{T}}\ d\Omega$$
$$-\int_\Omega K\tau\left[\nabla\cdot(\tilde{\phi}\nabla\phi^*)-(\nabla\tilde{\phi})(\nabla\phi^*)\right]d\Omega$$
$$=0$$

Using equation (1) and (35):

$$\int_D\tilde{\phi}\frac{\phi^*|_{t+\Delta t}-\phi|_t}{\Delta t}+\ \tilde{\phi}K\bar{\mathcal{T}}\ d\Omega$$
$$+\int_D K\tau\left[\left(\nabla\tilde{\phi}\right)(\nabla\phi^*)\right]d\Omega$$
$$-\int_\Gamma K\tau\left[\nabla\cdot(\tilde{\phi}\nabla\phi^*)\cdot n\right]dS=0$$

$$\int_D\phi^*|_{t+\Delta t}-\phi|_t\,\tilde{\phi}\ +\ \Delta tK\bar{\mathcal{T}}\tilde{\phi}$$
$$+\Delta tK\tau\left[\left(\nabla\tilde{\phi}\right)(\nabla\phi^*)\right]d\Omega\ =0 \quad (38)$$

Before entering the main optimization loop, two critical variables, alpha and phi, need to be initialized.

```
oldphi =1.0 ;
alpha=1.0;
```

Listing 7: Initialization of alpha and phi

Listing 7 initializes the variables *oldphi* and *alpha*. The variable *oldphi* stores the initial value of the level set function phi, representing the material distribution before any iteration has taken place. *Alpha* is set to 1.0, representing the initial value of the volume constraint, which will be dynamically adjusted as the optimization progresses.

With the necessary equations and initial parameters established, the groundwork is set for implementing the topology optimization process. The following section will detail the iterative steps that guide the material distribution towards an optimized structure while adhering to the exact volume constraints.

3.2 Optimization Process

In the optimization process, the initialized parameters and equations drive the iterative updates of the level set function, progressively refining the design. This section outlines the loop structure, mesh updates, and convergence criteria that are critical to achieving the final optimized configuration.

```
while (change > 0.02 )
{    iter = iter+1; // Iteration
```

Listing 8: Beginning of the main loop

Listing 8 opens the main loop of the optimization process. The loop continues to iterate as long as the change in the level set function (*change*) is greater than a specified threshold. This threshold ensures that the optimization only stops when further changes become insignificant, indicating that the design has converged. The iteration counter *iter* is incremented with each pass through the loop.

As the loop progresses, the script continuously updates the level set function and the mesh, ensuring that the material distribution remains accurate as the design evolves.

```
// write phi --> mmg iso mesh --> read
mesh
savesol("phi.sol",Th0,oldphi,order=1);
exec("./Th02Th.x");
Th = readmesh("Th.msh");
```

Listing 9: Mesh generation

Listing 9 updates the level set function (*phi*), saves it to a solution file (*phi.sol*), and then generates a new mesh based on the updated level set function. The command *exec("./Th02Th.x")* executes an external script that generates the new mesh, which is then read back into the script with *readmesh("Th.msh")*. This step is needed for refining the mesh to match the evolving material distribution.

With the updated mesh, the script performs stress analysis and recalculates the sensitivity function. These recalculations guide the next iteration of the optimization process.

```
elasticity;
    senscoef=0.5*V0/int2d(Th)(abs(sens));
        RDE;
    objective = int1d(Th,3)(f1*u1+f2*u2);
```

Listing 10: Calling of stress analysis, RDE, objective function

Listing 10 calls the previously defined elasticity problem (*elasticity*), recalculates the sensitivity coefficient (*senscoef*), and solves the reaction-diffusion equation (*RDE*) again based on the updated sensitivity information. *Senscoef* represents the normalized topological derivative (equation (39)). The objective function (equation (10)) is recalculated using the updated material layout. The integral is applied for the traction boundary, labeled #3 in *Gmsh*.

$$\begin{cases} \bar{\mathcal{T}} = C_0\mathcal{T} \\ C_0 = \dfrac{\int_D d\Omega}{2\int_D |\mathcal{T}|\, d\Omega} = \dfrac{0.5V_0}{\int_D |\mathcal{T}|\, d\Omega} \end{cases} \qquad (39)$$

The script now adjusts the volume constraint to ensure that the optimization respects the predefined material volume while continuing to improve the structural performance.

```
real k=iter^0.5+1.0;
        alpha=max(alpha0,alpha*0.96);
    phitemp=phi;
    phi=phitemp+Blamda*dphis;
```

Listing 11: Calling k, alpha and phitemp

Listing 11 adjusts the variables *alpha*, *k*, and *phi*. The parameter *alpha* is gradually reduced by multiplying it by 0.96 in each iteration, allowing the material distribution to converge towards the desired volume, but gradually to avoid material separation. The variable *k* is used to scale the value of the characteristic function over the iteration process, while *phitemp* temporarily stores the level set function phi before it is updated, in the same form as equation (13). These adjustments help maintain a smooth and controlled optimization process.

After adjusting *alpha* and *phi*, the script enforces boundaries on the level set function, ensuring that it stays within predefined limits.

```
    phi = min(1.0,phi);
    phi = max(-1.0,phi);
```

Listing 12: Applying boundaries on phi

Listing 12 applies boundaries to *phi*. First taking the minimum of present *phi* and 1.0. At this point, *phi* can be no more than 1. Next line, *phi* is the maximum of *phi* and -1.0. At this point *phi* can be no more than 1.0 and no less than -1.0. *Phi* can now be classified using equation (40), as either the material domain, the material boundary or finally the complementary void domain.

$$\begin{cases} 0 < \phi_{(x)} \leq 1 & \text{for } \boldsymbol{x} \in \Omega \\ \phi_{(x)} = 0 & \text{for } \boldsymbol{x} \in \partial\Omega \\ -1 \leq \phi_{(x)} < 0 & \text{for } \boldsymbol{x} \in D\backslash\Omega \end{cases} \qquad (40)$$

With the level set function bounded, the script updates the characteristic function, which defines the material regions within the design domain based on the current level set function.

```
        Xi=max(0.0,tanh(k*phi));
    ratio = int2d(Th0)(Xi)/V0;
        flamda = ratio-alpha;
    nri=0;
```

Listing 13: Updating the characteristic function

Listing 13 updates the characteristic function, *Xi.* A smoothed Heaviside function, here a hyperbolic tangent (equation (41)) smooths the transition between material and void regions, ensuring a realistic material distribution. The ratio of the material volume *(int2d(Th0)(Xi))* to the initial volume *(V0)* is calculated, and the difference between this ratio and the adjusted volume constraint (*alpha*) is stored in *flamda*.

$$\chi_{\phi} = H_1 = \max\left(0.0, \tanh(k\phi)\right) \qquad (41)$$

The script then uses the Newton-Raphson method to iteratively refine the volume constraint, ensuring that the material distribution converges to the desired volume.

```
while (abs(flamda)>1e-3*alpha)
    {
    nri=nri+1;
    phi=phitemp+Blamda*dphis;
    phi = min(1,phi);
    phi = max(-1,phi);

        Xi=max(0.0,tanh(k*phi));
    ratio = int2d(Th0)(Xi)/V0;
    flamda = ratio-alpha;
    Dflamda=int2d(Th0)((1.0-
(tanh(k*phi))^2.0)*k*dphis);
    Blamda=Blamda-flamda/Dflamda;
    }
```

Listing 14: Newton-Raphson for volume constraint

Listing 14 implements the Newton-Raphson method to refine the volume constraint iteratively. The loop continues until the difference *flamda* falls below a small tolerance, indicating that the volume constraint is sufficiently satisfied. During each iteration, the level set function *phi* is updated, and the characteristic function *Xi* is recalculated to ensure that the material distribution converges to the desired volume.

After refining the volume constraint, the script performs a final convergence check to determine if the optimization process has reached a stable solution.

```
    phierror = phi-oldphi;
    change = phierror[].linfty; // L-
infinity norm
    oldphi = phi;
    ratio2 = int2d(Th)(1.0)/V0;
```

Listing 15: Convergence of phi

Listing 15 performs the final convergence check by calculating the error in the level set function *(phierror)* by comparing the current and previous iterations. The L-infinity norm *(linfty)* of this error is computed (superior value of the array), and if the change falls below the predefined threshold, the optimization is considered converged. The variable *oldphi* is updated for the next iteration, and the ratio of the current volume to the initial volume is recalculated to ensure that the final design satisfies the volume constraint.

After confirming convergence, the optimization process is complete. The final material distribution represents an optimal solution that adheres to the exact volume constraint while maximizing the desired structural performance metric.

4. CONCLUSION

This research explored the exact volume constraint method for topology optimization, originally developed by Cui, Takahashi, and Matsumoto[1], through a detailed examination of its implementation in a FreeFEM++ script. The study focused on understanding and explaining the method, addressing the challenges of ensuring that optimized structural designs adhere to strict volume constraints while maximizing performance. The importance of this work lies in its role as an educational resource, bridging the gap between complex theoretical methods and their practical application, and providing clarity and accessibility for students and researchers new to the field.

By thoroughly analyzing the method and its implementation, the study contributes to making advanced optimization techniques more approachable, particularly for those in engineering fields like additive manufacturing and structural design. Although the method and script were originally developed and applied by others, this report enhances their understanding and effective use, offering a pathway for further exploration in more complex structures and refinement of computational techniques for greater efficiency and accuracy.

ACKNOWLEDGEMENTS

I would like to express my gratitude to Prof. Matsumoto for giving me this opportunity, to Asst. Prof. Cui for his guidance, and to Itoyama for his assistance.

REFERENCES

[1] Y. Cui, T. Takahashi, and T. Matsumoto, "An exact volume constraint method for topology optimization via reaction–diffusion equation," *Comput. Struct.*, vol. 280, p. 106986, May 2023, doi: 10.1016/j.compstruc.2023.106986.

[2] E. W. Weisstein, "Divergence Theorem." Accessed: Jul. 18, 2024. [Online]. Available: https://mathworld.wolfram.com/

[3] C. A. Manogue and T. Dray, *Product Rules*. Accessed: Jul. 18, 2024. [Online]. Available: https://books.physics.oregonstate.edu/GVC/rules.html

[4] P. Kelly, "Vectors_Tensors_12_HigherOrderTensors," in *Solid Mechanics Lecture Notes*, University of Auckland, 2013.

[5] D. Cheng, H. Qi (Ph.D.), and Y. Zhao, *An Introduction to Semi-tensor Product of Matrices and Its Applications*. World Scientific, 2012.

[6] M. P. Bendsøe and O. Sigmund, *Topology optimization: theory, methods, and applications*. Berlin ; New York: Springer, 2003.

[7] Y. Cui, T. Takahashi, and T. Matsumoto, "A time-saving FEM-based approach for structural topology optimization with exact boundary representation," *Mech. Eng. J.*, vol. 9, no. 6, pp. 22-00281-22–00281, 2022, doi: 10.1299/mej.22-00281.

[8] F. Hecht, "FreeFEM Documentation".

[9] C. G. Lopes, R. B. D. Santos, and A. A. Novotny, "Topological derivative-based topology optimization of structures subject to multiple load-cases," *Lat. Am. J. Solids Struct.*, vol. 12, no. 5, pp. 834–860, May 2015, doi: 10.1590/1679-78251252.

[10] A. A. Novotny and J. Sokołowski, *Topological Derivatives in Shape Optimization*. in Interaction of Mechanics and Mathematics. Berlin, Heidelberg: Springer Berlin Heidelberg, 2013. doi: 10.1007/978-3-642-35245-4.

[11] J. R. Barber, *Elasticity*, vol. 172. in Solid Mechanics and Its Applications, vol. 172. Dordrecht: Springer Netherlands, 2010. doi: 10.1007/978-90-481-3809-8.

[12] S. A. Nazarov, "Elasticity polarization tensor, surface enthalpy, and Eshelby theorem," *J. Math. Sci.*, vol. 159, no. 2, pp. 133–167, May 2009, doi: 10.1007/s10958-009-9432-0.

Comparative study of virgin and recycled CFRPs' characteristics

Mohamed Mokhtar Diop
Department of mechanical engineering, Polytechnique Montréal
mohamed-mokhtar.diop@polymtl.ca

Supervisor: Pr. YOSHIMURA Akinori
Graduate School of Engineering, Nagoya University
akinori.yoshimura@mae.nagoya-u.ac.jp

August 19, 2024

Abstract

The present paper intends, firstly, to show the steps that one can take to make carbon fibers reinforced polymer (CFRP) specimens. Secondly, it compares some mechanical properties of the virgin and recycled samples and quantify the degradation of the latter compared to the former when subjected to a tensile load. It focuses on characteristics like the Young's modulus, ultimate tensile strength and Poisson ratio. However, large variations have been observed among the results making then the comparison difficult. There are factors, some minor and others major, that had an impact on the final obtained results.

1 Introduction

Carbon fibers, a type of composite materials, are very well known for their high strength-weight ratio as well as tensile modulus-weight ratio, high fatigue strengths, high thermal conductivity and low coefficient of thermal expansion. However, they also feature weaknesses. Among them are their low strain-to-failure, low impact resistance and high cost [5]. They are getting more and more used in several industries. This production increase comes with a major drawback : Energy consumption and Pollution. Indeed, a big amount of energy is needed to manufacture carbon fiber. In addition to that, its waste is very polluting and dangerous for the environment. Recycling it cannot only keep the harm it provokes away but also allow industries that use composites the most to take advantage of it. They can replace some amount of virgin carbon fibers in their products by recycled ones, an efficient move for saving money. The reclaimed fibers from high-technology applications cannot be reused in the same applications from which they were recovered because of the drop-off in performance [7]. The objective of this study is to analyze those properties losses by conducting tensile tests.

2 Specimens fabrication process

In order to make comparisons, specimens have to be fabricated. To do so, we are obliged to go through the whole fabrication process. After a couple of unfruitful attempts, our team has been able to find the best manufacturing method.

2.1 Fibers cutting and arrangement

2.1.1 Virgin Carbon Fiber (vCFRP)

For the purpose of this study, the high-performance medium-elasticity fibers **T800SC-24K** are utilized. It is mainly found in the aerospace industry for now but its use will be expanded into other fields in the future. It has a Young Modulus of **294 GPa**, a tenisle strength of **5880 MPa** and a breaking elongation of **2%** [2].

Virgin carbon fibers (**275 mm** long) are cut and laid out next to each other to obtain 4 layers. The tows consist of 24000 filaments of 5 µm each and are placed in a way to get a width of **100 mm** for each ply, that means the number of tows could vary from one layer to another.

Figure 1: Virgin Fibers T800SC-24K

2.1.2 Recycled Carbon Fiber (rCFRP)

This recycled fiber has been obtained from the **T800S** used to make the B787 aircraft which has the same tensile strength and modulus as the the T800SC-24K [1]. The recycling process has been carried out by Carbon Fiber Recycle Industry co.ltd. by thermally decomposing the matrix before reclaiming the fibers. It is to be noted that there is an inevitable drop-off in performance undergone by the recycled fibers that we will quantify later on in this report.

Figure 2: Carbon fiber usage process

Unlike the vCFRP, the recycled carbon fibers arrived at the laboratory already arranged in tows of **1.3 m** long and **210 mm** wide. The number of filaments comprising each tow is only known by the company that reclaimed them.

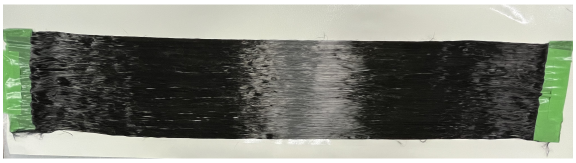

Figure 3: Recycled carbon fibers T800S

Figure 4: Epoxy resin film

2.2 Resin application

Only one type of resin is used in the context of this project, it is a mixture of two resins made by Mitsubishi Chemical Corporation: the **jER828** and the **jER1001** with a 4:6 mixing ratio.

Two epoxy resin films are applied over the front and back sides of each carbon fibers layer which account to a total of 8 small films for the vCFRP and 2 large films for the rCFRP. By applying a little bit of tension to straighten the fibers and remove the gaps between them, using an iron and applying it with a low pressure in the direction of the fibers, the resin is then liquefied and the fibers impregnated.

Figure 5: Ironing technique

In the case of the rCFRP since the fibers are too long, the whole partially cured resin and impregnated fibers that is called **prepreg** is cut in 4 small layers of **275 mm** long and **100 mm** wide to match the dimensions of the vCFRP product. The latter are then stacked up by making use once again of the ironing technique. This action allows the bonding of the layers.

and films

Figure 6: Stacking of the layers

2.3 Curing process

The step that ensues is the curing process thanks to an autoclave whose main advantage is the ability to control the pressure. But before starting the hardening step, the prepreg has to be vacuum-bagged until the pressure reaches **-0.1 MPa** in order to impregnate the fibers even more and remove as many voids as possible. These little empty spaces in the product can compromise its strength and durability. The curing pressure is then set at **0.3 MPa** for the virgin carbon fiber prepreg. But the volume of fiber being bigger for the rCFRP, a higher pressure is needed compared to the vCFRP to get a better fiber impregnation even it is dangerous. In this case, it is **0.5 MPa**.

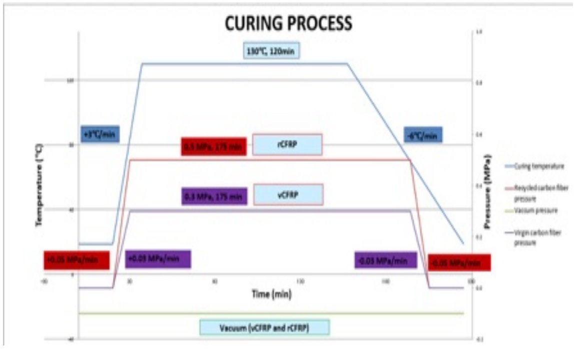

Figure 7: The autoclave setting during the curing process

2.4 Final products

Two different laminates are obtained at the end of the curing process. The principal difference between them is the volume fraction which is defined as its name suggests as, the volume of fibers in an entire composite product. It is given by the following formula:

$$\mathbf{v_f} = \frac{\rho_\mathbf{m}\mathbf{w_f}}{\rho_\mathbf{f} - (\rho_\mathbf{f} - \rho_\mathbf{m})\mathbf{w_f}} \tag{1}$$

Where:
w_f corresponds to the weight fraction of the fibers and is calculated via this equation:

$$\mathbf{w_f} = \frac{\mathbf{W_f} - \rho_\mathbf{A}\mathbf{A_{resin}} * \mathbf{number - of - layers}}{\mathbf{W_f}} \tag{2}$$

and
W_f represents the weight in grams of the carbon fibers in the product;
ρ_f and ρ_m respectively are the fibers and resin or matrix densities. Their values are given by this following table 1 :

Table 1: Carbon fiber and resin density

	Density (g/cm^3)
Fiber	1.8
Resin	1.2

One approximation is made here: we consider the density of the virgin and recycled carbon fibers to be the same. This can impact the results we get later on.

2.4.1 Virgin Carbon Fiber (vCFRP)

This laminate comprised of 4 layers of vCFRP and 8 epoxy resin films exactly weighs **36.59 g**. Therefore,

$$\mathbf{w_f} = \frac{\mathbf{36.59 - 48.5 * 0.285 * 0.120 * 8}}{\mathbf{36.59}} \tag{3}$$
$$\Longrightarrow \mathbf{w_f} = 63.73\%$$

and

$$\mathbf{v_f} = \frac{\mathbf{1.2 * 0.6373}}{\mathbf{1.8 - (1.8 - 1.2) * 0.6373}} \tag{4}$$
$$\Longrightarrow \mathbf{v_f} = 53,95\%$$

2.4.2 Recycled Carbon Fiber (rCFRP)

This laminate which is also made of 4 layers of rCFRP and 8 epoxy resin films exactly weighs **46.95 g**. Thus,

$$\begin{aligned} \mathbf{w_f} &= \frac{\mathbf{46.95 - 48.5 * 0.275 * 0.105 * 8}}{\mathbf{46.95}} \\ \Longrightarrow \mathbf{w_f} &= \mathbf{76.14\%} \end{aligned} \tag{5}$$

and

$$\begin{aligned} \mathbf{v_f} &= \frac{\mathbf{1.2 * 0.7614}}{\mathbf{1.8 - (1.8 - 1.2) * 0.7614}} \\ \Longrightarrow \mathbf{v_f} &= \mathbf{68, 02\%} \end{aligned} \tag{6}$$

2.4.3 Conclusion

Both products are in concordance with the general rule about the composites stating that the volume fraction of a product must be around 50 to 60 % and can thus be used to conduct tensile tests.

2.5 Cutting of the specimens

The two CFRP products are cut into a number of specimens using the a manual and automatic cutting machines by taking into account the ATSM standards and recommendations. Certain dimensions have to be respected depending on the test which is performed. For a tensile test, it is recommended to have specimens which are **250 mm** long and **15 mm** wide as shown by the table 2.

The ASTM D3039 specimens are rectangular in shape with a constant cross-section[6]. Given that the prepregs were made of unidirectional carbon fibers oriented at 0°, the appropriate coupon length to conduct a tensile test is **250 mm** as shown on the table. However on the recommendation of the professor, it has been decided to pursue with samples that have a width of **12.5 mm** instead of 15 mm in order to maximize their number. As far as the thickness is concerned, it varies depending on the position the specimen is cut from. Put simply, the edges of both hand-made CFRP products are very thin and cannot be used to perform tests; that's why only its central part is exploited. A thickness considered reasonable can go from **0.7 to 1.2 mm**.

3 Tensile testing

During a tensile test, a sample is subjected to a tension until it breaks. It generally undergoes a elastic then plastic deformation before failing. But in the of carbon fibers' case there is no plastic deformation, the elastic one is directly ensued by a fracture signaling that the specimen is broken.

The test is performed through a universal testing machine (**Shimadzu AUTOGRAPH AG-X plus 100 kN**) fabricated by Shimadzu and is able to reach 100 kN as the model name suggests. The testing speed is the one set by default, that is **1 mm/min**.

According to the ASTM D3039, 5 specimens per test are required [8] but the data of one of the initial test's samples were lost so, it has been decided that the following test will be carried out with 4 specimens.

Figure 8: Tensile Testing set-up

3.1 Gripping area

According to the recommendations for any polymer matrix composite specimen, the length of each of the two gripping areas must be tantamount to 20% of the total length of the sample, that is **50 mm** in our case. It is

Table 2: Tensile specimens geometry recommendations [8]

Fiber orientation	Width,mm	Overall Length, mm	Thickness, mm	Tab Length, mm
0° unidirectional	15	250	1.0	56
90° unidirectional	25	175	2.0	25
balanced and symmetric	25	250	2.5	emery cloth
random-discontinuous	25	250	2.5	emery cloth

very common for users to utilize tabs in composites testings in order to decrease the stress concentration around the grips. But these specimens being comprised of unidirectional fibers, an emery cloth must be used instead. It prevents the specimens from slipping while the load is applied by increasing the friction between them and the grips.

Figure 9: Gripping area

3.2 Strain gauges

A strain gauge is a transducer measuring loads and elongations an object is subject to by using the properties of electrical conductance. In other words, it transforms physical loads into a readable electrical signal recorded by a data logger (see figure 11). There are several types of strain gauges but only the bi-axial one is used within the scope of this project because it allows us to get the Poisson ratio for each coupon.

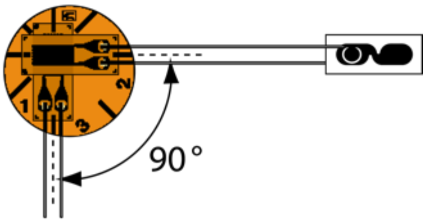

Figure 10: Bi-axial 0°/90° strain gauge

The model used is named **KFGS-1-120-D16-11 L1M2S**. It is **1 mm** long and has a resistance of **120.4** Ω.

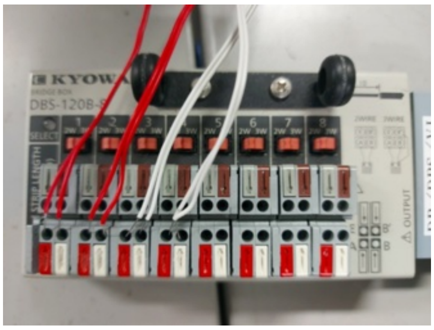

Figure 11: Data logger

Looking at the figure 10, it is possible to notice that four wires compose it: two in one direction and the other two are positioned at an 90° angle from the first ones.

On a specimen, a setof two wires (Whichever it is) is positioned in a way that they are parallel to the fibers. It allows to get the deformation in the direction of the fibers (0°) and in the transversal direction (90°).

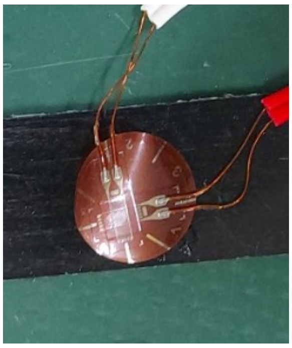

Figure 12: A strain gauge set on a specimen

3.3 Observations

The specimens are broken along their longitudinal axis that is, the fibers separate themselves from each other (see figure 13). This kind of failure mode is called **"Splitting"**.

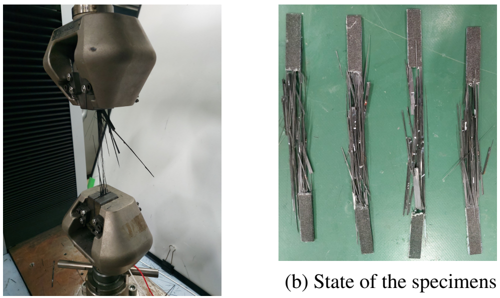

(a) Splitting of the fibers

(b) State of the specimens after the tensile test

Figure 13: Tensile test results

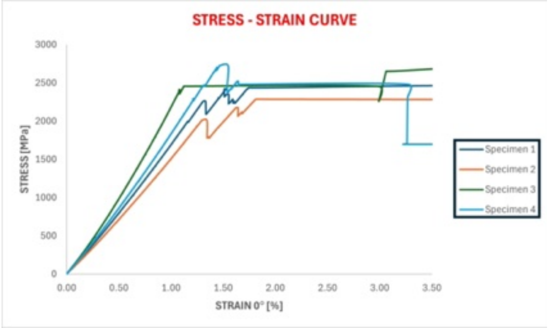

(a) Stress-strain curve for the vCFRP

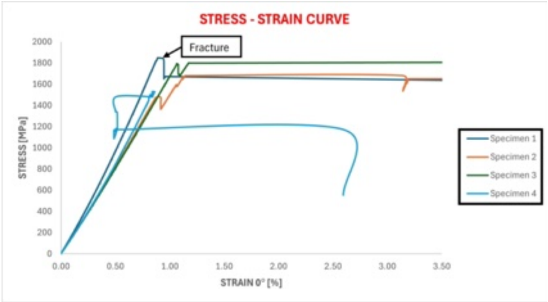

(b) Stress-strain curve for the rCFRP

Figure 14: Tensile test results

3.4 Coefficient of variation

The coefficient of variation (CV) is the ratio of the standard deviation to the mean. As to the former, it is defined a measure of the amount of variation of a random variable expected about its mean value. The following formulas enable to express them [8]:

$$\mathbf{\bar{x} = \frac{\sum_{i=1}^{n} x_i}{n}}$$

$$\mathbf{s_{n-1} = \sqrt{\frac{\sum_{i=1}^{n} x_i^2 - n\bar{x}^2}{n-1}}} \tag{7}$$

$$\mathbf{CV = 100 * \frac{s_{n-1}}{\bar{x}}}$$

where:
$\bar{x}$ = sample mean (average);
$s_{n\ 1}$ = sample standard deviation;
CV = sample coefficient of variation, in percent;

n = number of specimens; and
x_i = measured or derived property.

The coefficient of variation (CV) must be inferior to 5% for the results to be considered good.

3.5 Ultimate tensile strength

The ultimate tensile strength is the maximum stress that a material can withstand while being stretched or pulled before breaking. It is expressed through the below formula :

$$\mathbf{F^{tu}} = \frac{\mathbf{P^{max}}}{\mathbf{A}} \tag{8}$$

where:
F^{tu} = ultimate tensile strength, MPa;
P^{max} = maximum load before failure, N;
A = average cross-sectional area, mm^2

Table 3: Ultimate tensile strength

	vCFRP, MPa	rCFRP, MPa
Specimen 1	2434.89	1849.29
Specimen 2	2286.62	1680.67
Specimen 3	2651.31	1801.27
Specimen 4	2481.25	1499.74
Average value	**2463.51**	**1707.74**
s_{n-1}	**150.22**	**155.76**
CV	**6.10%**	**9.12%**

The coefficients of variation are superior to 5% which means that the results are not good enough.

3.6 Young modulus

The Young modulus can be defined as a mechanical property that measures the tensile or compressive **stiffness** of a material when a force is applied lengthwise. Its formula is the following:

$$\mathbf{E} = \frac{\Delta\sigma}{\Delta\epsilon} \tag{9}$$

where:
E = tensile chord modulus of elasticity, GPa;
Δσ= difference in applied tensile stress between the two strain points (0.1 and 0.3 %), MPa; and
Δε= difference between the two strain (nominally 0.002).

Table 4: Young's modulus

	vCFRP, MPa	rCFRP, MPa
Specimen 1	188.32	156.19
Specimen 2	162.01	140.40
Specimen 3	159.38	191.00
Specimen 4	164.38	170.91
Average	**168.52**	**164.62**
s_{n-1}	**21.55**	**13.36**
CV	**13.09%**	**7.93%**

The coefficients of variation are superior to 5% which means that the results are not that acceptable.

3.7 Poisson ratio

The Poisson's ratio is the ratio between a material's lateral and longitudinal strain when it is stretched. It is given by the following equation :

$$\nu = -\frac{\Delta\epsilon_t}{\Delta\epsilon_l} \tag{10}$$

where:
ν= Poisson's ratio;
$\Delta\varepsilon_t$ = difference in lateral strain between the two longitudinal strain points (0.1 and 0.3 %) ; and
$\Delta\varepsilon_l$ = difference between the two longitudinal strain points (0.1 and 0.3 %).

Table 5: Poisson ratio

	vCFRP, -	rCFRP, -
Specimen 1	0.41	0.33
Specimen 2	0.37	0.41
Specimen 3	0.36	0.42
Specimen 4	0.37	0.46
Average	**0.38**	**0.41**
s_{n-1}	**0.020**	**0.056**
CV	**5.30%**	**13.77 %**

The coefficient of variation for the vCFRP is equal to 5% which means that the result is acceptable even if the values of the Poisson ratio are too big. However, the same can't be said about the rCFRP's coefficient of variation.

4 Causes of the differences among the results

As shown by the tables 3, 4 and 5, there is a large variation between the tensile strengths, Young Modulus and Poisson ratios of the specimens containing the same type of fibers regardless of the conducted test.

Many factors can be the reasons of such diversified results [8]:

- Methods of material preparation and lay-up,
- Specimens stacking sequence,
- Testing environment,
- Specimens alignment and gripping,
- Speed of testing,
- Void content...

Beside these aforementioned factors, other elements are able to have a large impact on the final numbers. Among them, there are:

4.1 Quality of the specimens

The samples being handmade, it is evident their quality leave a lot to be desired. Even though the same techniques are used to make the virgin and recycled prepregs, small differences can occur due to human error like for instance the tows positioning, iron temperature ....

4.2 Volume of fibers

The difference of volume fraction amongst the specimens made from the same kind of fiber can partly explain the large variation observed when they are subject to tensile loads.

4.3 Waviness

Waviness is a common defect characterized by local misalignment of straight fibers, resulting in a deviation from the initial intended direction [3]. Avoiding these waving patterns is extremely difficult or even impossible. Their presence, size, shape and location affect drastically the mechanical performances of a product. They are also responsible for initiating the failures in composites and reducing their stiffness, that is their Young modulus. Even the Poisson ratio can undergo changes because of that [4].

(a) Longitudinal waviness

(b) Transversal waviness

Figure 15: Virgin and recycled CF prepregs

4.4 Strain gauges misalignment

One major problem of using a strain gauge when doing a tensile test is its misplacement. This phenomenon can result in the distortion of the results as it can be seen on figure 14. The differences between the Young modulus are a proof that the strain gauges are not positioned where they should be.

5 Adjustments of the tensile strength and Young modulus

Given the volume fraction difference between the specimens used to conduct the two tensile tests, their results cannot be really compared as they are. To make a proper comparison, we must estimate the ultimate tensile strength and Young modulus of the virgin carbon fiber at a 68% volume of fiber.

5.1 Ultimate tensile strength

The following formula allows to calculate the ultimate tensile strength of a product:

$$\sigma_\mathbf{c} = \sigma_\mathbf{f}\mathbf{v_f} + \sigma_\mathbf{m}(\mathbf{1} - \mathbf{v_f}) \tag{11}$$

Here:
σ_c = Ultimate tensile strength of an entire specimen;
σ_f = Ultimate tensile strength of the fibers comprising a specimen;
σ_m =Ultimate tensile strength of the matrix or resin which composes a specimen; and
v_f = Fraction volume or volume of fiber.

The exact strength of the resin is difficultly knowable. The calculations will be made under the assumption that it's equal to zero because it's effect is so small compared to that of the fibers. Knowing that:

$$\sigma_\mathbf{c} = \sigma_\mathbf{f}\mathbf{v_f} \tag{12}$$

The ultimate strength of the fibers is then computable:

$$\begin{aligned} \sigma_\mathbf{c} &= \sigma_\mathbf{f}\mathbf{v_f} \\ \Longrightarrow \sigma_\mathbf{f} &= \frac{\mathbf{2463.5}}{\mathbf{0.54}} = \mathbf{4562.04} \quad \mathbf{MPa} \end{aligned} \tag{13}$$

This enables us to estimate the exact value the ultimate tensile strength we would have gotten had the volume of fiber of the virgin specimens been 68%.

$$\begin{aligned} \sigma_{\mathbf{68\%}}(\mathbf{vCFRP}) &= \sigma_\mathbf{f}\mathbf{v_f} \\ \Longrightarrow \sigma_{\mathbf{68\%}}(\mathbf{vCFRP}) &= \mathbf{4562.04} * \mathbf{0.68} \\ \Longrightarrow \sigma_{\mathbf{68\%}}(\mathbf{vCFRP}) &= \mathbf{3102.19} \quad \mathbf{MPa} \end{aligned} \tag{14}$$

5.2 Young modulus

The following formula allows to compute the Young modulus of a product:

$$\mathbf{E_c} = \mathbf{E_f}\mathbf{v_f} + \mathbf{E_m}(\mathbf{1} - \mathbf{v_f}) \tag{15}$$

Here:
E_c = Young's Modulus of an entire specimen;
E_f = Young's Modulus of the fibers comprising a specimen;
E_m = Young's Modulus of the matrix or resin which composes a specimen; and
v_f = Fraction volume or volume of fiber.

It's an equation with two unknowns because neither of E_f and E_m are known. But according to the data facilitated by Toray, the modulus of the fibers E_f equates to 298 GPa [1]. With the latter, the modulus of elasticity of the epoxy resin becomes calculable:

$$\begin{aligned} \mathbf{E_m} &= \frac{\mathbf{E_c} - \mathbf{E_f}\mathbf{v_f}}{\mathbf{1} - \mathbf{v_f}} \\ \Longrightarrow \mathbf{E_m} &= \frac{\mathbf{164.8} - \mathbf{294} * \mathbf{0.54}}{\mathbf{1} - \mathbf{0.54}} = \mathbf{13} \quad \mathbf{GPa}. \end{aligned} \tag{16}$$

This enables us to estimate the modulus we would have gotten if the volume of fiber of the virgin specimens was 68%.

$$\begin{aligned} \mathbf{E_{68\%}}(\mathbf{vCFRP}) &= \mathbf{E_f}\mathbf{v_f} + \mathbf{E_m}(1 - v_f) \\ \Longrightarrow \mathbf{E_{68\%}}(\mathbf{vCFRP}) &= \mathbf{294} * \mathbf{0.68} + \mathbf{13} * \mathbf{0.32} \\ \Longrightarrow \mathbf{E_{68\%}}(\mathbf{vCFRP}) &= \mathbf{204.08} \quad \mathbf{GPa} \end{aligned} \tag{17}$$

Table 6: The calculation of the degradation

	vCFRP	rCFRP	Drop-off
σ_c	3102.16	1707.70	**45.96%**
E	204.08	168.50	**17.5%**

The above table 6 shows that there is a degradation of the quality of specimens. The recycled samples have an ultimate tensile strength and a Young modulus that are respectively about 46% and 18% less than the virgin ones. These numbers are in accordance with what has been found on the market: it has been proven that the Young modulus degradation , which is about 20%, is smaller than the ultimate strength one.

Moreover, it is possible to calculate the Young modulus of the recycled fiber alone by making use of the result of equation 16.

$$\mathbf{E_f} = \frac{\mathbf{E} - \mathbf{E_m}(\mathbf{1} - \mathbf{v_f})}{\mathbf{v_f}}$$
$$\implies \mathbf{E_f} = \frac{\mathbf{168.5} - \mathbf{13} * (\mathbf{1} - \mathbf{0.68})}{\mathbf{0.68}} \tag{18}$$
$$\implies \mathbf{E_f} = \mathbf{241.7} \quad \mathbf{GPa}$$

Knowing that the virgin carbon fiber's Young modulus is 294 GPa according to Toray, it is possible to say throughout the recycling process, the carbon fiber lost **17.8 %** of its Young modulus.

6 Conclusion

By way of conclusion, we can state that the recycled carbon fiber is still a very strong material. However, there is significant degradation of its properties compared to the virgin carbon fiber. The drop-off is estimated to be about 20% for the Young Modulus and 45% for the ultimate strength.

The quality of the specimens has probably played a major role in the results. In addition to that the volume of fiber, waviness and the strain gauges misalignment have also contributed to the large obtained variation.

Not being part of the scope of this research, one may further investigate about the degradation of the recycled carbon fibers when used in high and low temperature environments.

Acknowledgements

This work would not have been possible without the help of my advisor Pr. YOSHIMURA Akinori, his assistant Pr. ICHIKI Makoto and all the students of Advanced Composites laboratory. I would also like to acknowledge all the efforts of the JUACEP office and thank them for this big opportunity.

References

[1] Carbon fiber. https://www.toraycma.com/products/carbon-fiber/. Accessed: 2024-07-31.

[2] Torayca t800sc medium elastic carbon roving 24k 10e 1m-5m-20m. https://www.sano-factory.jp/item/117/. Accessed: 2024-07-31.

[3] MP Alves, CA Cimini Junior, and Sung Kyu Ha. Fiber waviness and its effect on the mechanical performance of fiber reinforced polymer composites: An enhanced review. *Composites Part A: Applied Science and Manufacturing*, 149:106526, 2021.

[4] Pritam Kulkarni, Kiran D Mali, and Sandeep Singh. An overview of the formation of fibre waviness and its effect on the mechanical performance of fibre reinforced polymer composites. *Composites Part A: Applied Science and Manufacturing*, 137:106013, 2020.

[5] Pankar K Mallick. *Fiber-reinforced composites: materials, manufacturing, and design*. CRC press, 2007.

[6] Ian McEnteggart. How to perform a tensile test on composite materials to astm d3039. https://www.instron.com/en/testing-solutions/astm-standards/astm-d3039. Accessed: 2024-07-29.

[7] Géraldine Oliveux, Luke O Dandy, and Gary A Leeke. Current status of recycling of fibre reinforced polymers: Review of technologies, reuse and resulting properties. *Progress in materials science*, 72:61–99, 2015.

[8] ASTM Committee D-30 on Composite Materials. *Standard test method for tensile properties of polymer matrix composite materials*. ASTM international, 2008.

THRUST CHARACTERISTICS OF DIVERGING MAGNETIC FIELD THRUSTERS

Edith Shear

College of Engineering - Aerospace Engineering, Rackham Graduate School, University of Michigan
emshear@umich.edu

Ryota Nakano, Kiyoshi Kinefuchi

Graduate School of Engineering, Nagoya University
Kiyoshi.kinefuchi@mae.nagoya-u.ac.jp

ABSTRACT

Measuring accurate thrust in electric propulsion is critically important for proper characterization. Thrust characteristics through diverging magnetic field thrusters via propellant injection from a central cathode exhibit difficulties when characterizing accurate measurements due to the small scale of thrust produced. This combined with magnetic field interferences with the geomagnetic field and other currents present in experimental setups creates difficulties in accurate measurements. By following procedures of calibration and using measurements from a pendulum stand, measurements were collected and analyzed with proper tare adjustments to account for these external magnetic forces. Thrust was analyzed through a series of tests varying discharge voltage and ejection mass flow rate. It was observed that through proper calibration techniques and calculation of tare forces, results followed trends that agreed with the known physical properties of electric propulsion thrusters.

1. NOMENCLATURE

Variables

I = *moment of inertia*

c = *damping constant*

θ = *angular position*

$F(t)$ = *applied force*

L = *length of pendulum arm*

k = *effective spring constant*

F_{tare} = *Tareforce*

J_d = *discharge current*

J_k = *keeper current*

J_c = *coil current*

F = *Thrust*

$\dot{m}$ = *total mass flowrate between anode and cathode*

V_e = *velocity*

V_{e_q} = *equivalent velocity*

p = *pressure*

A_e = *Area*

I = *total impulse*

g_0 = *gravitational constant*

Isp = *specific impulse*

e = *charge*

Pt = *total power between anode and cathode*

$E(-)$ = *error*

m_i = *ion mass*

η = *thrust efficiency*

2. INTRODUCTION

Efficient payload use is crucial for mission success and the duration of long-distance and extended operations. As missions expand further and further out a higher demand for better usage of payloads to support and sustain these missions grows in demand. This implies larger space missions are now requiring higher and higher specific impulses, which is the efficiency with which propellant is used and turned into thrust, in order to succeed. A thruster with higher specific impulse requires less overall propellant to be carried, which increases the efficiency of propellant usage. As a result, missions can allocate more payload to necessary supplies for sustaining long-term missions, creating more cost-effective space mission possibilities in a costly and growing industry.

Electric propulsion has gained popularity due to demonstrated higher efficiency in propellant utilization and greater specific impulses. This leads to a reduced propellant requirement, enabling a greater allocation of payloads compared to traditional chemical propellants. Specific impulse for electric propulsion is not potentially limited like that in chemical-based propellants. While chemical propellants are naturally constrained to the energy in chemical reactions themselves, electric propulsion does not rely on the propellant's chemical energy to efficiently ionize and accelerate particles. This opens the door to further optimizations and enhances the efficiency of electric propulsion thrusters beyond the capabilities of chemical propellants.

Accurate thrust measurements are essential for precise characterization of specific impulse (Isp) of thrusters, which ultimately contributes to improved optimization and design of thrusters, resulting in increased payload efficiency. Overall accurate thrust measurements provide a crucial role in characterizing thrusters. At the same time, one of the largest challenges of electric propulsion is the accuracy of measurements when experimentally testing as thrusters produce small levels ranging μN to mN levels of thrust rendering conventional thrust measurement methods ineffective. Currently, large amounts of effort are being put into properly developing practices and equipment to mitigate error. The AIAA currently is leading this initiative in setting a generalized standard for ensuring accurate testing. [1] This includes producing proper procedures for the usage of pendulum thrust stands along with calibration techniques.

Concerning electric propulsion, there are several types of thrusters available, most famously known among them are Hall and MPD thrusters. Electric propulsion is categorized into three main sections: electrostatic, electromagnetic, and electrothermal. [2] Electrostatic-magnetic hybrid thrusters with diverging magnetic fields, the focus of this study, combine the characteristics and advantages of both electromagnetic and electrostatic thrusters. With hybrid acceleration, thrust density is increased beyond what can be achieved with electrostatic acceleration alone. At the same time, thrust efficiency is also higher compared to electromagnetic acceleration alone. Considering the novelty of hybrid thrusters in comparison to more established forms of electronic propulsion, there is still ample room for investigation.[3] Nonetheless, qualifying accurate thrust measurements is a sound first step to characterizing these thrusters.

3. GOVERNING EQUATIONS

3.1 Pendulum thrust stand

Since electric propulsion exhibits a low thrust-to-mass ratio typical load cells that measure thrust directly cannot accurately be used. [1,4] A pendulum thrust stand is noted by the AIAA as the most accurate form of thrust measurement for electric propulsion. As such it is used for experimentation of collecting accurate thrust data.

Hanging pendulums exhibit the following dynamics of motion.

$$\boldsymbol{I\ddot{\theta} + c\dot{\theta} + k\theta = F_{(t)}L} \tag{1}$$

I is the moment of inertia while $\boldsymbol{\theta}$ denotes the angular position, c and k are damping constant and the spring constant respectively. F(t) is the applied force the pendulum experiences while L is the length of the pendulum arm.

3.2 Tareforce

Tareforce is categorized as interactional forces that occur within the setup that need to be mitigated in final thrust measurements to properly measure accurate thrust. [5] Tarefroce occurs in the interactions between different currents in the thruster stand wiring supplies, when activated several interactions occur. Notable interactions are accounted for through the following equation:

$$F_{tare} = C_1'J_cJ_d + C_2'J_kJ_d + C_3'J_d^2 \tag{2}$$

Discharge current J_d interacts with coil current J_c keeper current J_k discharge current J_d, generating extra force on the system. Since coil current and keeper current were kept at a constant the equation simplifies to:

$$F_{tare} = C_1J_d + C_3J_d^2 \tag{3}$$

3.3 Isp, Thrust Efficiency, and Error analysis

Specific impulse is characterized as the efficiency of thrust produced per unit of propellant flow rate. To calculate specific impulse, we first need to consider the generalized rocket thrust equation [6], which is given as follows:

$$F = \dot{m}V_e + (p_e - p_0)A_e \tag{4}$$

Equivalent Velocity is then defined as the following:

$$V_{eq} = V_e + \frac{(p_e - p_0)Ae}{\dot{m}} \tag{5}$$

$$F = \dot{m}V_{e_q} \tag{6}$$

It is essential to note that the total mass flow rate for the system is divided between the flow rates at the anode and cathode orifices within the thruster.

From this, the total impulse is described as the following:

$$I = F\Delta t = \int \dot{m}V_{eq}\,dt \tag{7}$$

Specific impulse is then:

$$I_{sp} = \frac{V_{eq}}{g_0} = \frac{F}{\dot{m}g_0} \tag{8}$$

Thrust efficiency, the ratio of effective thrust energy to the input energy, is defined as the following equation:

$$\eta = \frac{F^2}{2\dot{m}\,P_t} \tag{9}$$

Error calculations are made using error propagation rules for both thrust efficiency and Isp in equations 10 and 11 respectively.

$$E(\eta) = \eta \sqrt{2\left(\frac{E(F)}{F}\right)^2 + \left(\frac{E(\dot{m})}{\dot{m}}\right)^2 + \left(\frac{E(P_t)}{P_t}\right)^2} \quad (10)$$

$$E(I_{sp}) = I_{Sp}\sqrt{\left(\frac{E(F)}{F}\right)^2 + \left(\frac{E(\dot{m})}{\dot{m}}\right)^2} \quad (11)$$

4. EXPERIMENTAL SETTINGS

4.1 Vacuum Facility

All testing was contained within a 4 m long by 2 m high stainless steel vacuum chamber (Fig. 1). The thruster is held on a hanging pendulum thrust stand. Feed through wiring also extends down through the hanging pendulum thrust stand [7]. The hanging pendulum stand consists of a 1.1 m long aluminium arm that reaches outside the chamber and is connected to an oil damper and linear variable differential transformer (LVDT) LVDT1301-2; Shinko Electric Co., Ltd. The LVDT signal is used to determine the thrust force created by the thruster and is calibrated via a load force using a motor-actuator basket to load and unload various masses on a string pulley system that is connected to the thrust stand and anchored to the bottom of the vacuum chamber. Outside, the vacuum chamber is evacuated using two turbomolecular pumps, 3203LMC and XZ4304LM; Shimadzu Corporation, which operate at exhaust speeds of 3200 L/s and 4050 L/s, backed by a rotary pump, VD90C; ULVAC Technologies, Inc., with an exhaust speed of 30 L/s.

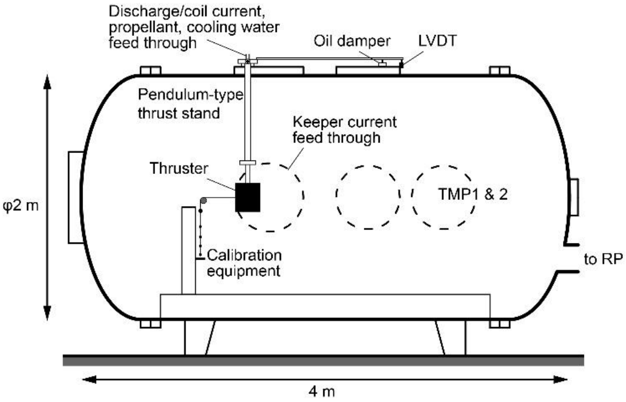

Fig. 1 Schematic of vacuum facility

4.2 Thruster and thrust stand

The thruster (Fig. 2) is comprised of a hollow cathode on a central axis and a ring-shaped anode with a nominal inner radius of 40mm. Propellant flow is injected through the hollow cathode of 2 mm diameter and a 1.5 mm width slit between the anode inner surface and the ceramic cylinder outer surface. A copper (C1020) SR with an axial thickness of 5 mm is at the anode tip. [8]

An external magnetic field is created within the thruster from the water-cooled solenoid coil. Proper connections are made both to the cathode and anode for keeper and discharge lines. Xenon (99.999% purity) is utilized for the thruster and is introduced using a mass flow controller (Model 3660; KOFLOC Co., Ltd.) to regulate the mass flow at the anode and cathode. Uncertainty for each mass controller is ±0.03 mg/s. A HX01000; TAKASAGO Ltd. is used to supply power for the discharge between the anode and cathode. For the hollow cathode keeper and the solenoid coil, KC8002; Kaufman & Robinson, Inc., and N8761A; Agilent Technologies, Inc. are used. [9]

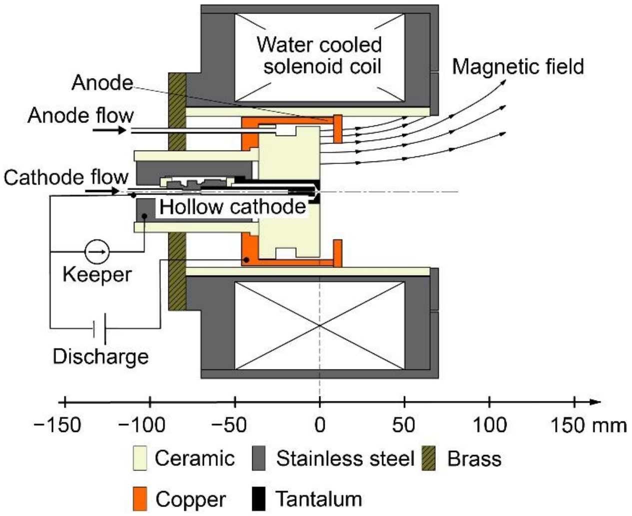

Fig. 2 Schematic of the thruster

4.3 Testing procedures

To start testing, the facility vacuum chamber was evacuated using two turbomolecular pumps (3203LMC and XZ4304LM; Shimadzu Corporation) with exhaust speeds of 3200 L/s (N2) and 4050 L/s (N2), backed by a rotary pump (VD90C; ULVAC Technologies, Inc.) with an exhaust speed of 30 L/s (N2) as prior mentioned. The rotary pump is used to draw a vacuum to less than 200 Pa. for about 45 min. Argon flows at a mass flow rate of 5 sccm to “clean out” tubing while evacuation of the chamber is happening. The two turbomolecular pumps are then used to draw vacuum to less than 5 mPa, which takes about 2 hours. The working gas (xenon) then flows at 100 sccm to properly ‘load’ the flowlines between mass flow meters with working gas. The keeper supply is then turned on and kept at a constant keeper current of 2 A and a gradual reduction in the working gas flow rate is made to the specified tested values.

Table 1. Operating Conditions

Operating conditions	**Symbol**	**Unit**	**Value**
Propellant species	-	-	xenon
Keeper current	J_k	A	2.0
Magnetic field strength (at cathode tip)		T	0.15
Cathode flow rate	$\dot{m}_c$	mg/s	0.49
		Aeq	0.36
Anode flow rate	$\dot{m}_a$	mg/s	1.4, 2.1, 2.7
		Aeq	1.0, 1.5, 2.0
Total flow rate	$\dot{m}_t = \dot{m}_c + \dot{m}_a$	mg/s	1.9, 2.5, 3.2
		Aeq	1.4, 1.9, 2.4
Discharge voltage	V_d	V	100–300

Table 2. Measurement Parameters

Measurement Parameters	**Symbol**	**Unit**	**Value**
Keeper voltage	V_k	V	11–14
Discharge current	J_d	A	7–18
Back pressure	-	mPa	10–20
Thrust	F	mN	19–54

To initiate the discharge of the thruster, propellant flow is supplied to the anode. The solenoid coil power is then activated to apply the magnetic field, and subsequently, the main power discharges the thruster.

Table 1 refers to operating conditions of propellant species, keeper current, magnetic field strength, flow rates for both the anode and cathode injection sites, and discharge voltage. To follow up in Table 2, measurement parameters are defined for the system.

5. RESULTS AND DISCUSSION

Tables 1 and 2 display the thruster operating conditions and the measurement parameters, respectively. Testing with xenon propellant was conducted at mass flowrate of 14, 21, and 28 sccm. Mass flow rate at the cathode was kept at a constant 5 sccm throughout all testing. Discharge voltage was tested at varying intervals, 100-300 V so that the discharge current did not exceed the hollow cathode specification.

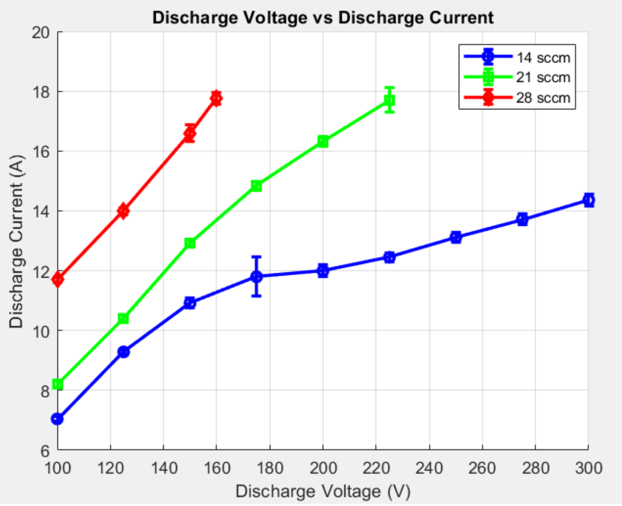

Fig. 3 Discharge Voltage vs Discharge Current of Xenon

In Fig. 3, it is demonstrated that an increase in discharge voltage leads to a corresponding increase in discharge current, in accordance with Ohm's law. Furthermore, the data indicates that elevating propellant flow rates results in higher discharge current. This observation can be attributed to the heightened ion density and ionization within the thruster, thereby causing a greater flow of current through the system. Increases in both flow rates and discharge voltages led to an amplified overall thrust, as depicted in Fig. 4.

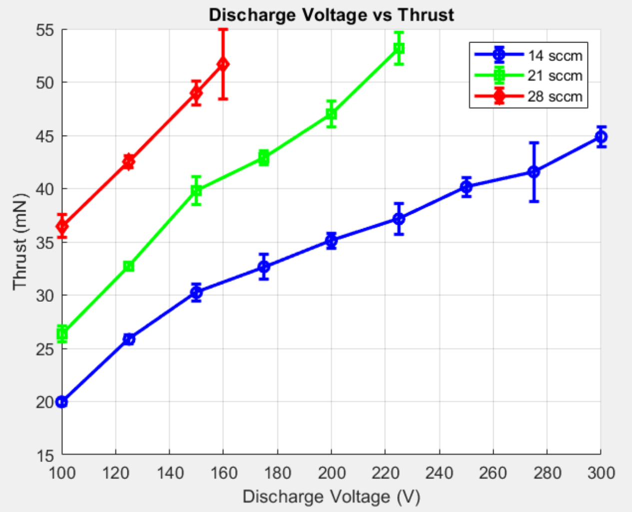

Fig. 4 Discharge Voltage vs Thrust of Xenon Propellant

At lower discharge voltages, ion acceleration is seen to be less effective in thrusters than at higher discharge voltages. Although higher propellant flow rates initially resulted in higher impulse as demonstrated in Fig. 5, this decreased over increased discharge voltages due to this ion acceleration inefficiency.

With an increase in discharge voltage, a higher specific impulse was achieved. Change in specific impulse due to variations in propellant flow rate falls within the margin of error, indicating that no significant difference is apparent, as demonstrated through Fig. 6. Lower flow rates demonstrated higher specific impulse rates at increasing discharge voltages, which signaled more efficient power distribution as discharge voltage increased. Thrust efficiency decreased at higher discharge voltages across all flow rates. This decrease can be attributed to the increase in losses within the system due to higher discharge voltages, which in turn require more current, reducing overall efficiency of the thruster.

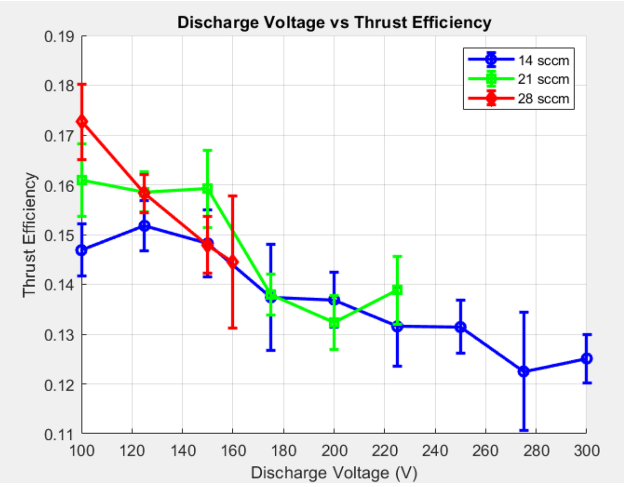

Fig. 5 Discharge Voltage vs Thrust Efficiency

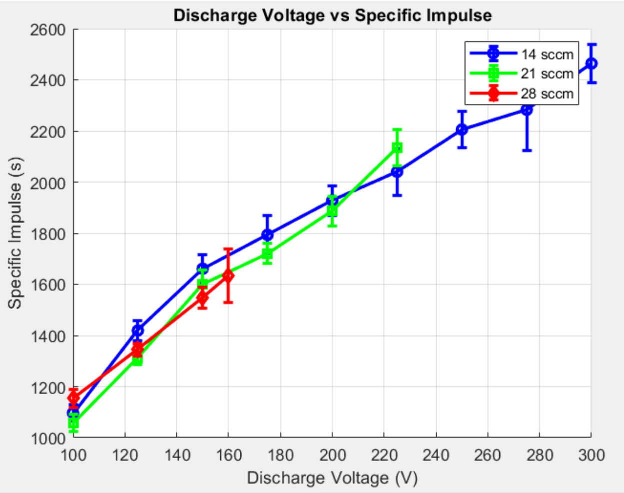

Fig. 6 Discharge Voltage vs Specific Impulse

6. CONCLUSION

Measuring accurate thrust for electric propulsion is notoriously difficult due to the small magnitude of thrusts produced. Accurate measurements of these thrusts are highly important for correctly characterizing thrusts and Isp thrusters are able to produce. With standardized procedures errors in measurements can be mitigated. Following standards through using highly precise measurement techniques like pendulum thrust stands and proper calibration for this equipment can assist in reducing measurement errors that occur. Optimization of procedures is a continuous effort to obtain more precise measuring techniques and hone available methods further. Also, ensuring that measurements taken follow physically explained outcomes solidify the validity of each test.

REFERENCES

[1] Polk, J. E., Pancotti, A., Haag, T., King, S., Walker, M., Blakely, J., & Ziemer, J. (2024, April 4). *Recommended practices in thrust measurements*. Root. https://hdl.handle.net/2014/44429

[2] R. Jahn, Physics of Electric Propulsion, McGraw–Hill, New York, 1968 Chaps. 6–8.

[3] Sasoh, A., Kasuga, H., Nakagawa, Y., Matsuba, T., Ichihara, D., and Iwakawa, A., “Electrostatic-magnetic-hybrid thrust generation in central-cathode electrostatic thruster (CC-EST)”, Acta Astronautica, vol. 152, pp. 137–145, 2018. doi:10.1016/j.actaastro.2018.07.052.

[4] J.E. Jones, and M.D. Cox, Thrust Stand for Electric Propulsion Performance Evaluation* T.E. Markusict, NASA Marshall Space Flight Center, Huntsville, AL, 3576

[5] Ichihara, Daisuke, Uno, Tomoki, Kataoka, Hisashi, Jeong, Jaehun, Iwakawa, Akira, Sasoh, Akihiro, *Ten-Ampere-Level, Applied-Field-Dominant Operation in Magnetoplasmadynamic Thrusters*, Journal Article, 2017, Journal of Propulsion and Power, 360-369, 10.2514/1.B36179 [doi] Journal of Propulsion and Power March 33(2):360

[6] NASA. Specific Impulse. *Nasa.gov*. https://www.grc.nasa.gov/www/k-12/airplane/specimp.html.

[7] Sasoh, A., & Arakawa, Y. (1993, March 1). *A high-resolution thrust stand for ground tests of low-thrust space propulsion devices*. AIP Publishing.

[8] Ryota Nakano, Daisuke Ichihara, Akihiro Sasoh, Enhancement of the electrostatic–magnetic hybrid thrust performance using a stagnant ring, Acta Astronautica, Volume 220, 2024, Pages 495-503, ISSN 0094-5765 https://doi.org/10.1016/j.actaastro.2024.04.043.

[9] D. Ichihara, K. Oka, A. Higo, Y. Nakamura, K. Kinefuchi, A. Sasoh, Thrust density enhancement in an electrostatic–magnetic hybrid thruster, J. Propul. Power 37 (2021) 973–976

ACKNOWLEDGMENTS

This research was supported by the Japan-US-Canada Advanced Collaborative Education Program (JUACEP) between Nagoya University and the University of Michigan and was funded by the Japan Student Services Organization (JASSO) scholarship. I give my upmost appreciation to my advisors and colleagues for their invaluable guidance and support.

JUACEP Independent Research Report
Nagoya University, Japan

Optimization of Robust LiDAR SLAM framework for Predictive World Modeling Integration

Luna Xiaoyue Wu[1], Robin Karlsson[2], Alexander Carballo[3], Kento Ohtani[4], Keisuke Fujii[5] and Kazuya Takeda[6]

[1]Department of Mechanical Engineering, University of Michigan, Ann Arbor, USA
[1]wxyluna@umich.edu
[2]Graduate School of Informatics, Nagoya University, Nagoya, Japan
[2]karlsson.robin@g.sp.m.is.nagoya-u.ac.jp
[3]Department of Electrical, Electronic and Computer Engineering, Gifu University, Gifu, Japan
[3]alex@gifu-u.ac.jp
[4]Graduate School of Informatics, Nagoya University, Nagoya, Japan
[4]ohtani.kento@g.sp.m.is.nagoya-u.ac.jp
[5]Graduate School of Informatics, Nagoya University, Nagoya, Japan
[5]fujii@i.nagoya-u.ac.jp
[6]Graduate School of Informatics, Nagoya University, Nagoya, Japan
[6]kazuya.takeda@nagoya-u.jp

***Abstract*—LiDAR SLAM (Simultaneous Localization and Mapping) involves using continuous 3D point cloud scans to map an area while tracking the robot's location within it. This paper builds upon the concept of Predictive World Models (PWM) from real-world partial observations [5], focusing on creating consistent concatenated point clouds to improve the model's performance. The purpose is to pave ground for PWM's application on actual robots by implementing a comprehensive SLAM framework with minimal dependencies, loop-closure-detection and ideally excluding IMU usage. The study evaluates the performance of NDT scan matching based li-slam-ros2 and compares its robustness and applicability in a ROS 2 environment with ICP-based LIO-SLAM using the KITTI-360 dataset. Results indicate that compared to LIO-SAM, li-slam-ros2 is a more lightweight and user-friendly framework for generating dense point cloud maps without mandatory IMU dependency.**

1. INTRODUCTION

The fundamental goal of autonomous vehicles (AV) and advanced driving assistance systems (ADAS) is reducing accidents, yet several accidents has been reported as such vehicles are deployed in the real world. To drive safely in a world mixed with conventional (non self-driving) vehicles, self-driving vehicles are required to deeply understand the driving environment and learn what is the behavior of the road participants in order to decide the correct driving behavior of the ego-vehicle. One of the key technologies used is knowing the ego-vehicle's posture in the surrounding environment, namely, self localization. Traditionally, self localization requires known prior maps of the environment to find the vehicle's bearings. Such high definition maps include details such as 3D configuration of the environment with features for self localization, road topology, traffic lights, driving directions, speed limits, traffic flow, etc. However, when using precise 3D LiDARs, map creation and the sensors' corresponding maintenance requires a considerable cost. There are several ongoing efforts for map-less navigation, where the ego-vehicle discovers its position, the road topology, maximum speeds and other elements; among such efforts, Predictive World Models (PWM) has been proposed.

This work was part of the Japan-US-Canada Advanced Collaborative Education Program (JUACEP) internship. The assigned project consisted in exploring LiDAR-based simultaneous localization and mapping (SLAM) methods to reduce the problem of polluted training samples in Nagoya University's PWM approach, which uses a hierarchical variational autoencoder (HVAE) to predict a diverse range of plausible worlds based on accumulated sensor observations.

The PWM is able to use HVAEs to predict complete states from partially observed data. The process of PWM is shown in Fig.1. With spatial information gathered from sensor observations (point clouds generated from LiDAR) and semantic segmentation gathered from camera's RGB picture, ICP is used to accumulate the observations and stack them in the common semantic vector space. The accumulated observations are generated into bird's eye view (BEV) as past observations; the semantic point cloud observation upon that time is the current observation. Based on the present observation, the PWM is able to generate a set of plausible worlds using its past "memory" (past observations). The PWM can have several use cases, such as when the ego vehicle's perspective is being blocked and it needs to imagine occluded regions to make decision. SLAM means Simultaneous Localization and Mapping. It is a vital part in modern robotics for both indoor and outdoor usage, where a robot can create a map in the area it spans and localize it within the map it creates. SLAM has proven to be essential for autonomous units that operate in unknown environment, from Romba that cleans the house floor

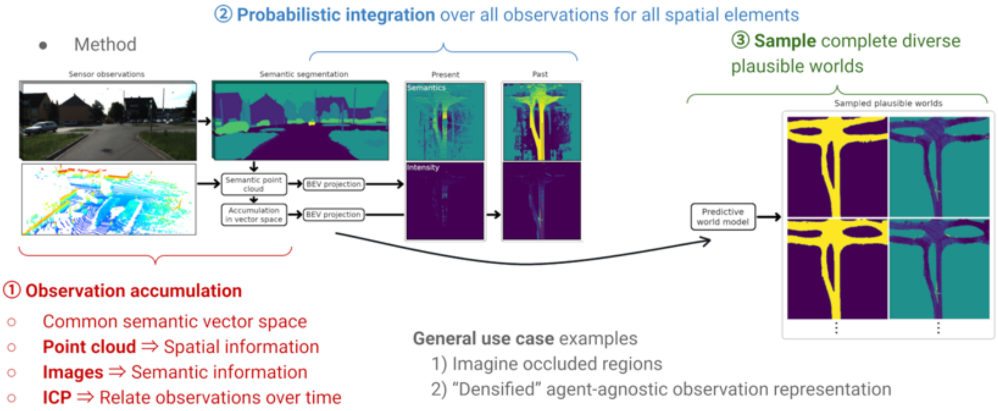

Fig. 1. Predictive World Models from Real-World Partial Observations [5]

to rescue robot and surveillance drones that secure safety for front-line rescuers. To build upon the PWM research's context, the main focus will be LiDAR-based SLAM which relies on LiDAR odometry.

The Iterative Closest Point (ICP) algorithm is one of the most important geometric alignment algorithm for three-dimensional point cloud registration. ICP algorithm was also used to estimate the sensor's motion and align sequential observations as accumulated point clouds [4] in PWM which is mentioned earlier. However, ICP scan sometimes create jumps and lacks loop closure, occasionally creates inaccurate or erroneous input sample as shown in Fig.2, where red represents road, drivable or asphalt; green represents vegetation, plant, statics; blue represents the ground. The three images are semantic point clouds that represents past-to-present accumulated observations, present-to-future accumulated observations and past-to-future observations. The overlapping red trajectory in the present-to-future observations indicates an ICP failure, resulting in trajectory overlap in past-to-future prediction in the right image. Also, as the real-time performance of the PWM is desired to be tested on robotic platform, a practical feature that can be integrated into the model is desired. Thus, an all-encompassing SLAM feature becomes a potential solution. The goal of this study is to explore and optimize other SLAM methods which overcome jumps in ICP and include loop-closure detection. Meanwhile, for the sake of simplicity, easy implementation and more versatile use case, the emphasis of the study would be to identify a SLAM framework with minimal dependency (ex. preferable IMU input). In summary, the objectives of this internship work are:

- Download and get familiarize with the KITTI360 [9] Raw Velodyne Scans (119G) data structure.
- Read the KITTI360 data using the Point Cloud Accumulation Library (PAL) [5].
- Experiment with own SLAM-based (fast) code and obtain [x, y, z, R, G, B] format segmented accumulated point cloud.
- Consider how to store the segmented accumulated point cloud into sub-point clouds given a time stamp ts that splits point clouds as 'past' and 'future'
- Train a new VDVAE (Very Deep VAE) [2] model on the RGB segmented point cloud.

Fig. 2. Occasional ICP failures resulting polluted samples

The rest of this report is structured as follows: In Section 2 we present background information concerning the technologies related to this work. In Section 3 we present the details of the methods used to solve this problem, while in Section 4 we present the results achieved. In Section 5 we provide in depth discussions regarding the results, and in Section 6 we present the conclusions and lessons learned. An appendix is included with additional results.

2. RESEARCH BACKGROUND

A. *Iterative Closest Point (ICP)*

The iterative closest point (ICP) algorithm is a method that aligns two sets of point clouds by finding the closest distance between them. The output of ICP is a translation vector $\mathbf{t}$ and a rotation matrix $\mathbf{R}$ such that, when applied to the second point cloud set, will ideally match with the first set with minimal error. The process starts by finding the closest point of the second set of point clouds with the first set of point clouds, and gradually matching the corresponding points together by minimizing the residual between points. The process of determining the association is repeated as necessary, meaning it will iteratively find the closest point to the other set of point clouds [19]. ICP is a clean and simplistic approach towards the essence of points matching and have been integrated with various other features. Built based upon standard ICP, other methods such as Generalized-ICP (GICP) [16] that combines ICP and point-to-plane ICP together, provides greater robustness to incorrect correspondences and improving overall accuracy in point cloud matching.

B. Normal Distributions Transform (NDT) scan matching

The NDT (Normal Distributions Transform) algorithm is a scan matching technique where the scanned space is partitioned into cells and it enhances the convergence area by adjusting the eigenvalues of the normal distribution. In this approach, the points in the reference point cloud are divided into 3D voxels, where each voxel i is a 3D normal distribution represented by a mean vector $\mu_{\mathbf{i}}$ and covariance matrix $\mathbf{\Sigma_i}$. For each point in the input scan, the closest 3D voxel in the reference scan is identified to estimate the relative pose between the two scans [21]. The convergence algorithm involves three main steps: searching for neighboring cells, expanding the normal distribution, and fusing data around the less populated reference cell.

C. KITTI-360

KITTI360 [9] is a large scale dataset that recorded several suburbs of Karlsruhe, Germany, consisting over 320k images and 100k laser scans in a driving distance of 73.7km. For the data collection, it was equipped a station wagon with one 180° fisheye camera to each side and a 90° perspective stereo camera (baseline 60 cm) to the front. There is a Velodyne HDL-64E and a SICK LMS 200 laser scanning unit in pushbroom configuration on top of the roof. Since the original work of the Predictive World Model utilizes the KITTI360 data set's Velodyne raw data, this study inherits the same approach and will build upon working with the same dataset.

D. LiDAR SLAM

A typical Autonomous vehicle (Fig.3) contains four key parts: localization, perception, planning, and control [24]. Perception means the autonomous vehicle collect data of the road environment it operates in, whether its flow of data or images; localization means positioning itself in the active running process. Combining perception and localization, the relationship between the local coordinate and the world frame can be found, resulting in the process of mapping. Planning utilizes localization, perception and mapping to determine the most efficient and effective subsequent driving epochs for optimal performance. Planning is executed via automobile's control system, such as brake pedal. cruise control or lane keep to perform desired task. For achieving higher levels of automation, mapping is essential for path planning, decision-making, and other advanced tasks. Autonomous vehicles typically use three-dimensional LiDAR sensors to gather environmental data, and SLAM processes this input into concatenated point clouds to build a comprehensive map.

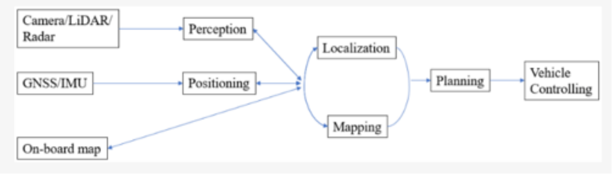

Fig. 3. A typical autonomous vehicle structure [24]

Three-dimensional LiDAR sensor uses laser light beam to determine spatial information around it. Laser beams are emitted from transmitters in LiDAR which fires pulses of light that will be reflected off from surfaces and return to the receiver. The time it takes for the light beam to travel indicates the distance from the sensor to the reflected surface. Then the sensor yields a set of point cloud data that can be projected in to three-dimensional space. The information can tell the distance, feature, location and texture of its surrounding environment.

The inertial measurement unit (IMU) is a electronic unit that measures three dimensional displacements on the X, Y, and Z axis and angular rate (roll, pitch and yaw). It usually comes with accelerometers and gyroscopes. IMU is widely used in modern devices, vehicles or platforms to determine change in motion, which is a vital component in calculating vehicle poses in SLAM.

Loop-closure detection refers to ”detecting for a closed-loop” task in the context of SLAM. It can tell whether the ego vehicle has visited the same place before after a certain time interval. A reliable loop-closing performance indicates the robustness and accuracy of a SLAM framework.

E. Robotic Operating System 2 (ROS2)

The Robot Operating System (ROS) is a set of software libraries and tools for building robot applications. Within the ROS workspace, data is being communicated as messages under different categories named as topics. The data is being transferred through the action of publishing and subscribing in between different nodes, which allows for flexible and modular system architectures. In ROS2, the communication model remains centered around nodes, topics, and messages are similar as ROS. ROS2 is designed to address the limitation of ROS. It enhances communication between nodes using the DDS middleware, offers improved real-time performance, scalability, and security. ROS2 supports cross-platform development and introduces lifecycle management for controlled node states. Additionally, it natively supports multi-robot systems and offers Quality of Service (QoS) settings for fine-tuning communications [10].

3. METHODOLOGY

A. KITTI360 Dataset Study

By using the provided kitti360Scripts [8] dataset utility scripts package, a two-dimensional visualization and depth information of the Raw Velodyne Scans sequence 0 (Fig.4) and sequence 2 (Fig.5) were obtained. The projected depth of each individual laser point is indicated by an RGB color spectrum, with red color being the farthest and blue being the closest.

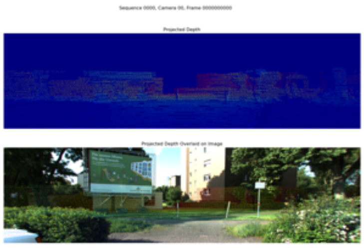

Fig. 4. Visualization of sequence 0 camera 0 frame 0

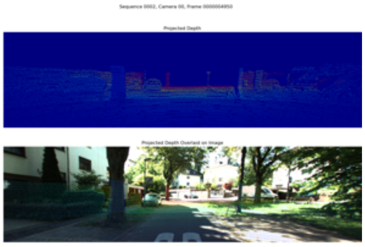

Fig. 5. Visualization of sequence 2 camera 0 frame 4950

B. Birds Eye View (BEV) Generation with PAL

The point cloud accumulation library (PAL) is a library within the PWM package [5] for temporal accumulation of semantic point clouds generated from image and LiDAR senor data. The dependencies are Open3D, ONNX Runtime and PyTorch. It converts the accumulated segmented point clouds into BEV tensor as a compatible format for PWM input. The generated BEV from KITTI360 sequence 0 using one camera and lidar is shown in Fig.6. The top row images indicates semantics, where yellow represents road or drivables; purple represents ”non-road”. The middle row indicates point cloud intensity and the third row shows segmented point clouds. The very last image shows semantic segmentation output.

C. Data Pre-processing

Before running the KITTI360 dataset in ROS2, necessary data preprocessing was required. The KITTI360 data needs to be converted into ROS2 acceptable format, such as through a ros2 bag or ros2 node. Since the official KITTI360 Script package does not have a node for publishing data in the ROS2 environment, the `kitti_to_ros2bag` [12] package was used to convert KITTI360 data into a ROS2 bag that includes `sensor_msgs/PointCloud2` and `sensor_msgs/Imu` information as the minimal required dependencies, following the initial motivation of keeping as little dependencies as possible.

D. LIO-SAM

LIO-SAM is a widely used real-time LiDAR-inertial odometry package that integrates LiDAR and inertial data with a factor graph, allowing various sources of information to be incorporated into the system. LIO-SAM requires input from LiDAR sensors (such as Livox, Velodyne, Ouster, Robosense), a 9-axis IMU, and optionally, GPS data. It features scan-context which is an egocentric spatial descriptor for place recognition within 3D point cloud map [6]. The system architecture of is shown in Fig.7, which consists of four essential parts: imuPreintegration, imageProjection, featureExtraction and mapOptimization. ImuPreintegration subscribes to IMU data and LiDAR odometry and publish IMU odometry; imageProjection subscribe to pointcloud, imu data and odometry data to publish `cloud_info` message;featureExtraction adds edge extraction and planar feature into `cloud_info`; with `cloud_info` messages and GPS data, mapOptimization would be able to publish graph-optimized LiDAR odometry to create a consistent map. Having such well-structured and detailed SLAM pipeline requires well-structured rosbag consisting all necessary dependencies to run the framework properly.

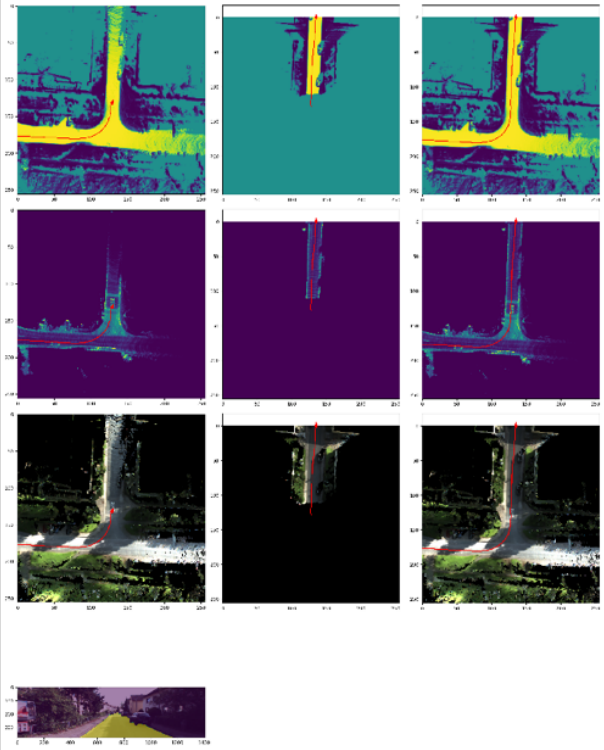

Fig. 6. Generated BEV of KITTI360 sequence 0 using PAL

Upon implementing the converted KITTI ROS2 bag into the LIO-SAM framework, several problems had persisted.

Since the original KITTI360 dataset is missing the LiDAR ring number information, ImageProjection couldn’t work properly, resulted in no point cloud being loaded. As shown in

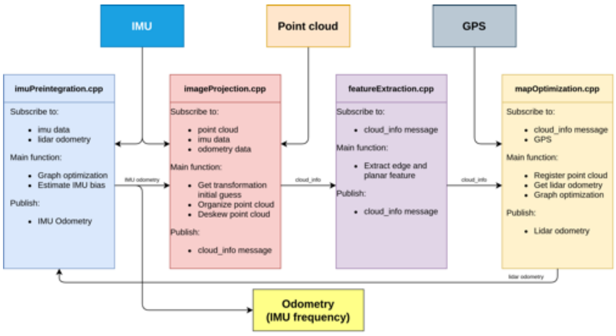

Fig. 7. LIO-SAM system architecture [17]

Fig.8, for 64-channel Velodyne HDL-64E, θ determines the rotation and ϕ determines the alzmith of each laser beam. With 32 channels on both the upper and lower blocks of HDL-64E, a total of 64 laser beams are fired to collect densely populated poincloud data. Ring number helps with identifying different LiDAR beam layers which is a vital part in projecting the point clouds for visualization in LIO-SAM pipeline. The Velodyne HDL-64E LiDAR has vertical field of view +2 to -8.33 with 1/3 degree spacing and -8.83 to -24.33 with 1/2 degree spacing, 26.8 degree vertical field of view (elevation) -+2 up to -24.8 down with 64 equally spaced angular subdivisions (approximately 0.4) [22]. Firstly, continuous pitch angle (elevation angle ϕ) that is used to calculate ring index can be calculated as Eq. (1):

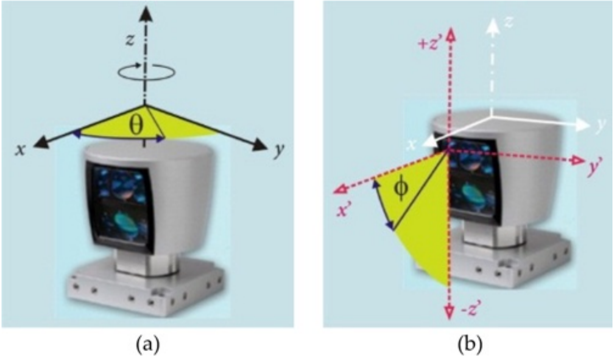

(a) (b)

Fig. 8. Velodyne HDL-64E angles [1]

$$\phi = \arcsin\left(\frac{z}{\sqrt{x^2 + y^2 + z^2}}\right) \tag{1}$$

1. For $\phi \geq -8.83°$:

$$\text{rowIdn} = \lfloor (2 - \phi) \times 3.0 + 0.5 \rfloor$$

This formula accounts for the 1/3 degree spacing, scaling the angle difference by 3. The + 0.5 ensures rounding to the nearest integer.

2. For $\phi < -8.83°$:

$$\text{rowIdn} = \frac{64}{2} + \lfloor (-8.83 - \phi) \times 2.0 + 0.5 \rfloor$$

Here, the formula scales the angle difference by 2 for 1/2 degree spacing and adjusts the row index to account for the previous rows. Points that are outside the valid vertical field of view (greater than 2 degrees or less than -24.33 degrees) or if the calculated row index is invalid (greater than 64 or less than 0) are filtered out. After implementing this and a forked version imageProjection [18] into imageProjection, the point cloud data could be projecting into the ROS2 graphical interface Rviz2.

However, drifting appears when loading IMU and point cloud upon initialization, resulting in failure for reconstructing the point cloud map as shown in Fig.9. There are numerous factors that potentially cause this to happen and will be discussed in the discussion section.

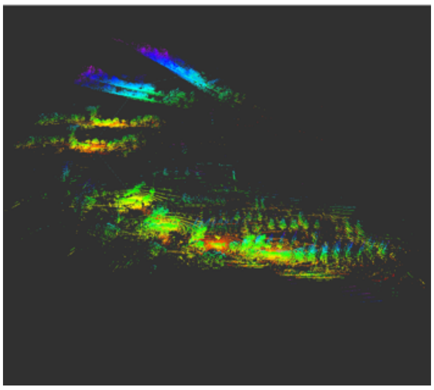

Fig. 9. Drifting upon initializing mapping process

E. *li-slam-ros2*

The open-sourced package is an extended work built upon lidarslam-ros2 [14], which is a light-weight ros2 slam open-sourced package with frontend using OpenMP-boosted NDT algorithm [7] that is SSE-friendly and multi-threaded, which runs ten times faster than its original version in point cloud library according to the provided benchmark comparison in Table I. OpenMP-boosted pcl(DIRECT1, 8 threads), with a run time of 16.7266msec, out performs the original NDT algorithm provided in pointcloud library, whose run time is 425.142msec. The backend of this package uses graph-based slam. Besides the lidarslam-ros2 backbone, this package also adapts IMU integration from LIO-SAM's imuPreintegration. Compare to lidarslam-ros2, li-slam-ros2 [15] has better performance on long-distance dataset and was able to provide satisfactory result upon its implementation.

Upon running the package with long-distance KITTI360 Velodyne raw data sequence 0, consistent concatenated point cloud map was generated. When the ego vehicle made a T turn at a stop, the framework is able to accurately match the points together and complete loop closure detection (Fig.10), as the green path for modified map trajectory with loop-closure and yellow path for map trajectory merges together in Fig.11. The framework is able to produce high-quality dense map

TABLE I
BENCHMARK COMPARISON OF PCL AND PCL-OMP NDT IMPLEMENTATIONS [7]

Method (NDT)	Single [msec]	Fitness
`pcl`	425.142	0.213937
`pclomp (KDTREE, 1 thread)`	308.935	0.213937
`pclomp (DIRECT7, 1 thread)`	188.942	0.214205
`pclomp (DIRECT1, 1 thread)`	41.3584	0.208511
`pclomp (KDTREE, 8 threads)`	108.68	0.213937
`pclomp (DIRECT7, 8 threads)`	56.9189	0.214205
`pclomp (DIRECT1, 8 threads)`	16.7266	0.208511

representation with clean building edges, road texture, accurate vegetation and road-side vehicle location.

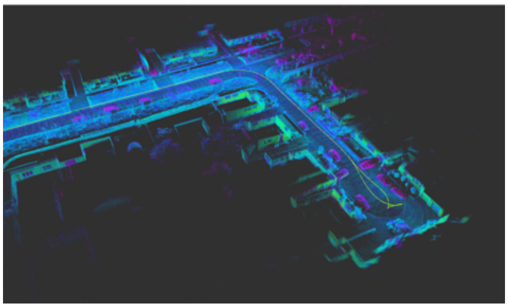

Fig. 10. Successful T-turn

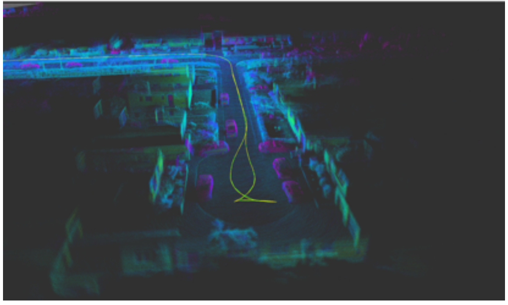

Fig. 11. Successful loop-closure detection

4. RESULTS

Upon running li-slam-ros2, certain problem still persists during mapping long-distance dataset. Drifting happens occasionally when NDT scan matching fails, the reason will be discussed later in the discussion session. A small drift leads to error accumulation in matching, which results in significant offset between the map and ground truth for long-distance dataset. As shown in Fig.12, NDT scan matching failed in matching this segment of point clouds, resulting in a failure of loop closure in Fig.13 (intersection not closing due to misalignment). Similar drift also happened in a later U-turn (Fig.14), where the feature of the load could not align together. Finally, the map representing sequence 0's lower-half section drifted away from the ground truth starting from the lower left where drifting of the U-turn happens, despite the right hand side of the map initially appears to be close to the ground truth (Fig.15). Since running the long-distance dataset sequence 0 is time consuming (four hours on average for

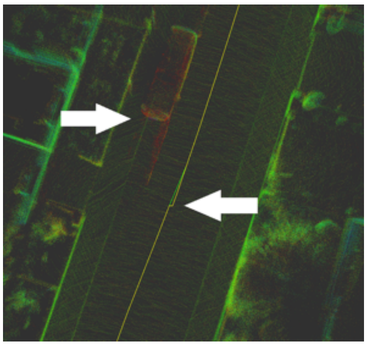

Fig. 12. Small drift due to NDT scan matching failure

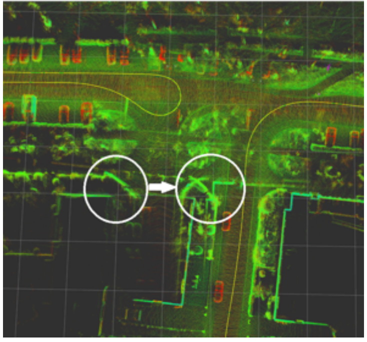

Fig. 13. Loop closure detection at intersection failed

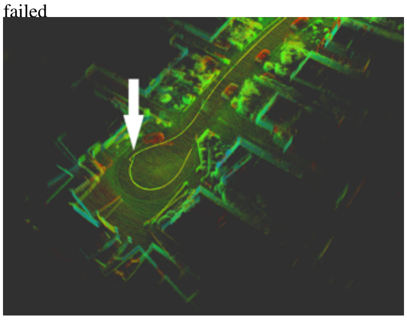

Fig. 14. Unsuccessful U-turn scan matching

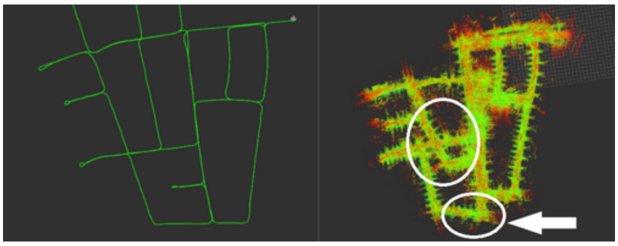

Fig. 15. Ground truth (green trajectory) and generated map for KITTI360 sequence 0's lower half section

each mapping process), for the sake of comparing performance under different sets of parameters within the limit time span of the research, test sample was changed to the smaller open-loop dataset sequence 10 that spans three kilometers. For KITTI360 raw Velodyne points sequence 3, its performance is being tested between different voxel grid input size with a ros2 bag play speed of 10% of the original speed. The mapped trajectory and ground truth trajectory are shown in Fig.16and Fig.17. The ground truth are linearly interpolated due to pose count mismatch between li-slam-ros2's output and the original ground truth file. The difference between ground truth and map trajectory appears to have different length due to the fact that drifting happened half way during the ego vehicle is running a straight road segment with relatively less recognizable features (see Fig.18).

TABLE II
APE W.R.T. TRANSLATION PART (M) FOR $\Delta = 1$ FRAMES USING CONSECUTIVE PAIRS (WITH SE(3) UMEYAMA ALIGNMENT)

Metric	vg_size_for_input = 0.1	vg_size_for_input = 0.5
Max	132.405109	65.813757
Mean	71.001208	34.065833
Median	63.509209	29.641923
Min	5.348601	1.122075
RMSE	79.266206	38.879658
SSE	5365794.226172	1303023.172519
Std	35.241452	18.738911

TABLE III
RPE W.R.T. TRANSLATION PART (M) (WITH SE(3) UMEYAMA ALIGNMENT)

Metric	vg_size_for_input = 0.1	vg_size_for_input = 0.5
Max	4.854812	3.238841
Mean	0.686717	0.540633
Median	0.419178	0.400135
Min	0.014963	0.017295
RMSE	0.968964	0.703898
SSE	800.873962	426.601796
Std	0.683601	0.450764

The absolute pose error (APE) and relative pose error (RPE) are computed using the EVO package [3] to evaluate the accuracy of the map trajectory with respect to the ground truth. For the EVO package, the evaluations of absolute trajectory error ATE and APE after alignment are the same, so APE would be ATE in this context. The ATE parameter assesses the overall effectiveness of the registration algorithm and is widely used in evaluating SLAM algorithm's performance. On the other hand, RPE evaluates the accuracy of the relative pose between two consecutive frames over a specific time interval [20] [23].

As shown in Table II and Table III, APE appears to be significantly smaller for voxel grid input size of 0.5. RPE for 0.1 and 0.5 voxel grid input size appear to be close, but 0.5 voxel grid input size's Sum of Square Errors (SSE) appears to be approximately half of 0.1 voxel grid input size, indicating a better performance that is closer to the ground truth. The XYZ comparison (Fig.22, Fig.26), roll pitch yaw comparison (Fig.23,Fig.27), APE with respect to mapped trajectory (Fig.20, Fig.24), RPE with respect to mapped trajectory (Fig.21, Fig.25) for both voxel grid size for input are attached in the Appendix. The error is scaled and shown based on a RGB spectrum from blue (low) to red (high). For both test trials, mapped trajectory and normalized ground truth have close alignment in the X-Y dimension, but large deviation in the z-direction is observed. Although the pitch yaw motion could be recreated with latency, the SLAM framework fails in recreating the roll motion.

The test trial result with larger dataset KITTI360 sequence 10 which spans 10km with a voxel grid input size 0.5 is attached. Note that due to drifting, there appears to be significant offset between ground truth and mapped trajectory in Fig.19. The XYZ comparsion (Fig.30), roll pitch yaw comparision (Fig.31), APE wwith respect to trajectory (Fig.28) and RPE with respect to trajectory (Fig.29) are attached in the Appendix. Notably, for long-distance datasets, the elevation mapping along the z-axis becomes increasingly inaccurate. The yaw motion is recreated with noticeable latency, and significant deviations in pitch motion are observed, likely due to the z-axis misalignment. Additionally, the roll motion is once again not faithfully recreated, further contributing to the overall mapping inaccuracies.

5. DISCUSSION

The potential reasons that lead to the failure of LIO-SAM mapping initialization could be the following:

- Although timestamps are provided in the KITTI360 dataset, they are not included with the point cloud data. The absence of timestamps in the ROS2 bag leads to a failure in initializing point-cloud de-skewing, which is necessary to compensate for the high acceleration of the ego vehicle and ensure mapping precision. However, since the ego vehicle in KITTI360 sequence 0 initially backed out of a parking space slowly before gradually accelerating, and the mapping process failed immediately, the missing timestamps in the point cloud data may not be the primary cause of the failure.
- Although the ROS2 bag is generated using the provided calibration parameters, the IMU and LiDAR messages in the ROS2 bag are not calibrated. The available open-source calibration packages are primarily designed for ROS1, making the conversion between the original and calibrated bags from ROS1 to ROS2 computationally inefficient.
- Iterative Closest Point (ICP) requires a good initial guess to converge to the correct geometric registration. Without an accurate starting point, the algorithm can struggle to align point clouds properly, leading to suboptimal results. In this case, the robustness of ICP is particularly challenged, as the lack of a reliable initial guess increases the likelihood of incorrect convergence. This sensitivity to initialization makes ICP less suitable for situations where the alignment between datasets is not well known

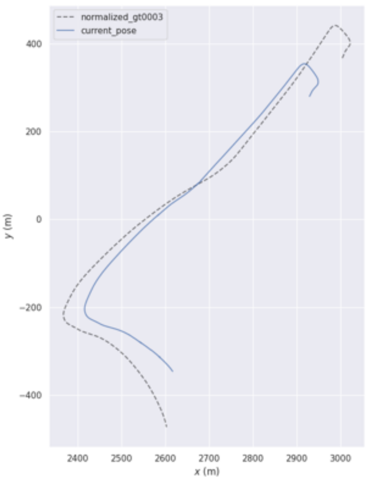

Fig. 16. Mapped trajectory vs. ground truth with voxel grid input size 0.1

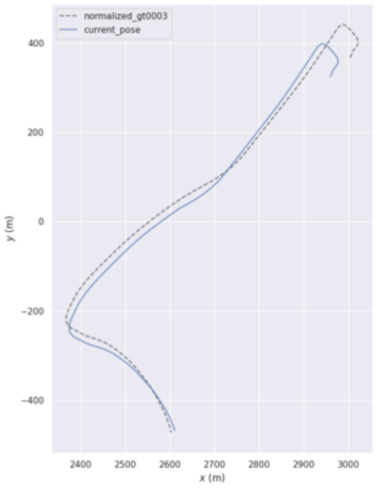

Fig. 17. Mapped trajectory vs. ground truth with voxel grid input size 0.5

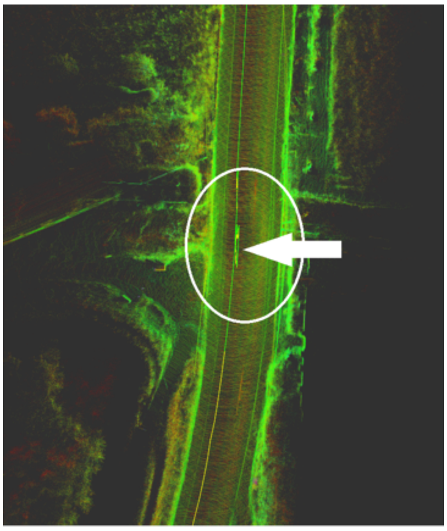

Fig. 18. Drifting happens at position with less features

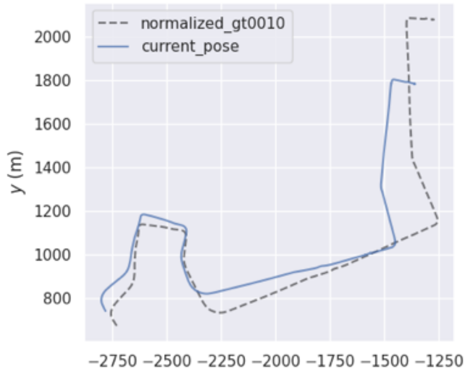

Fig. 19. Ground truth and mapped trajectory for KITTI360 sequence 10 with voxel grid input size 0.5

beforehand, and alternative methods or enhancements may be needed to improve performance.

- Upon observing significant drift in the mapping process, the error message ”Large velocity, reset IMU-preintegration!” appears. This issue may be caused by differences in the publishing rates of the point cloud and IMU data or by discrepancies in processing speeds, leading to latency issues. As a result, misalignment occurs between the point cloud sequence and the IMU data, which can further affect the accuracy of the mapping process.

For li-slam-ros2, The quantitative analysis result shows a much higher error for APE than RPE, indicating that the framework excels in local alignment but struggles with global accuracy. This can be attributed to the fact that LI-SLAM-ROS2's core, NDT scan matching-based lidarslam-ros2, lacks a global localization method for 3D point cloud alignment. As a result, while the mapped trajectory may deviate from the ground truth, it performs better in local alignment over shorter intervals. li-slam-ros2 has loop-closure detection, but is prone to drifting that happens during mapping.

Drifting also happened during the mapping process, potentially due to the lack of calibration between the ROS2 bag's IMU and LiDAR data, insufficient or repetitive features in the environment, or an inappropriate voxel grid size. As demonstrated in the results section, voxel grid size have significant impact on NDT scan matching performance. If it is too small, the algorithm will have difficulties converging and be less robust to errors upon initialization. If the size is too big, the precision of the scan matching will decrease [13].

Additionally, to discuss the effect of having IMU dependency on li-slam-ros2, a mini study using Gifu University campus dataset and lidarslam-ros2 (li-slam-ros2's backbone) is conducted and the yellow line trajectory results (Fig.32, Fig.33) in Rviz2 and ground truth (Fig.34) comparison are attached in the Appendix. Although a quantitative analysis was not performed due to time constraints, it is evident that incorporating IMU data significantly enhances the performance of the NDT scan matching algorithm. The addition of IMU data leads to a more accurate recreation of the ground truth trajectory, highlighting the substantial improvement in performance achieved by introducing this additional pose regulation.

6. CONCLUSIONS AND FUTURE WORK

The challenges faced in the initialization and performance of LIO-SAM and li-slam-ros2 can be traced to several factors related to data handling, calibration, and algorithmic robustness. The absence of timestamps in point cloud data, calibration discrepancies in IMU and LiDAR messages, and the sensitivity of ICP to initial conditions contribute to difficulties in achieving accurate mapping in LIO-SAM. Additionally, the misalignment and latency issues between point cloud and IMU data, particularly under varying velocities, further complicate the mapping process.

In the case of li-slam-ros2, the framework's reliance on NDT scan matching without a global localization method results in better local alignment but poorer global accuracy, as shown by the significantly higher APE compared to RPE. The effectiveness of NDT scan matching is also highly dependent on voxel grid size, with both too small and too large grid sizes leading to reduced performance. Relying solely on point cloud input without incorporating IMU data as a regulatory condition will lead to accumulative errors in the azimuth over time. Without the stabilizing influence of IMU measurements, the system is more prone to drift, especially in rotational estimates, resulting in a loss of accuracy in the overall trajectory. Adding IMU dependency can significantly improve NDT scan matching's performance.

Overall, compared to LIO-SAM, li-slam-ros2 is a more lightweight and easier-to-implement framework for creating dense point cloud maps, with no mandatory IMU dependency. To enhance the performance of these systems, it is essential to address calibration and synchronization issues, fine-tune voxel grid size, and explore alternative methods to improve the robustness of the mapping process across various scenarios and datasets.

Due to time restriction, objectives of creating SLAM map with desired array format from segmented point clouds, partitioning the accumulated segmented point cloud map timestamps into "past" and "future", and training a new VDVAE model with the RGB segmented point cloud were not finished. The study was able to span KITTI360 dataset structure study, running the perception pipeline PAL of PWM on KITTI360 dataset, as well as conducted numerous SLAM frameworks experimentation on non-segmented point cloud data. Potential next steps include integrating a global localizer into li-slam-ros2, generating semantic layers from the framework, and converting concatenated point clouds into recognizable array format using pypcd4 [11] for PWM training.

ACKNOWLEDGMENT

This work was supported by the Japan-US-Canada Advanced Collaborative Education Program (JUACEP) with a scholarship stipend provided by the Japan Student Services Organization (JASSO).

The author would like to express sincere gratitude to Prof. Kazuya Takeda and Prof. Keisuke Fujii for providing the JUACEP opportunity to participate in research at the Behavior Signal Processing Lab in Nagoya University, Nagoya, Aichi, Japan. This experience has been invaluable for learning about 3D LiDAR SLAM and gaining insights from both academic and practical industry perspectives.

Appreciation is also extended to the colleagues in the driving behavior risk group for their support, to Prof. Alexander Carballo for his generous sharing of expertise; to Prof. Kento Ohtani and Mr. Souta Nakanishi from the machine-learning group for facilitating a smooth transition into the lab environment. Special thanks are due to Mr. Robin Karlsson for his guidance on the direction of the summer research based on his work *Predictive World Models from Real-World Partial Observations* and Mr. Khanh Bao Tran for his generous help in sharing work experience in LiDAR SLAM field.

Furthermore, the author is grateful for the opportunities afforded by Prof. Takeda and Prof. Ohtani, which included a visit to Map IV. The visit provided valuable advice from the entire team, including Mr. Ryohei Sasaki, the author of *lidarslam_ros2* and *li_slam_ros2*.

REFERENCES

[1] G. Atanacio-Jiménez, J-J González-Barbosa, J.B. Hurtado-Ramos, et al. Lidar velodyne hdl-64e calibration using pattern planes. *International Journal of Advanced Robotic Systems*, 8(5), 2011.

[2] Rewon Child. Very deep vaes generalize autoregressive models and can outperform them on images, 2021.

[3] Michael Grupp. evo: Python package for the evaluation of odometry and slam. https://github.com/MichaelGrupp/evo, 2017.

[4] Robin Karlsson, Ruslan Asfandiyarov, Alexander Carballo, Keisuke Fujii, Kento Ohtani, and Kazuya Takeda. Open-vocabulary predictive world models from sensor observations. *Sensors*, 24(14), 2024.

[5] Robin Karlsson, Alexander Carballo, Keisuke Fujii, Kento Ohtani, and Kazuya Takeda. Predictive world models from real-world partial observations, 2023.

[6] Giseop Kim and Ayoung Kim. Scan context: Egocentric spatial descriptor for place recognition within 3d point cloud map. In *2018 IEEE/RSJ International Conference on Intelligent Robots and Systems (IROS)*, pages 4802–4809, 2018.

[7] K. Koide. Ndt_omp: Multi-threaded and sse friendly ndt algorithm. https://github.com/koide3/ndt_omp, n.d. Accessed: August 20, 2024.

[8] Yiyi Liao, Jun Xie, and Andreas Geiger. KITTI-360: A novel dataset and benchmarks for urban scene understanding in 2d and 3d. *arXiv preprint arXiv:2109.13410*, 2021.

[9] Yiyi Liao, Jun Xie, and Andreas Geiger. KITTI-360: A novel dataset and benchmarks for urban scene understanding in 2d and 3d. *Pattern Analysis and Machine Intelligence (PAMI)*, 2022.

[10] Steven Macenski, Tully Foote, Brian Gerkey, Chris Lalancette, and William Woodall. Robot operating system 2: Design, architecture, and uses in the wild. *Science Robotics*, 7(66):eabm6074, 2022.

[11] MapIV. Mapiv/pypcd4: Read and write pcl .pcd files in python. https://github.com/MapIV/pypcd4?tab=readme-ov-file, n.d. Accessed: August 20, 2024.

[12] B. PN. Kitti2rosbag2: Kitti2rosbag2 is designed to convert the kitti odometry dataset to ros2 bag format, n.d. Accessed: August 20, 2024.

[13] L. Renaut, H. Frei, and A. Nüchter. Smoothed normal distribution transform for efficient point cloud registration during space rendezvous. In *Proceedings of the 18th International Joint Conference on Computer Vision, Imaging and Computer Graphics Theory and Applications – Volume 5: VISAPP,*, pages 919–930. INSTICC, SciTePress, 2023.

[14] R. Sasaki. lidarslam_ros2: Ros 2 package of 3d lidar slam using ndt/gicp registration and pose-optimization. https://github.com/rsasaki0109/lidarslam_ros2, n.d. Accessed: August 20, 2024.

[15] R. Sasaki. li_slam_ros2: Ros 2 package of tightly-coupled lidar inertial ndt/gicp slam. https://github.com/rsasaki0109/li_slam_ros2, n.d. Accessed: August 20, 2024.

[16] Aleksandr Segal, Dirk Hähnel, and Sebastian Thrun. Generalized-icp. In *Proceedings of Robotics: Science and Systems*, June 2009.

[17] Tixiao Shan, Brendan Englot, Drew Meyers, Wei Wang, Carlo Ratti, and Rus Daniela. Lio-sam: Tightly-coupled lidar inertial odometry via smoothing and mapping. In *IEEE/RSJ International Conference on Intelligent Robots and Systems (IROS)*, pages 5135–5142. IEEE, 2020.

[18] Tixiao Shan, Brendan Englot, Drew Meyers, Wei Wang, Carlo Ratti, and Daniela Rus. Lio-sam: Tightly-coupled lidar inertial odometry via smoothing and mapping (forked by vineet tambe). GitHub repository, 2020. Forked from: https://github.com/TixiaoShan/LIO-SAM.

[19] Erik Smistad, Thomas L. Falch, Mohammadmehdi Bozorgi, Anne C. Elster, and Frank Lindseth. Medical image segmentation on gpus – a comprehensive review. *Medical Image Analysis*, 20(1):1–18, 2015.

[20] Jürgen Sturm, Nikolas Engelhard, Felix Endres, Wolfram Burgard, and Daniel Cremers. A benchmark for the evaluation of rgb-d slam systems. In *2012 IEEE/RSJ International Conference on Intelligent Robots and Systems*, pages 573–580, 2012.

[21] Tomohito Takubo, Takuya Kaminade, Yasushi Mae, Kenichi Ohara, and Tatsuo Arai. Ndt scan matching method for high resolution grid map. In *2009 IEEE/RSJ International Conference on Intelligent Robots and Systems*, pages 1517–1522, 2009.

[22] Velodyne LiDAR. Hdl-64e s2 manual, rev c, 2011, 2011. Accessed: 2024-08-20.

[23] Zichao Zhang and Davide Scaramuzza. A tutorial on quantitative trajectory evaluation for visual(-inertial) odometry. In *2018 IEEE/RSJ International Conference on Intelligent Robots and Systems (IROS)*, pages 7244–7251, 2018.

[24] Shuran Zheng, Jinling Wang, Chris Rizos, Weidong Ding, and Ahmed El-Mowafy. Simultaneous localization and mapping (slam) for autonomous driving: Concept and analysis. *Remote Sensing*, 15(4), 2023.

We include additional results to complement those provided in this report.

Appendix A
LI-LSAM-ROS2 RESULT FOR KITTI 360 SEQUENCE 3 WITH VOXEL GRID INPUT SIZE 0.1

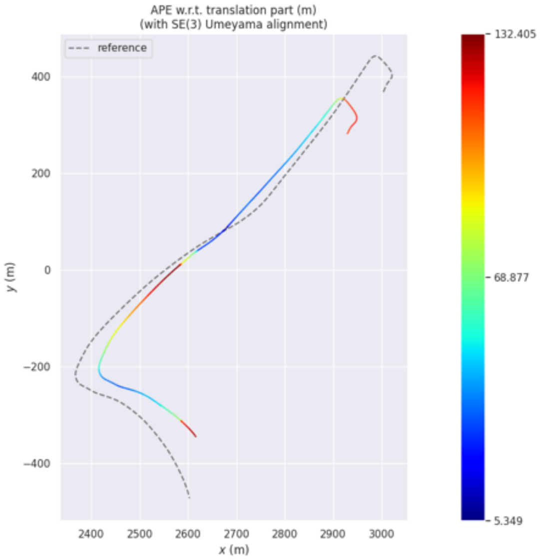

Fig. 20. APE along the mapped trajectory for KITTI 360 sequence 3 with voxel grid input size 0.1

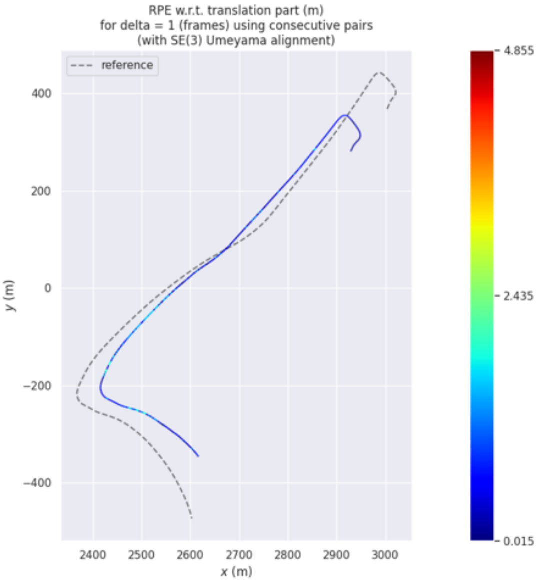

Fig. 21. RPE along the mapped trajectory for KITTI 360 sequence 3 with voxel grid input size 0.1

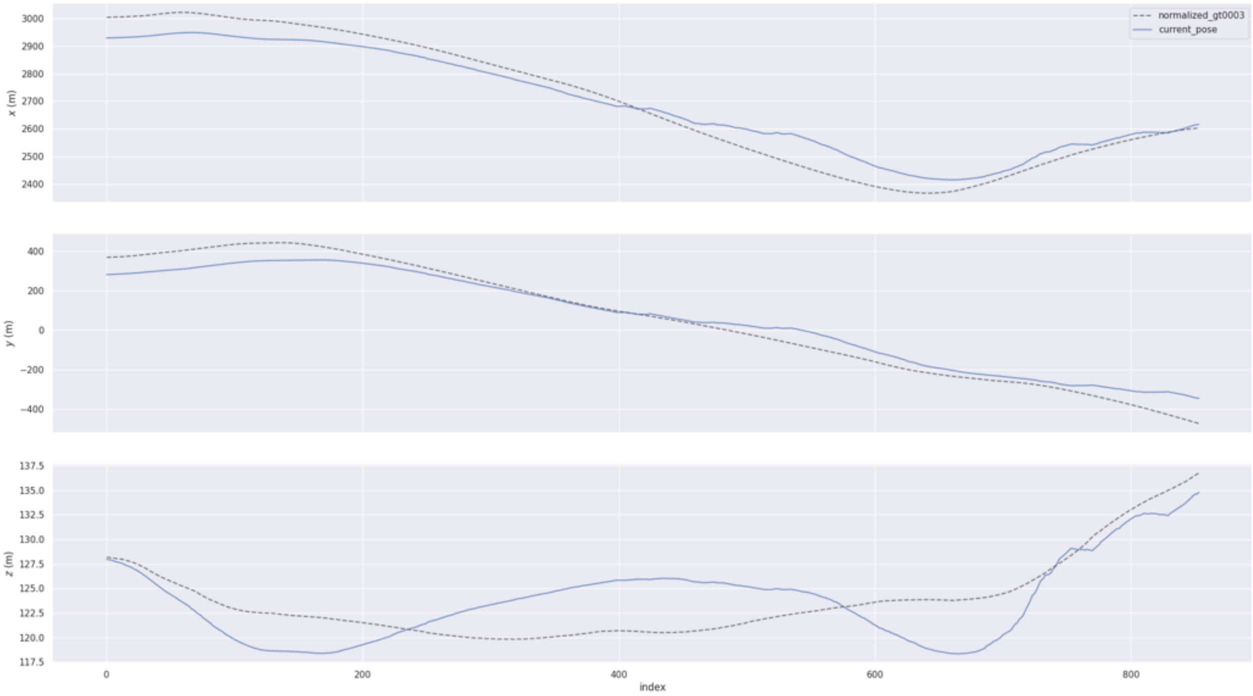

Fig. 22. XYZ alignment between normalized ground truth and mapped trajectory

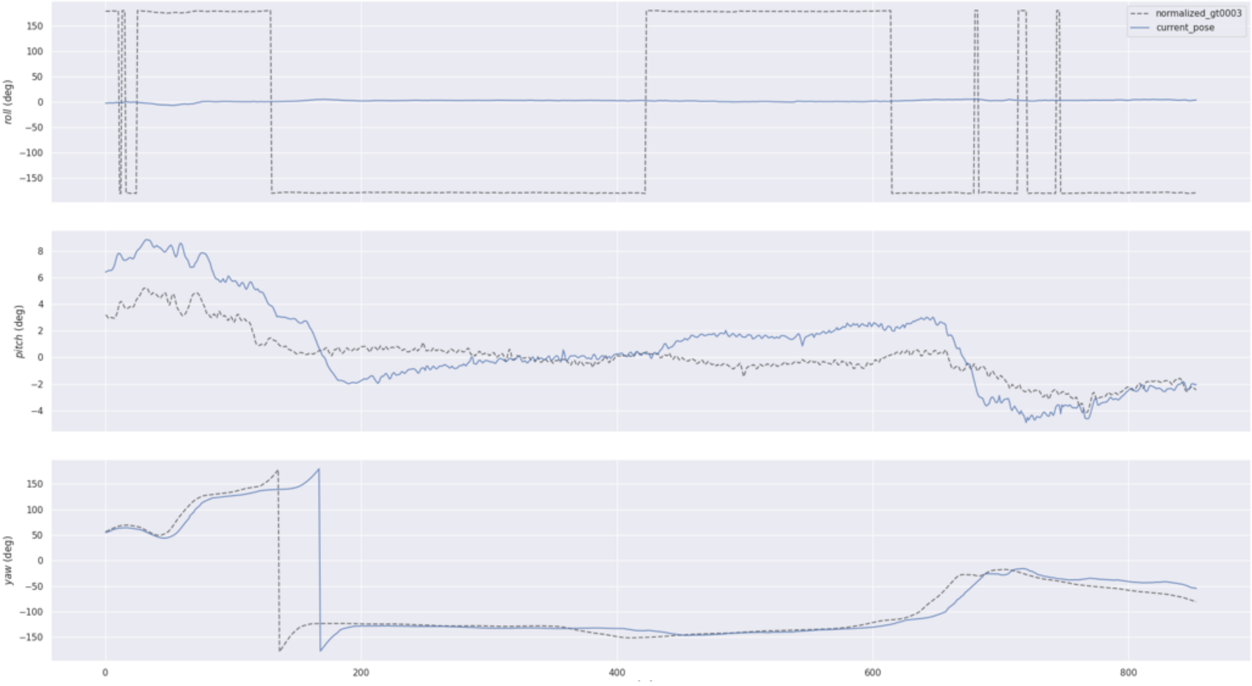

Fig. 23. Roll pitch yaw alignment between normalized ground truth and mapped trajectory

APPENDIX B
LI-LSAM-ROS2 RESULT FOR KITTI 360 SEQUENCE 3 WITH VOXEL GRID INPUT SIZE 0.5

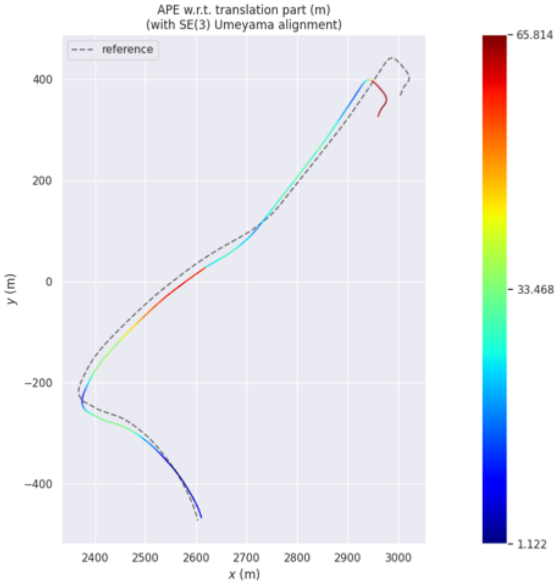

Fig. 24. APE along the mapped trajectory

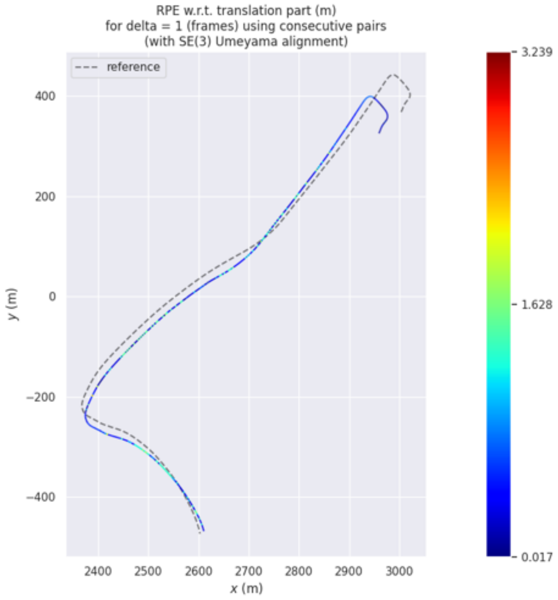

Fig. 25. RPE along the mapped trajectory

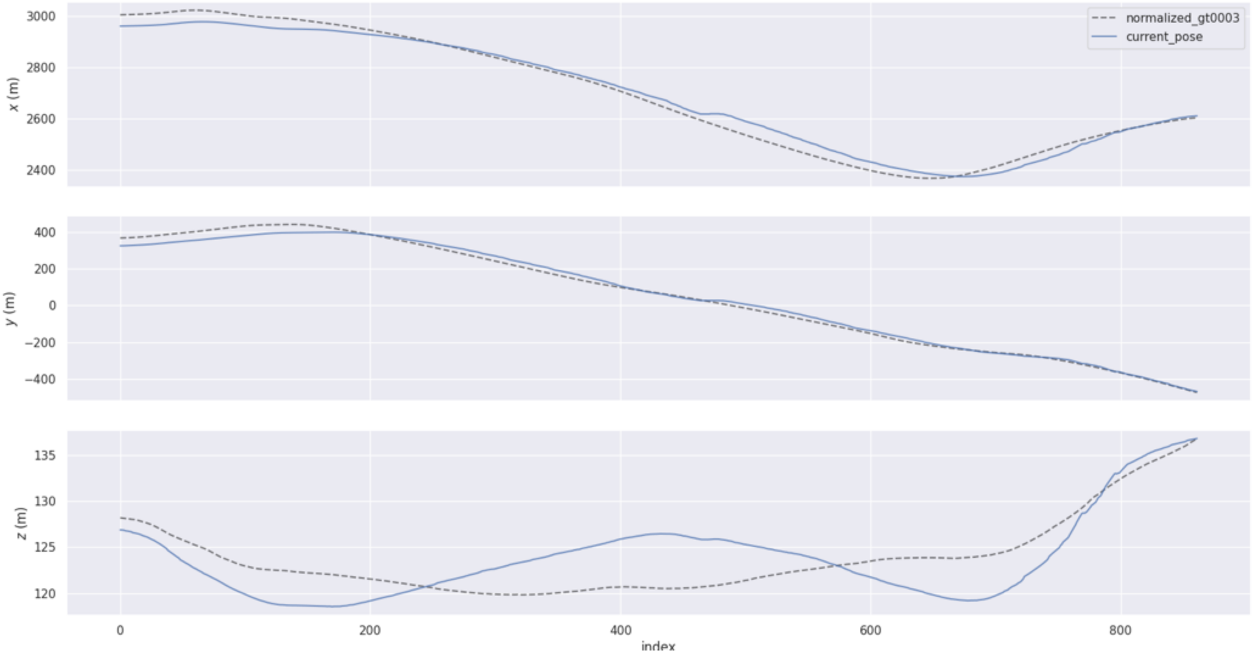

Fig. 26. XYZ alignment between normalized ground truth and mapped trajectory

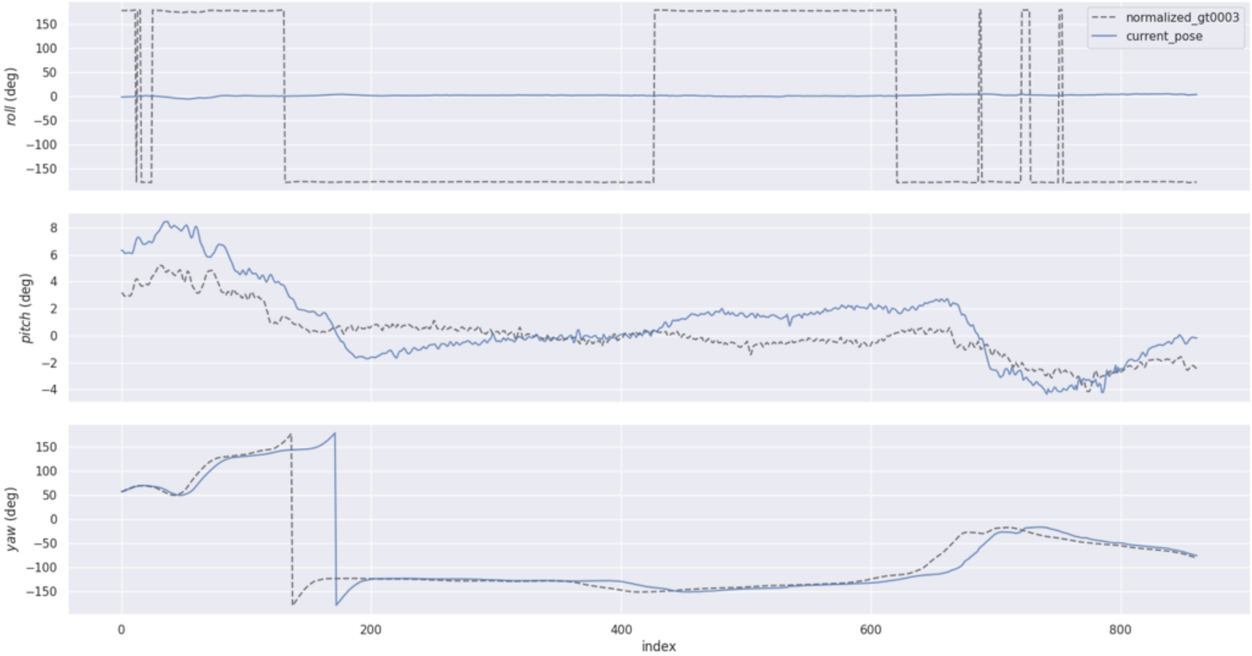

Fig. 27. Roll pitch yaw alignment between normalized ground truth and mapped trajectory

APPENDIX C
KITTI 360 SEQUENCE 10 WITH 0.5 VOXEL GRID INPUT SIZE

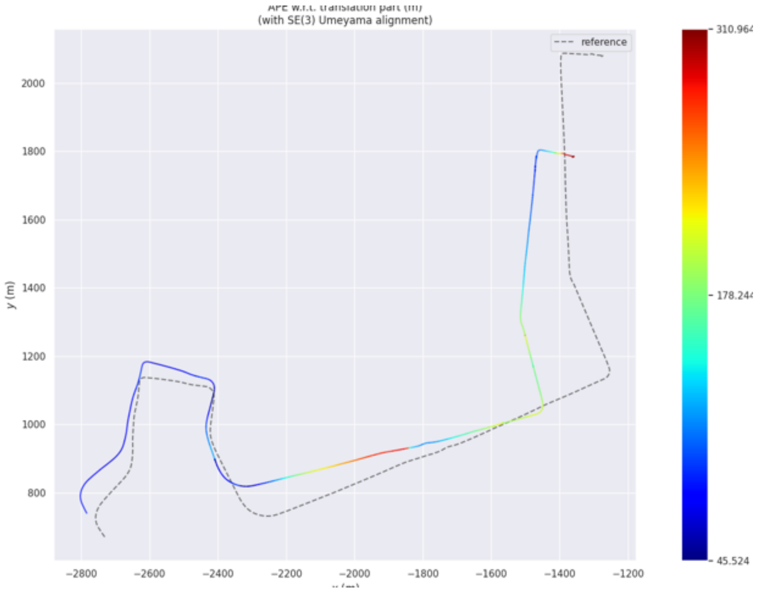

Fig. 28. APE along the mapped trajectory

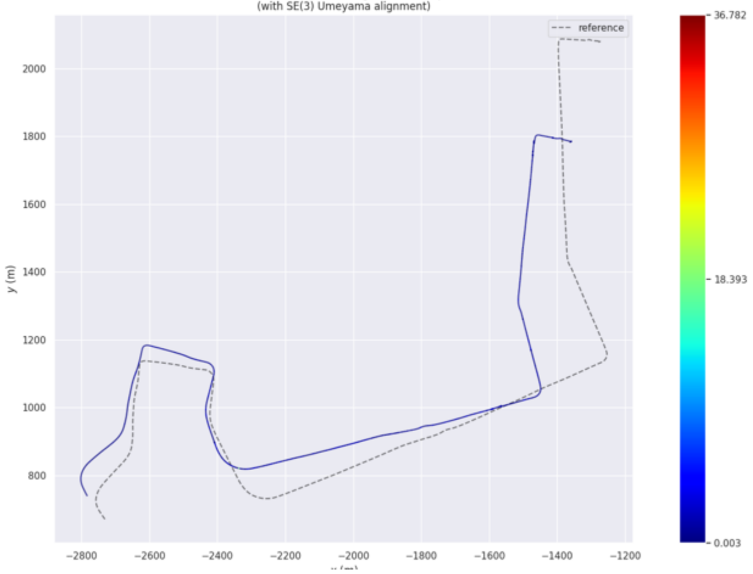

Fig. 29. RPE along the mapped trajectory

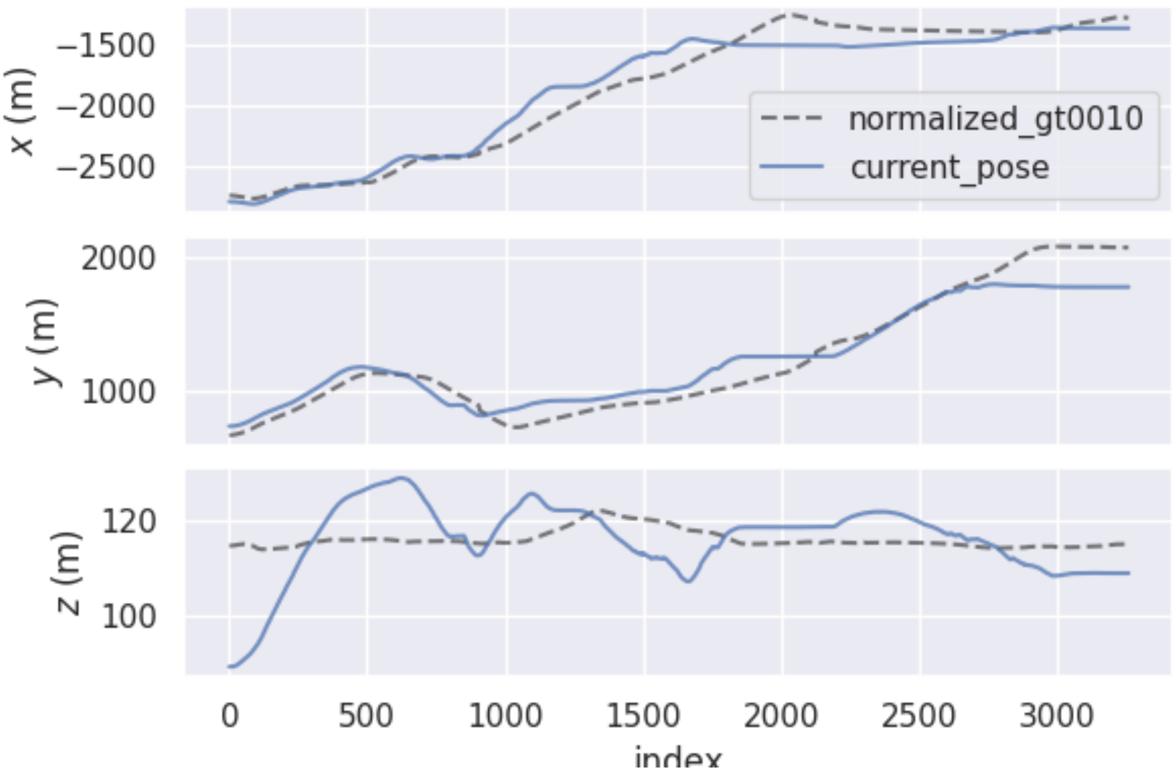

Fig. 30. XYZ alignment between normalized ground truth and mapped trajectory

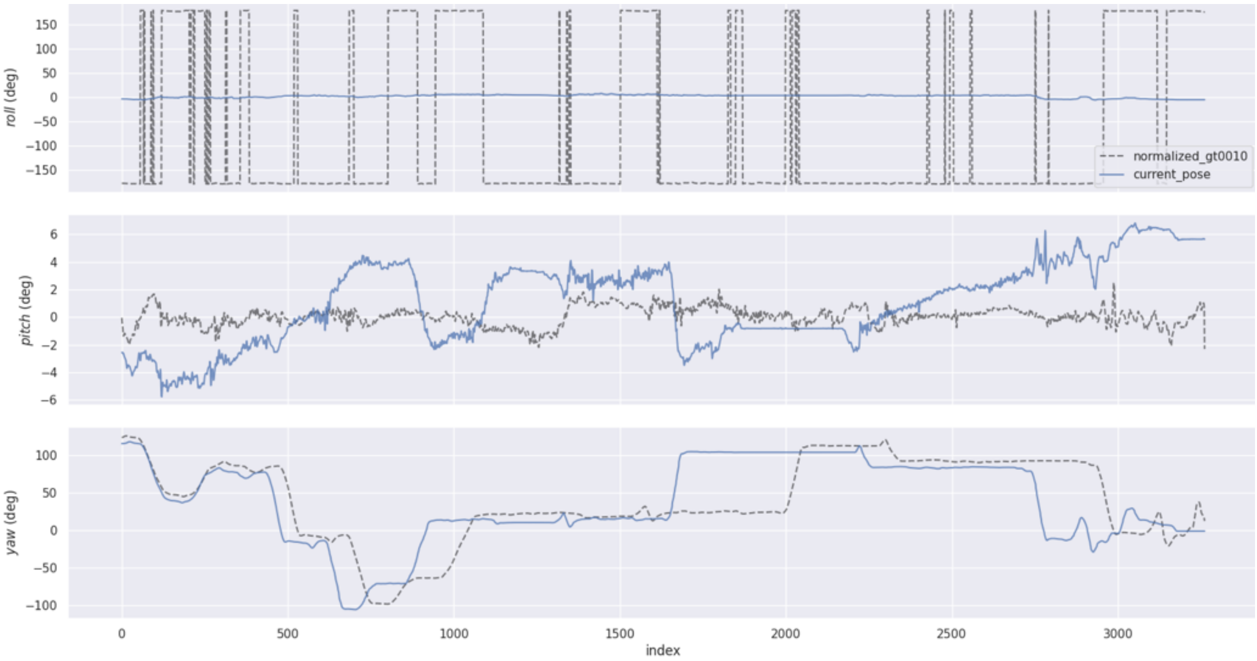

Fig. 31. Roll pitch yaw alignment between normalized ground truth and mapped trajectory

APPENDIX D
LIDARSLAM_ROS2 RESULT FOR GIFU UNIVERSITY CAMPUS DATASET TRAJECTORY COMPARISON

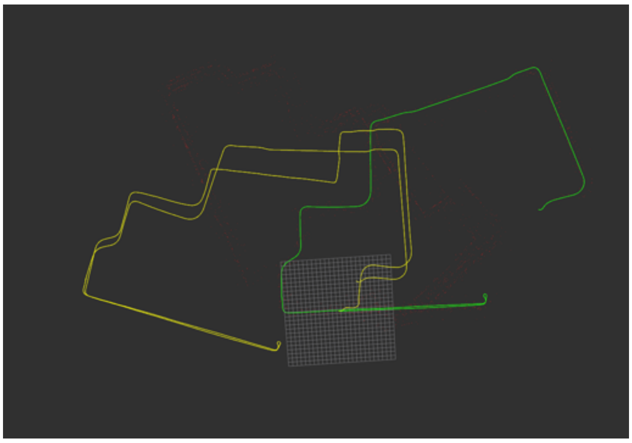

Fig. 32. Mapped trajectory without IMU integration

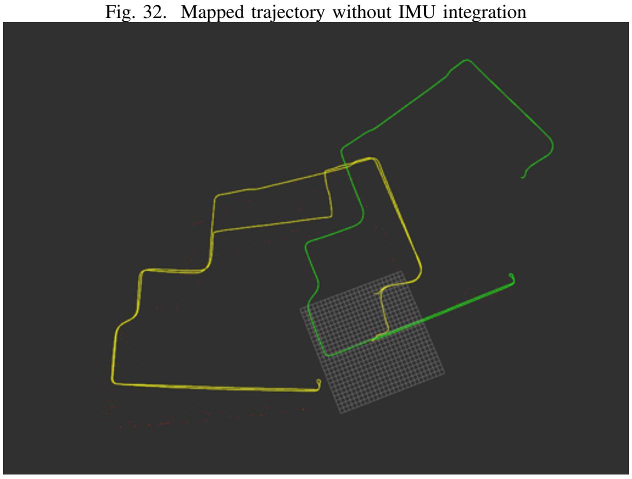

Fig. 33. Mapped trajectory with IMU integration

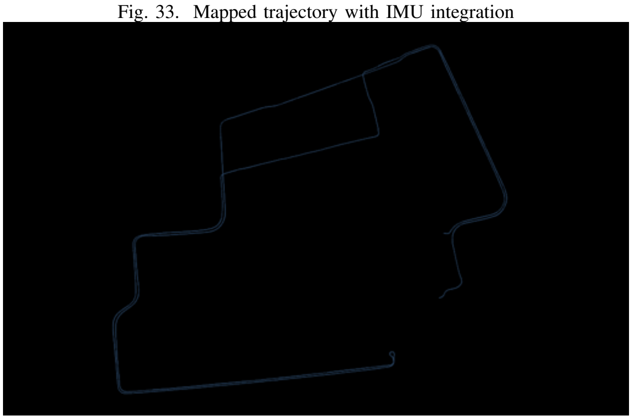

Fig. 34. Ground truth trajectory for the Gifu University campus dataset, generated using LIO-SAM

JUACEP Independent Research Project
Nagoya University, Japan

Impact Assessment of Combination of Secondary and Tertiary Reserve Capacity Flexibility for Reducing Operating Costs in Power Systems with High Penetration of PhotoVoltaic Power in Japan

Gavin Silveira
Department of Integrative Systems + Design, College of Engineering, University of Michigan
gavinsil@umich.edu

Prof. Takeyoshi Kato and Prof. Urabe Chiyori
Department of Electrical Engineering, Graduate School of Engineering, Nagoya University
kato.takeyoshi.b5@f.mail.nagoya-u.ac.jp

ABSTRACT

In order to meet the Japanese government's target of net zero greenhouse gas (GHG) emissions by 2050, significant investment in renewable energy generation is needed. Solar photovoltaic (PV) power is expected to grow exponentially in the coming decades to meet this demand [1]. This renewable energy will replace a large number of spinning generators, which are responsible for providing system interia as well as reserve capacity to ensure that demand and supply power is always balanced. The current industry "rule of thumb" is that the required secondary (also referred to as LFC) capacity should be the greater of either 2% of demand or 10% of solar PV forecast. This approach is conservative and creates a significant reserve capacity requirement as the amount of solar PV in the grid increases. This report explores alternatives to reducing the requirement during peak solar power supply, while still maintaining reliability of the grid.

1. INTRODUCTION

After the Fukushima disaster in 2011, Japan started to divest in nuclear power and begin the process to decommission existing generation. This resulted in an increased reliance on fossil fuels like coal, natural gas, and oil (which are largely imported) to meet their domestic electric power demands. Due to the availability of abundant solar irradiation, solar PV has been the preferred method of renewable energy generation, with an estimated 300 GW of capacity in the year 2050, compared to only 82 GW of wind power capacity [2]. This will represent a significant portion of the power supplied, leading to problems related to the inherent intermittency and zero-interia characteristics of solar power. Spinning generators, particularly coal, liquified natural gas (LNG), oil, and pumped hydro generators are needed to provide primary, secondary, and tertiary control to balance supply and demand, ensuring system reliability. It is important to understand that, unlike most other commodities, electric power cannot be stored (in any meaningful way for utility use) for later consumption. Reserve capacity mechanisms provide vital control to ensure that this balance is always maintained.

The first type of reserve capacity that will be considered is tertiary capacity. This can be divided into up and down reserves, and are primarily used to counteract large unforeseen imbalances between supply and demand in real time. Tertiary reserves are larger, and have slower response times (minutes to hours) compared to primary and secondary reserves. In this report, the need for tertiary reserve capacity is due to forecast errors in solar PV irradiation. The tertiary reserve capacity will be sized depending on the value of load and the largest expected forecast error in the simulation time period (1 hour) [3].

The second type of reserve capacity that will be considered is secondary capacity, also known as load frequency control (LFC) capacity. Secondary reserves are primarily used to balance supply and demand to ensure that the frequency of the grid is at its nominal value (50 Hz or 60 Hz depending on the region in Japan). These reserves have a faster response time (within a few minutes) and are needed to correct any frequency deviation. In this report, the LFC reserve will be responsible for ensuring that any high frequency fluctuations of residual load do not cause an imbalance in the system [3].

The report analyzes the electric power system of the Chubu region in Japan (which contains the industrial cities of Nagoya and Toyota) in the year 2030 to simulate the effects of large renewable energy penetration (particularly solar PV) on the grid. The electricity demand data, solar insolation, wind forecast data, etc. from April 2016 to March 2017 was used in this study. Unlike most other countries, the electric demand in Japan is projected to have a year-on-year *decrease* which allows us to create a conservative estimate for 2030 using historical data [4]. The expected solar PV capacity in 2030 is projected to be

$$PV_{cap} = 16,970\ MW\ in\ 2030 \qquad (1)$$

The demand data is assumed to be exact, i.e. there is no difference between the forecasted values and the actual values. All uncertainty in the system arises from solar PV forecast error. The temporal resolution of the solar PV forecast data is 1 hr while the temporal resolution for the actual solar PV generated is 1 min.

Residual load RL(t) is defined as the difference between the demand De(t) and renewable energy generation (solar PV(t) and wind power WT(t)) at a given time and represents the amount of power needed from conventional generators (nuclear, thermal, hydro)

$$RL(t) = De(t) - PV(t) - WT(t) \qquad (2)$$

In this study, only photovoltaic power is considered, therefore

$$WT(t) = 0 \qquad (3)$$

$$\Rightarrow RL(t) = De(t) - PV(t) \qquad (4)$$

Fig. 1 illustrates the relationship between demand, solar generation, and residual load. During periods of high solar insolation and low demand, it is possible for the residual load to be less than zero. The current inability to store excess energy necessitates the curtailment of solar power to ensure that spinning generators are above their minimum values and are able to provide adequate reserve capacity.

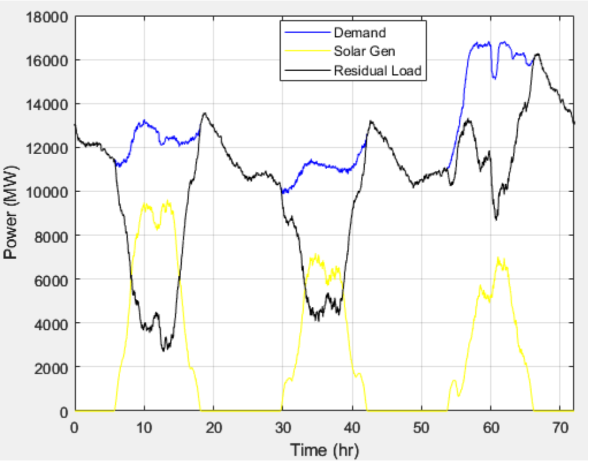

Fig. 1 - Relationship between demand, solar PV gen, and residual load over a 72 hour period in Chubu, Japan (neglecting wind)

Table 1 summarizes the different types and number of conventional generators used in the 2030 simulation of the Chubu area.

Table 1 - Generator assumptions

Type of Generator	No. of units	Max LFC capacity, rr(t)
Nuclear	2	NA
Hydro	4	NA
Coal	16	0.05
LNG	30	0.05
Oil	2	0.05
Pumped Hydro	16	0.20

2.0 METHODOLOGIES

2.1 ORIGINAL MODEL

This report expands on a prior master's thesis at Kato lab and incorporates the sequential optimization of the Unit Commitment (UC) and Economic Dispatch Control (EDC) using GAMS software and its native cplex optimization package [5].

The UC model primarily determines the status of each dispatchable generator (on / off), and PV curtailment, along with their optimal power outputs in 1 hour time increments using forecasted demand and solar PV insolation data. The optimization program aims to minimize the total operating costs (fuel costs + startup costs + shortage/surplus penalties) subject to constraints (supply/demand balance, tertiary capacity requirements, LFC capacity requirements, thermal limits of generators, minimum uptime/downtime of generators, etc.). The UC model runs for a 24 hour period (0:00 to 23:59) at a time. The start/stop states of generators (thermal power plants, hydroelectric generators, pumped hydro generators), and PV curtailment plan for the day determined by the UC model are input variables (exogenous) to the EDC model. The EDC model uses actual 5 minute load and solar insolation data to determine power generation of generators that are running, and water levels of hydro dams, every 5 min for the same 24 hour period analyzed by the UC model.

The objective function to be minimized in the UC and EDC model is the overall operating costs of the system, which includes fuel costs of thermal machines, startup costs of thermal machines, and penalty costs for active power shortages and surplus in the region.

$$COST_{day} = \sum_{1\,day} \sum_{j} [(a_j U_j(t) + b_j P_j(t) + Y_j(t) x_j] + \sum_{1\,day} (S_1(t) + S_2(t))\beta \qquad (5)$$

Where a_j, b_j are fuel cost coefficients (JPY), $U_j(t)$ is the binary operation status (1=on, 0=off), $P_j(t)$ is the active power in MW, $Y_j(t)$ is the startup variable (1=startup), x_j is the startup cost (JPY), $S_1 and\, S_2$ are the shortage and surplus respectively of the Chubu area in MW, and β is the penalty cost of the shortage (JPY/MW), all summed over j thermal machines over every time t. In order to optimize without surplus or shortage, the penalty cost is set to an arbitrarily high value, $\beta = 10,000,000\, JPY/MW$.

For this report, the constraints that are relevant are the minimum secondary (LFC) and tertiary reserve capacity required.

$$\sum_j P_u^{TM}(t) + \sum_g P_u^{PG}(t) \geq De(t) * 0.05 \qquad (6)$$

$$\sum_j P_d^{TM}(t) + \sum_g P_d^{PG}(t) \geq De(t) * 0.05 \qquad (7)$$

Where P_u and P_d are the up and down tertiary reserve capacities respectively. The sum of all thermal machines (TM) and pumped hydro generating (PG) tertiary reserve capacities should be a minimum of 5% of the demand for all time t (hr).

The required secondary (LFC) reserve capacity LFC(t) is determined from rr(t) which is the ratio of each generator's rated capacity allocated for secondary reserves.

$$rr_j(t) = \frac{LFC_j(t)}{P_j^{max}} \qquad (8)$$

$$rr^{TM} \leq 0.05,\ rr^{PG} \leq 0.20 \qquad (9)$$
$$maximum\ LFC\ ramp\ rate\ \ constraint$$

$$LFC(t) = \sum_{i=1}^{I} \sum_{n=1}^{N_i} P^{TM,max}_{i,n}\, rr^{TM}_{i,n}(t) + \sum_{j=1}^{J} \sum_{m=1}^{M_j} P^{PG,max}_{j,m}\, rr^{PG}_{j,m}(t) \qquad (10)$$

$$LFC(t) \geq Req_{LFC}(t) \qquad (11)$$

Thermal machines are summed over I fuel types and N_i generators per fuel type and pumped hydro generators are summed over J reservoirs with M_j pumps per reservoir. The superscript *max* refers to the maximum capacity of that generator. In the traditional model, the required secondary (LFC) reserve capacity $Req_{LFC}(t)$ is

$$Req_{LFC}(t) = max\{De(t) * 0.02, PV_f(t) * PV_{cap} * PV_r(t) * 0.10\} \quad (12)$$

is the maximum of either (a) 2% of demand or (b) 10% of forecasted solar PV generation at time t in hours, where $PV_f(t)$ is the forecasted normalized insolation and $PV_r(t)$ is the curtailment factor (1 = no curtailment, 0=night time).

$$0 \leq PV_f(t) \leq 1 \quad (13)$$

$$0 \leq PV_r(t) \leq 1 \quad (14)$$

2.2 UPDATED MODEL

The objective of this report is to investigate a more economical allocation between secondary and tertiary reserve capacities in order to reduce PV curtailment and decrease the total cost of dispatching the system.

2.2.1 PV CURTAILMENT OPERATION

The model described in section (2.1) uses PV curtailment data from the UC forecasts to determine the curtailment plan for the entire day. The EDC model is not able to change curtailment level as it updates with more precise data. This was a realistic assumption when a large number of solar farms in Japan could not be operated remotely and required an engineer to manually set the curtailment at each facility [1]. With newer power electronics, we are making the assumption that PV can be curtailed in real time. Therefore, the EDC model will no longer receive curtailment data from UC and will be able to curtail PV in real time. Due to the zero marginal cost of PV power, the optimization model will always choose to deploy maximum PV power in accordance with other constraints.

The ability to curtail PV dynamically provides additional *downward* flexibility in the power system and acts as an unofficial down reserve capacity. As will be summarized in later sections, only power shortages were discovered in the simulations.

2.2.2 TERTIARY RESERVE CAPACITY CONSTRAINTS

In our model, the purpose of tertiary reserve capacity is to accommodate PV forecast errors between the day before forecast and the actual day. In order to better model the maximum realistic forecast error, the statistical 5% ($PV_{fu}(t)$) and 95% ($PV_{fl}(t)$) confidence interval (CI) data was obtained, which was compared to the 50% CI data (forecast value $PV_f(t)$). The updated tertiary reserve capacity requirement can be expressed as

$$\sum_j P_u^{TM}(t) + \sum_g P_u^{PG}(t) \geq De(t) * 0.05 + (PV_f(t) - PV_{fl}(t)) * PV_{cap} * PV_r(t) \quad (15)$$

$$\sum_j P_d^{TM}(t) + \sum_g P_d^{PG}(t) \geq De(t) * 0.05 + (PV_{fu}(t) - PV_f(t)) * PV_{cap} * PV_r(t) \quad (16)$$

Since $PV_f(t) \geq PV_{fl}(t)$ and $PV_{fu}(t) \geq PV_f(t)$, this change *increases* the minimum constraint, which is needed during times of high PV forecast errors, increasing the overall cost of dispatching the system. This change ensures that the maximum *realistic* PV forecast errors are accounted for on each day in the UC simulation.

2.2.3 SECONDARY (LFC) RESERVE CAPACITY

In our model, the purpose of secondary (LFC) reserve is to accommodate high frequency fluctuations in residual load. In order to determine trends, the demand data and solar PV generation data for one year was analyzed. In order to strictly determine the high frequency fluctuations every hour, the data was passed through a high pass filter to discard any periodic components with a time period higher than 32 minutes using the “highpass” function in MATLAB’s signal processing toolbox. Unless otherwise stated, the data was time filtered to only include data points between the hours of 8:00 and 16:00 (daylight hours). The fluctuation data (solar PV fluctuations, residual load fluctuations, and demand fluctuations) was created by calculating the maximum fluctuations in the high frequency filtered data in every 20 minute period.

$$max, fluctuation(t) = max\{data(t), data(t+1),... + data(t+19)\} - min\{data(t), data(t+1),... + data(t+19)\} \quad (17)$$

Where data(t) is either solar PV, residual load, or demand data at t min. The maximum fluctuation every hour was taken to create a data set of maximum *hourly* fluctuation. Figure 2 shows the relationship between the low and high frequencies of a 3 day PV output curve.

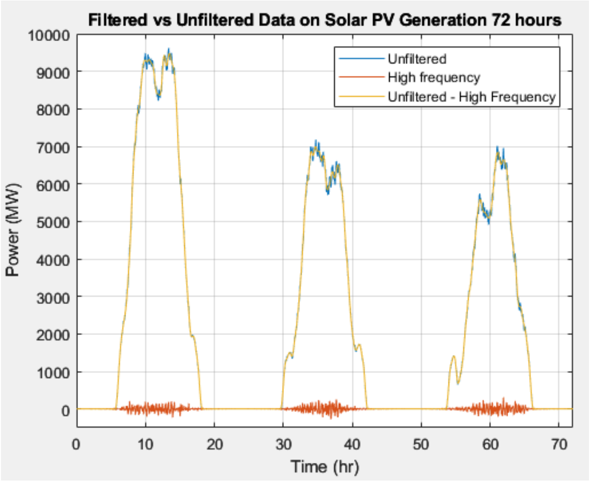

Fig. 2 - Solar PV data showing unfiltered and filtered components over a 72 hr period

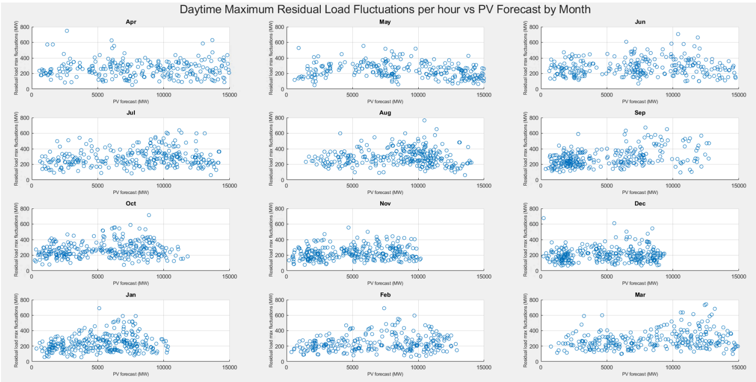

Fig. 3 - Daytime maximum residual load fluctuations per hour vs PV forecast per month

Figure 3 shows the maximum hourly residual load fluctuations as a function of PV forecast, divided by each month of the year. There is a *small* trend that fluctuations tend to be smaller when PV forecasts are high. This makes sense since PV forecasts are high during sunny, cloudless days - which do not have high frequency fluctuations. Furthermore, the new EDC PV curtailment strategy provides additional flexibility to reserves, allowing us to be more conservative during times of high PV output (midday). The effect of only demand fluctuations have not been considered.

The PV output of a typical day is divided into two sections - the ramp A (morning and evening), and the peak B (midday) as shown in figure 4.

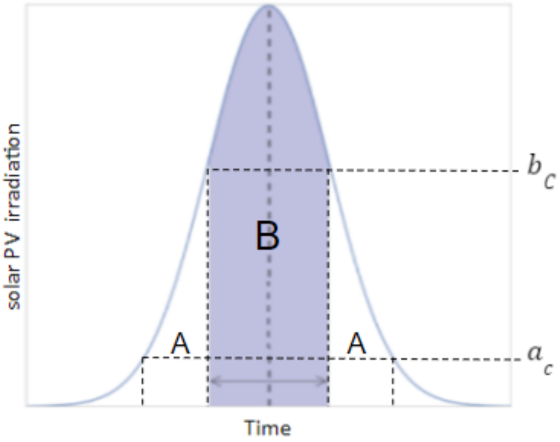

Fig. 4 - Solar insolation curve of a typical day highlighting peak areas to redefine secondary reserve constraints

The required secondary (LFC) reserve capacity $LFC(t)$ will depend on the value of curtailed PV forecast in the UC calculation (note that UC and EDC models *independently* calculate required PV curtailment).

Condition (i)

$$if\ a_c \leq PV_f(t) * PV_{cap} * PV_r(t) \leq b_c \qquad (18)$$

$$\Rightarrow LFC(t) \geq PV_f(t) * PV_{cap} * 0.10 \qquad (19)$$

Condition (ii)

$$if\ PV_f(t) * PV_{cap} * PV_r(t) > b_c \qquad (20)$$

$$\Rightarrow LFC(t) \geq - PV_f(t) * PV_{cap} * 0.10 + \alpha \qquad (21)$$

Condition (iii)

$$LFC(t) \geq De(t) * 0.02\ \forall t \qquad (22)$$

Condition (iii) has no conditional assignment and therefore always ensures that the secondary (LFC) reserve capacity is set at a *minimum* of 2% of demand. Conditions (i) and (iii) are similar to the original constraints described in equation (12).

Condition (ii) tends to (depending on the value of α) decrease the required reserve capacity in region B. Experimentally, if α is large(≥ 1900), it does not reduce the required constraint. Therefore, this report focuses on the effect of different α values to LFC(t) requirements, PV curtailment, and system operating costs.

The cutoff between sections A and B are determined by the intersection of the equations in conditions (i) and (ii),

$$PV_f(t) * PV_{cap} * 0.10 = \qquad (23)$$

$$- PV_f(t) * PV_{cap} * 0.10 + \alpha$$

$$\Rightarrow b_c * 0.10 =- b_c * 0.10 + \alpha \qquad (24)$$

$$\Rightarrow b_c = \frac{\alpha}{0.20} MW \qquad (25)$$

And

$$a_c = 2000\, MW \qquad (26)$$

Note that the new constraints *do not* include PV curtailment $PV_r(t)$ that was included in the previous model. The binary variables needed to implement the conditional constraints are not compatible with being multiplied with another decision variable $PV_r(t)$. This is a limitation of the GAMS optimization software when solving mixed integer linear programming (MILP) optimization problems. GAMS does not allow conditional *if* statements within its equation definitions, which necessitates the use of the "big M" method using the simplex algorithm.

2.3 SIMULATIONS

1 year simulations were run for for the following situations:

a) Original model - no PV curtailment in EDC, original secondary (LFC) reserve constraints
b) Same as (a), but with updated EDC PV curtailment
c) Same as (b), but with updated LFC reserve constraints:
    i) $\alpha = 1900,\ b_c = 9500$
    ii) $\alpha = 1800,\ b_c = 9000$
    iii) $\alpha = 1700,\ b_c = 8500$
    iv) $\alpha = 1600,\ b_c = 8000$
    v) $\alpha = 1500,\ b_c = 7500$
    vi) $\alpha = 1400,\ b_c = 7000$

As described in a previous section, a C script runs the GAMS' optimization model sequentially - first the UC model, which transmits its generator commitment data to the EDC as well as to the next day's UC calculation (to ensure continuity in the operation of the generators and enforce start / stop and ramp limit constraints). Therefore, each day of the year calls the two optimization models, leading to a computational time of 5-6 hours per 1 year simulation. Figure 5 graphically depicts the algorithm's function.

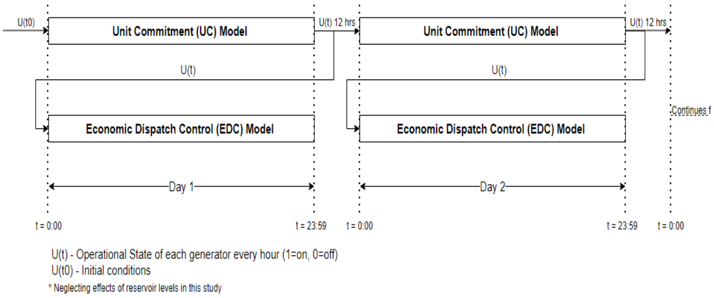

Fig. 5 - Schematic representation of each GAMS optimization algorithm

In all the above simulations, the tertiary reserve capacity found in equations (15) and (16) were used. Therefore, a comparison can be made between different EDC optimization techniques and secondary (LFC) reserve capacity constraint adjustments as only a single aspect of the model was changed between simulations.

3.0 RESULTS AND DISCUSSIONS

After running the simulations in GAMS, the results were compiled, analyzed, and plotted using Matlab. The following subsections provide an overview of the secondary (LFC) reserve capacity, PV curtailment, and operating costs of the system. No shortages or surpluses were recorded in any of the simulations; the Chubu power system was able to fulfill its power demand without exchanging power between neighboring regions.

3.1 SECONDARY (LFC) RESERVE CAPACITY FOR DIFFERENT SIMULATIONS

Figure 6 shows the daily mean secondary (LFC) reserve capacity allocated each month. Since reserve capacity depends strongly on solar PV

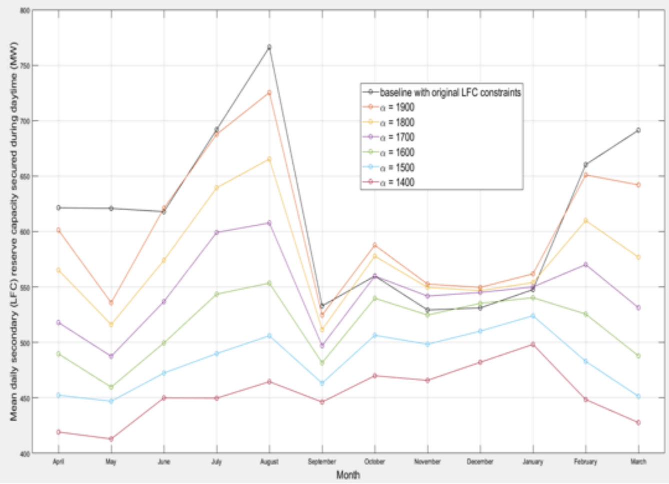

Fig. 6 - Mean daily secondary (LFC) reserve capacity allocated per month for different values

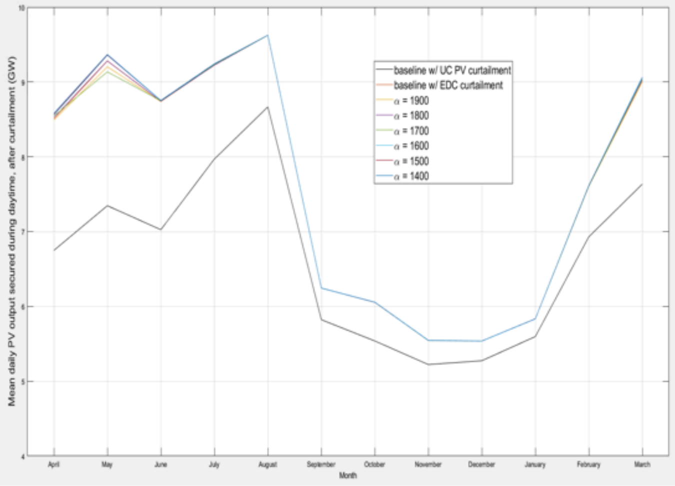

Fig. 7 - Mean daily solar PV output each month for different simulations

output, it increases in the hotter months (July, August, March) and reduces in the colder winter months (November, December, January). As expected, the LFC reserve reduces as we decrease α, which is evident from the figure. In the colder months, the baseline (original constraints) produce a lower (and hence more economical) reserve capacity compared to $\alpha = 1900, 1800, 1700$. This is possibly because, at higher α values, the original constraints are *more* restrictive, particularly when the average PV output is lower.

For the most part, the actual secondary reserve capacity is close to the minimum required constraint, since that is usually where the optimization function finds the objective function (costs) minima.

3.2 SOLAR PV CURTAILMENTS FOR DIFFERENT SIMULATIONS

Figure 7 shows the actual daily mean PV output each month. The general shape is similar to the secondary reserves obtained in the previous section, though the spread between different α values is not significant, particularly at the chosen scale of the graph (except in the month of May).

There are large differences in average PV output between the baseline case (with UC PV curtailment) and the cases which include EDC PV curtailment. This makes it clear that dynamic adjustments of PV curtailment in real time to adjust the supply / demand balance helps reduce PV curtailments significantly. Since the marginal cost of solar PV power is zero, every MW of solar PV curtailed results in increased costs since a fossil fuel generator will need to cover that deficit (except in the case of hydroelectric energy).

3.3 SYSTEM OPERATING COSTS IN DIFFERENT SIMULATIONS

Figure 8 shows the total costs per month for each of the simulations. Due to the benefit of lower solar PV curtailments, the simulations that include EDC PV curtailments (all except the baseline w/ UC PV curtailment) show a significantly lower dispatching cost each month. Figure 9 is a magnified view of the same graph to highlight that the costs do decrease as the value of α decreases.

The cost savings compared to the baseline case (UC PV curtailment, original constraints) are shown in figure 10. From the figure, the $\alpha = 1900$ simulation shows a similar cost savings compared to the simulation without the revised secondary reserve constraints. However, as we decrease α, there appears to be a linear increase in savings.

Figure 11 shows the relationship between α and savings and applies a linear fit to the data. As summarized, as α increases, the savings *decrease.* In theory, we should be able to further reduce α below 1400. However, the simulations showed power shortages during some days which were considered unacceptable in this report. Since PV curtailment is always an option, there was not a power surplus in the year since the GAMS model was free to curtail PV as much as needed to accommodate. Therefore, this flexibility provided an unofficial down reserve benefit to the system. Table 2 summarizes the cost

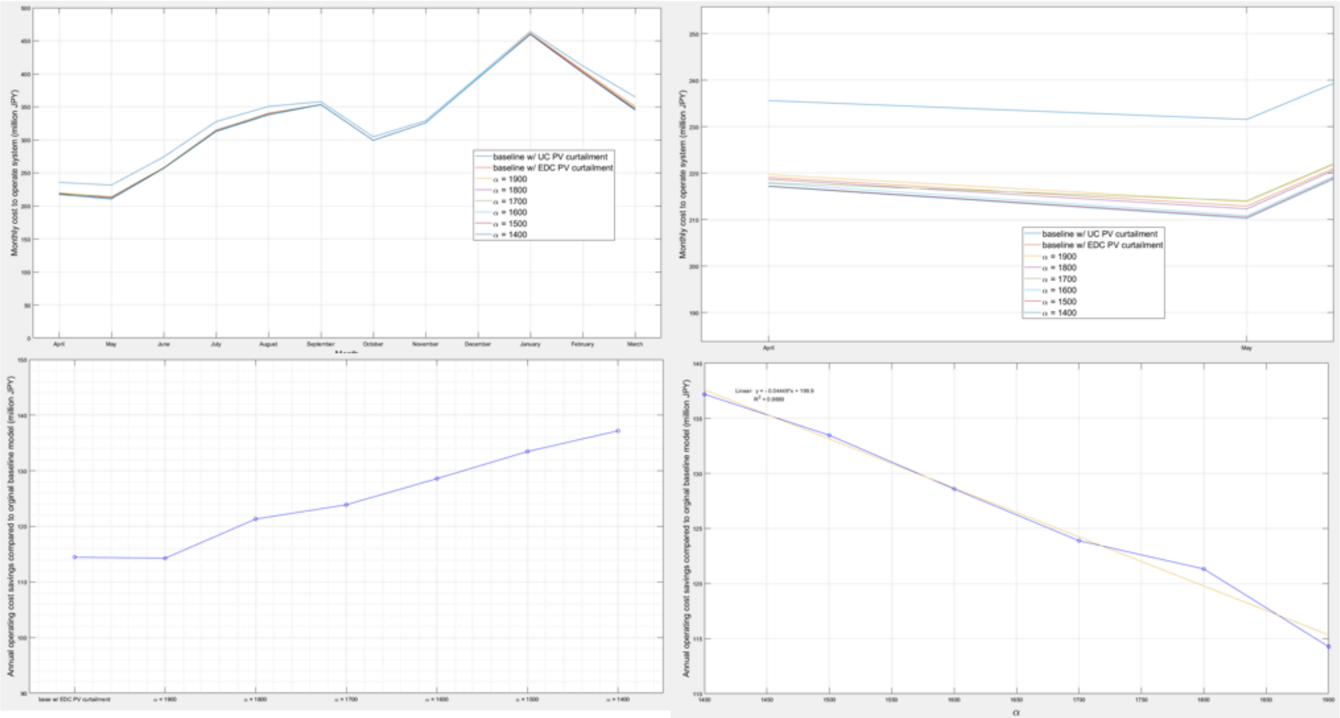

From top left and moving clockwise: Fig. 8 - Monthly System Operating Costs for each simulation, Fig. 9 - Magnified view of April and May of figure 8 highlighting differences between simulations , Fig. 10 - Annual cost savings of each simulation of the updated model compared to original model, Fig. 11 - Linear relationship between α and cost savings

savings for each simulation compared to the original base case.

$$AnnualCost_{base\ w/\ UC\ PV\ curtailment} = 4,048\ million\ JPY \qquad (27)$$

Table 2 - Summary of cost savings for each simulation compared to original model

Simulation	Savings (million JPY)	Savings (%)
Baseline w/ EDC PV curtailment	114.45	2.82 %
α = 1900	114.27	2.82 %
α = 1800	121.32	3.00 %
α = 1700	123.89	3.06 %
α = 1600	128.58	3.18 %
α = 1500	133.46	3.30 %
α = 1400	137.18	3.39 %

4.0 CONCLUSIONS AND FUTURE WORK

This report analyzes the electric power system in Chubu region, Japan, in the year 2030. Due to Japan’s commitment to decarbonize its electric generation, the amount of renewable energy sources are expected to increase rapidly. Solar PV was considered along with all traditional generators (nuclear, hydro, coal, natural gas, oil, pumped hydro) to analyze methods to reduce solar PV curtailment and lower operating costs.

The optimization analysis conducted in GAMS for different simulations show that there are cost saving benefits to creating more robust secondary (LFC) reserve capacity constraints. Furthermore, curtailment of PV output in real time allows the system more flexibility in balancing supply and demand and maintaining nominal frequency.

The major findings of this report are that if PV curtailment was determined in real time (as opposed to the day before), the system obtains a large increase in flexibility, significantly reducing PV curtailments and operating costs. For the most conservative successful simulation, a 137.18 million JPY annual savings was calculated.

Prior to implementation, further research is needed. The models need to be tuned to include wind energy, demand error, and PV curtailment ramp limitations. A thorough security analysis is also needed to ensure that the system can handle contingencies - natural disasters like earthquakes and tsunamis are a common occurrence in Japan [8]. This report uses an optimization model that only considers economic dispatch of the system without consideration of the physics of power flow in the Chubu area. The next step would be to incorporate power flow related constraints to create an optimal power flow (OPF) model which will be more realistic and accurate.

ACKNOWLEDGEMENTS

I would like to thank the JUACEP program for this research opportunity at Nagoya University. Special thanks to Kato sensei, Urabe sensei, Atsumi san, and all other members of Kato lab for their guidance and assistance throughout the project.

REFERENCES

[1] K. Ogimoto and H. Wani, “Making Renewables Work: Operational Practices and Future Challenges for Renewable Energy as a Major Power Source in Japan,” IEEE Power and Energy Magazine, Dec. 2020.

[2] “太陽光発電の基礎知識について - JPEA 太陽光発電協会,” *JPEA 太陽光発電協会 - Japan Photovoltaic Energy Association*, May 17, 2021. https://www.jpea.gr.jp/knowledge/about/ (accessed Aug. 5, 2024).

[3] S. Koohi-Kamali, V. V. Tyagi, N. A. Rahim, N. L. Panwar, and H. Mokhlis, “Emergence of energy storage technologies as the solution for reliable operation of smart power systems: A review,” *Renewable and Sustainable Energy Reviews*, vol. 25, pp. 135–165, Sep. 2013, doi: 10.1016/j.rser.2013.03.056.

[4] *FY2022 energy supply and demand report (revised report)*. (n.d.). Retrieved July 10, 2024, from https://www.meti.go.jp/english/press/2024/0412_003.html

[5] N. Harag, C. T. Urabe, and T. Kato, “Optimal Allocation of Curtailment Levels of PV Power Output in Different Regions in Consideration of Reduction of Aggregated Fluctuations,” IEEE Xplore, Jul. 17, 2023. https://ieeexplore.ieee.org/document/10185041/ (accessed Jun. 10, 2024).

Development of a Novel Haptic System Using a 3D Vibration Motor

Yukteshwar Ravi [1],Izuru Naito [2], Tsuyoshi Inoue[3], Akira Heya[4]

[1] Department of Mechatronics and Robotics, New York University ,New York ,USA

[2] Department of Mechanical Engineering ,Nagoya University ,Nagoya ,Japan

[3] Department of Mechanical Engineering ,Nagoya University ,Nagoya ,Japan

[4] Department of Mechanical Engineering ,Nagoya University ,Nagoya ,Japan

Abstract— ***The demand for immersive virtual reality (VR) experiences has driven the development of advanced haptic feedback systems. Traditional 2D haptic feedback technologies have limitations in providing realistic, multi-directional sensations, leading to the need for more advanced solutions. This paper presents the development of a novel haptic system using a 3D vibration motor, called the XReactor. The XReactor is compact, lightweight, and capable of generating precise 3D feedback in real-time. Through experimental verification in a VR environment, the system demonstrated its ability to deliver accurate, multi-directional haptic feedback, enhancing the realism and immersion of virtual experiences. The results show the potential of the XReactor to significantly improve haptic feedback technology, with future work focusing on optimization and broader applications.***

I. INTRODUCTION

1.1 Background

Haptic feedback technology has become increasingly important in enhancing user interaction, especially in virtual reality (VR) environments. Traditional haptic systems are limited to 2D feedback, which constrains the depth of interaction and realism in these applications. The evolution of VR and gaming calls for more advanced, immersive feedback systems capable of providing 3D sensations.

1.2 The Need for 3D Haptic Feedback

Current 2D haptic feedback systems are unable to simulate the full range of human touch sensations, leading to a demand for 3D haptic systems. Such systems would allow for realistic, multi-directional sensations, enhancing immersion in VR applications. This project introduces the XReactor, a novel haptic system that addresses this gap by providing accurate, multi-directional feedback in a compact form factor.

II. RELATED WORK

2.1.EXISTING TECHNOLOGIES

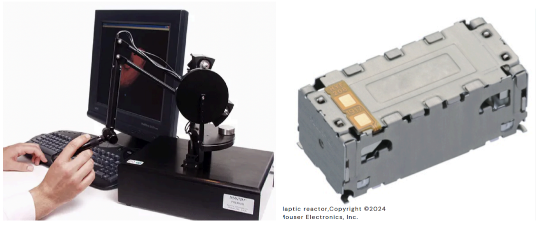

Fig 1. 3D Phamtom Premium & Haptic system
©1993-2012. Geomagic, Inc. All rights reserved. Produced inthe USA.

- **3D Systems Phantom Premium 1.5 High Force:** A sophisticated haptic system used in medical simulations and other specialized fields. While highly effective, its bulk and complexity make it unsuitable for consumer applications.

- **Traditional Haptic Reactors:** Widely used in gaming and mobile devices, these systems provide simple 2D vibrations. However, they lack the capability for realistic, multi-directional feedback needed for immersive experiences.

2.2.LIMITATIONS

Although these technologies are useful, they fail to provide the full range of realistic feedback needed in consumer VR applications. The XReactor seeks to fill this gap by offering 3D feedback in a portable and efficient form.

III. PROPOSED SYSTEM: THE XREACTOR

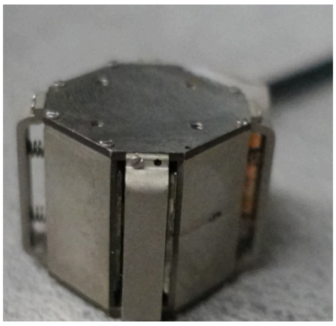

Fig 2.XReactor

3.1 Overview

The XReactor is a 3D vibration motor-based haptic system designed to overcome the limitations of traditional haptic devices. It generates precise feedback in the x, y, and z directions, creating realistic sensations for users in VR environments. Its compact and lightweight design makes it ideal for integration into consumer-grade VR systems.

3.2 Key Features

- **3D Vibration with a Single Unit:** Provides feedback in all three axes (x, y, z).
- **Compact and Lightweight Design:** Easily integrated into portable devices.
- **Powerful Vibrations:** Despite its small size, the XReactor can generate strong, precise vibrations that enhance the user experience.

IV. WHAT IS A 3D VIBRATION MOTOR?

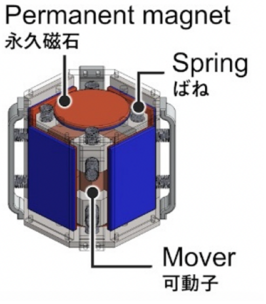

Fig 4:Structure

4.1 Technical Details

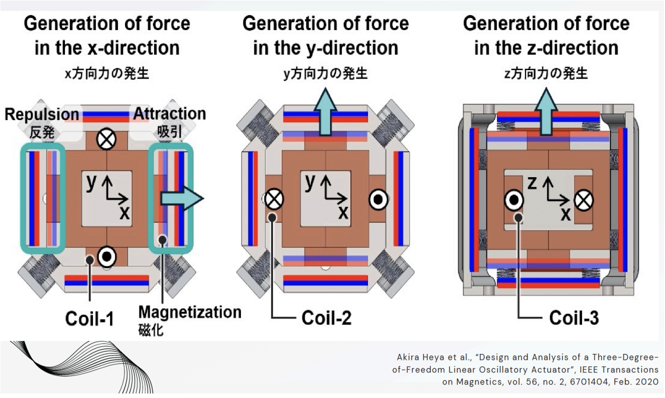

Akira Heya et al., "Design and Analysis of a Three-Degree-of-Freedom Linear Oscillatory Actuator", IEEE Transactions on Magnetics, vol. 56, no. 2, 6701404, Feb. 2020

Fig 5:Design % Analysis of a 3D linear Oscillatory Actuator

The 3D vibration motor used in the XReactor is based on the research of Akira Heya et al., involving a three-degree-of-freedom linear oscillatory actuator. This motor is capable of generating forces in the x, y, and z directions by controlling the movement of the internal mover through varying current in the motor's coils.

4.2 Operation

The motor's operation relies on precise control of the current passing through its coils, which manipulates the permanent magnets and generates directional forces. This allows the XReactor to produce 3D feedback, simulating the sensation of touch and movement in all directions.

V. SYSTEM CONFIGURATION

5.1 Components

A. ***Meta Quest 3:*** *Tracks hand movements in a virtual environment.*

B. ***Microcontroller and Motor Driver:*** *Controls the XReactor's output, translating user interactions into physical sensations.*

5.2 How it Works

In a VR environment, when a user interacts with an object (such as an arrow pointing in a particular direction), the system sends a signal to the microcontroller. This drives the XReactor to generate a corresponding sensation in the appropriate direction, simulating the physical force of the interaction. This process creates a pseudo-traction effect, enhancing the realism of the virtual experience.

VI. EXPERIMENTAL VERIFICATION

6.1 Testing Methodology

The XReactor was tested in a VR environment with arrows pointing in six directions: left, right, up, down, front, and back. The system was manually moved toward each arrow to measure its response.

6.2 Results

The XReactor successfully provided immediate, multi-directional feedback for all six directions, validating its ability to produce precise, real-time 3D haptic sensations. The experiments confirmed that the system enhances immersion in VR environments, performing consistently across all test scenarios.

VII. Discussion

7.1 System Performance

The XReactor demonstrated a significant improvement over traditional haptic systems by providing multi-directional feedback. The compact and efficient design makes it suitable for a range of VR and gaming applications.

7.2 Future Improvements

While the XReactor performed well in initial testing, there is room for optimization. Future work will focus on refining the motor design to make it even smaller and more energy-efficient. Additionally, exploring wearable applications could further expand the utility of the XReactor.

VIII. Conclusion

The XReactor successfully demonstrated its ability to provide accurate 3D haptic feedback in multiple directions, enhancing the realism and immersion of virtual environments. With further development, this system has the potential to revolutionize haptic feedback technology in consumer and professional applications.

References

1. Heya, A. et al. “Design and Analysis of a Three-Degree-of-Freedom Linear Oscillatory Actuator.” *IEEE Transactions on Magnetics*, vol. 56, no. 2, 2020.
2. Additional references can be added based on project details.

STATISTICAL TESTING ON GENERATIVE AI ANOMALY DETECTION TOOLS IN ALZHEIMER'S DISEASE DIAGNOSIS

Rosemary He

(Affiliation) Department of Computer Science, Graduate School of University of California, Los Angeles
Rosemary068@g.ucla.edu

Supervisor: Ichiro Takeuchi

(Affiliation) Graduate School of Engineering, Nagoya University
takeuchi.ichiro.n6@f.mail.nagoya-u.ac.jp

ABSTRACT

Alzheimer's Disease is challenging to diagnose due to our limited understanding of its mechanism and large heterogeneity among patients. Neurodegeneration is studied widely as a biomarker for clinical diagnosis, which can be measured from time series MRI progression. On the other hand, generative AI has shown promise in anomaly detection in medical imaging and used for tasks including tumor detection. However, testing the reliability of such data-driven methods is non-trivial due to the issue of "double dipping" in hypothesis testing. In this work, we propose to solve this issue with selective inference and develop a reliable generative AI method for Alzheimer's prediction. We show that compared to traditional statistical methods with highly inflated p-values, selective inference successfully controls the false discovery rate under the desired α level while retaining statistical power. In practice, our pipeline could assist clinicians in Alzheimer's diagnosis and early intervention.

1. INTRODUCTION

Alzheimer's disease (AD), the most prevalent cause of dementia, is difficult to diagnose due to our limited understanding of disease mechanism and interpersonal variability between symptoms and progression[1]. While AD can only be formally diagnosed through autopsy, alternative biomarkers are used to assess clinical diagnosis. There are three classes of potential biomarkers for AD: β-amyloid, tau and neurodegeneration or neuronal injury[1]. Compared to the first two classes, neurodegeneration can be measured noninvasively and observed in time series magnetic resonance (MR) images. On the other hand, deep learning approaches for medical diagnosis and classification have shown potential to outperform traditional statistical models[2]. In the field of medical imaging, generative AI (genAI) has been applied extensively for tasks including anomaly detection and disease classification[3]. However, the reliability of such data-driven methods remains questionable due to its black-box nature and the issue of "double dipping", where the hypothesis is selected and validated on the same dataset[4]. While traditional statistical methods follow the assumption that result statistics are inherently independent of the selection criteria under the null hypothesis[4], data-driven methods, including deep learning, break this assumption by using the same dataset for training and validation. As a result, statistical inference becomes invalid with a high false discovery rate (type I error).

1.1 Related Works

In medical imaging, pathology such as anomalous growth (tumors) or traumatic injury can be viewed as deviations from the norm. Therefore, quantifying such deviation can be used to separate true anomalous signal from noise in imaging, improving classification accuracy. The main approach for anomaly detection with brain MRIs are semi-supervised, where the model is trained on the set of healthy patients only[16]. During inference, the model estimates the "healthy" alternative of the diseased image, and anomaly analysis is performed on the reconstruction error between the ground truth and prediction. While most published applications of such methods on brain imaging focus explicitly on tumors (which is one image), we apply the same setting to study anomalous neurodegeneration rate in Alzheimer's patients (which is progressional and estimated using two images).

Hypothesis testing in data-driven methods including machine learning and deep learning often face the issue of "double dipping"[4], where the same data is used to formulate and validate the hypothesis. As traditional statistical testing follows the assumption that a hypothesis is predetermined and independent from the dataset, "double dipping" will lead to selection bias, resulting in a high false discovery rate (FDR) and an invalid test. Selective inference (SI) is a statistical framework that corrects such bias by considering a conditional test. Previously, the SI framework has been applied to assess deep learning methods for medical segmentation[23], saliency map[24], anomaly detection in VAE[6] and diffusion[25] models.

1.2 Contribution

In this work, we propose to apply selective inference, a statistical testing framework for data-driven hypothesis[5], [6], to assess the reliability of a genAI based anomaly detection tools for AD neurodegeneration progression. We first develop a conditional variational autoencoder (CVAE) model for anomaly detection in Alzheimer's cohort, then apply selective inference to test the significance of its predictions. While both tasks have been studied in their respective fields, we list two novel contributions of our work: 1. the first to apply selective inference to assess the validity of genAI based diagnosis tool in Alzheimer's, and 2. novel approach to study neurodegeneration rate via estimating optical flow from paired MRIs.

2. METHODS

2.1 Data Preparation

We obtain our dataset from the Alzheimer's Disease Neuroimaging Initiative (ADNI) database[7] and the Open Access Series of Imaging Studies (OASIS) database[8], [9]. ADNI (adni.loni.usc.edu) is led by Principal Investigator Michael W. Weiner, MD. The primary goal of ADNI is to measure the progression of mild cognitive impairment (MCI) and early Alzheimer's disease. First, we include subjects from ADNI 1, 2 and 3 studies, as well as OASIS-3 who have at least 2 MPRAGE scans available at least one year apart. For patients with more than 2 scans, we take the first and last scans as the pair. In recent deep learning applications, disease progression can be modeled as changing pixel values in time series medical images[10], [11], [12], [13]. Under this model, we propose to estimate the atrophy rate via optical estimation, i.e. by tracking pixel movement in the pair of images over an arbitrary amount of time[14], [15]. For each pair of images, we estimate the velocity of change for each pixel, where positive values (light pixels) indicate growth and negative values (dark pixels) indicate atrophy. Sample visualization of optical flow estimation is shown in Fig. 1, where growth in the ventricles (due to atrophy in surrounding white matter) is observed. We note here that though both the MRI and optical flow are 3D (80x80x80 pixels), we take the middle coronal slice (80x80 pixels) as 2D input into the model due to computational limitations. Lastly, we standardize the images across the cohort.

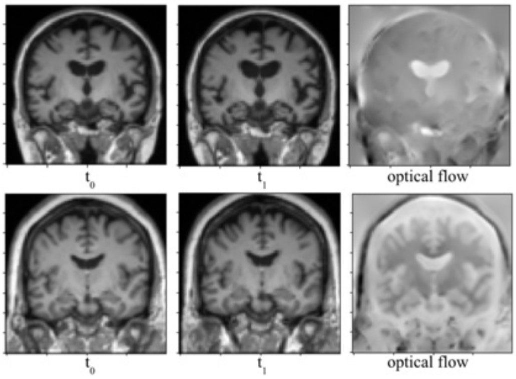

Fig. 1 sample visualization of optical flow estimation.

In addition to the images, we add two conditional variables to the model: age at the first scan and time difference between the pair of MRIs. We standardize both to have mean 0 and variance 1. For disease labels, we chose binary outputs for simplicity and group patients into healthy or diseased. We note here that ADNI groups patients into 6 categories: cognitive normal, subjective memory complaint, early mild cognitive impairment, mild cognitive impairment, late mild cognitive impairment and AD. Since OASIS and ADNI have different conventions for disease status, we keep consistency by grouping OASIS subjects into cognitive normal, cognitive impairment and AD, and assign them a value of 0, 3 and 5. To increase data quality, we take only the cognitive normal cohort as healthy, and late mild cognitive impairment (label of 5) and AD (label of 6) as diseased. After initial filtering and processing, the cohort consists of 888 healthy and 110 diseased individuals.

2.2 Anomaly Detection

2.2.1 Conditional variational autoencoder

In this section, we give a brief overview for those unfamiliar with autoencoder models and their extensions. Autoencoders are a class of deep learning methods that learn a low-dimensional representation of high-dimensional data such as medical imaging[17]. Autoencoders often follow a U-net[18] architecture, where an encoder projects high dimensional data down to a latent space with lower dimensions, and a decoder learns to map the latent space representation back to its original input. Though there is a latent space, autoencoders are deterministic as its latent distribution is unknown, making inference difficult and prompting the need for variational autoencoders (VAE)[19].

VAE models assume the following sample generation: a sample x is generated from a distribution conditioned on the latent space z, where z follows $p_\theta(z)$ and x follows $p_\theta(x|z)$. However, estimating the posterior distribution of x is intractable in practice. To address this issue, a more tractable distribution, $q_\Phi(z|x)$, is used to approximate the true posterior. VAEs can be trained to sample from unknown distributions using the variational lower bound of the log-likelihood, which can be written as follows[19]:

$$L(\theta, \Phi,x) = - D_{KL}(q_\Phi(z|x)|| p_\theta(z)) + E_{q\Phi(z|x)}[\log p_\theta(x|z)] \quad (1)$$

,where D_{KL} is the Kullback–Leibler divergence[20] that measures how similar two distributions are, and $E_{q\Phi(z|x)}$ measures the sum of squared reconstruction error where we assume $p_\theta(x|z)$ is Gaussian with mean predicted by the model and variance of 1. We use the common choice that $p_\theta(z)$ is multivariate standard normal, with no learnable parameters. Conditional VAE (CVAE) models are an extension to the VAE and include an additional variable y as the conditional variable[21]. While the mathematical framework remains the same, CVAEs are used widely in medical applications as conditional variables offer additional information and can improve parameter estimation.

2.2.2 Model architecture

To reduce computational time of selective inference testing, we construct a relatively simple CVAE as in Fig. 2. The encoder consists of 3 blocks, where each block contains one convolutional and one max pooling layer; the decoder consists of 3 blocks, one convolutional and one up-sampling layer with skip connections, as illustrated in grey in Fig. 2. As the selective inference procedure has high computational requirements, we keep the model relatively simple with a latent space size of 10 and 128 channels at the deepest.

2.2.3 Model training

Following a common training and inference scheme of anomaly detection, we train on healthy subjects only and keep all 110 AD subjects for selective inference later. Within 888 healthy subjects, we take 600 as the training set, 100 as the test set, 100 for selective inference and 88 for variance estimation used in selective inference. We split the subjects at random and train the model with the Adam optimizer[22], learning rate of 1e-5 and for 1000 epochs with early stopping.

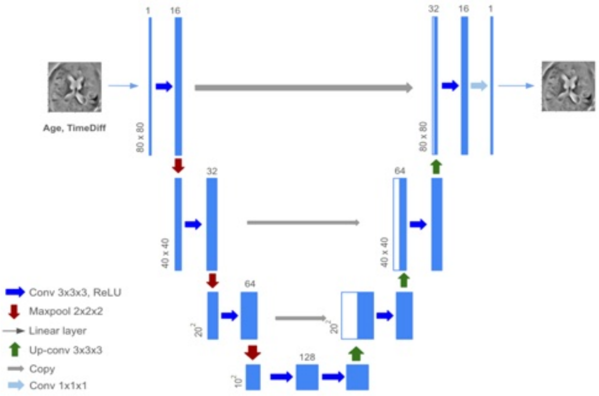

Fig. 2 Model architecture.

2.2.4 Anomaly detection pipeline

After the model is trained with only healthy subjects, we describe the steps for anomaly detection as follows:

1. Given the image of an Alzheimer's subject, the CVAE predicts the "healthy" alternative image
2. Take the difference between ground truth and prediction to find reconstruction error per pixel
3. Binarize the error by applying a threshold where a pixel X_i =1 if abs(X_i)>threshold and 0 otherwise
4. Obtain the anomaly mask

For the threshold, we take the 95th percentile of the reconstruction error for the healthy test set. To improve mask quality, we focus on the ventricle regions only.

2.3 Selective Inference

2.3.1 Statistical test

Here we follow the same set-up to assess our CVAE model as [6]. Let an optical flow image X be described as a n-dimensional vector,

$$X=(X_1,X_2,\ldots X_n) = \mathbf{s}+\boldsymbol{\varepsilon},\ \boldsymbol{\varepsilon}\sim N(\mathbf{0}, \Sigma) \quad (2)$$

, such that $\mathbf{s}\in R^n$ represents the vector of true signals and $\boldsymbol{\varepsilon}\in R^n$ is the noise following normal distribution. Let the CVAE anomaly detection pipeline be represented as a black-box function A such that

$$A: R^n \ni X \mapsto A_X \in 2^{[n]} \quad (3)$$

, where $2^{[n]}$ is the power set of [n] and A_X is the anomaly mask obtained by steps in 2.2.4.

To quantify the reliability of detected anomaly regions, we test the difference between the true signal of pixels in the abnormal region $\{s_i\}_{i\in A_X}$ and normal region $\{s_i\}_{i\in A^c_X}$, where

A^c_X is the complement to the anomaly region. We define the null and alternative hypothesis as:

$$\begin{aligned} H_0&: \frac{1}{|A_{\boldsymbol{X}}|}\sum_{i\in A_{\boldsymbol{X}}} s_i = \frac{1}{|A^c_{\boldsymbol{X}}|}\sum_{i\in A^c_{\boldsymbol{X}}} s_i \\ H_1&: \frac{1}{|A_{\boldsymbol{X}}|}\sum_{i\in A_{\boldsymbol{X}}} s_i \neq \frac{1}{|A^c_{\boldsymbol{X}}|}\sum_{i\in A^c_{\boldsymbol{X}}} s_i \end{aligned} \quad (4)$$

, and the test statistics T(X) as

$$T(\boldsymbol{X}) = \frac{1}{|A_{\boldsymbol{X}}|}\sum_{i\in A_{\boldsymbol{X}}} X_i - \frac{1}{|A^c_{\boldsymbol{X}}|}\sum_{i\in A^c_{\boldsymbol{X}}} X_i = \boldsymbol{\eta}^\top \boldsymbol{X} \quad (5)$$

$$\boldsymbol{\eta} = \frac{1}{|A_{\boldsymbol{X}}|}\mathbf{1}_{A_{\boldsymbol{X}}} - \frac{1}{|A^c_{\boldsymbol{X}}|}\mathbf{1}_{A^c_{\boldsymbol{X}}} \quad (6)$$

In the naïve setting, the p-value can be calculated as

$$P_{naive} = P_{null}(|T(X)| \geq T(x)|) \quad (7)$$

, where X is a random vector and x is the observed image. Under this assumption, P_{naive} can be calculated from the normal distribution $T(X)\sim N(0, \eta^T \Sigma\eta)$. However, it does not consider the fact that the anomaly region obtained is dependent on each input, resulting in a high false positive rate and rendering the test invalid[6]. On the other hand, SI calculates the p-value of T(X) conditional on the observation, i.e. $T(X)|\{A_X=A_x\}$. By conditioning on the hypothesis selection event, SI considers the rarity of observation from the subset of hypothesis in which an abnormal region is detected instead of the entire space. For details on calculating the statistics, we follow the same procedure as in [6] and use the SI package from [26].

3. RESULTS

First, we show the validity of SI under this setting by constructing a dataset with 1000 random noise images. Under the null hypothesis, the p-values of a valid test follows a uniform distribution, as seen in Fig. 3. The naïve p-values are heavily skewed to the left while the p-values from SI (selective p-value) are uniformly distributed as expected.

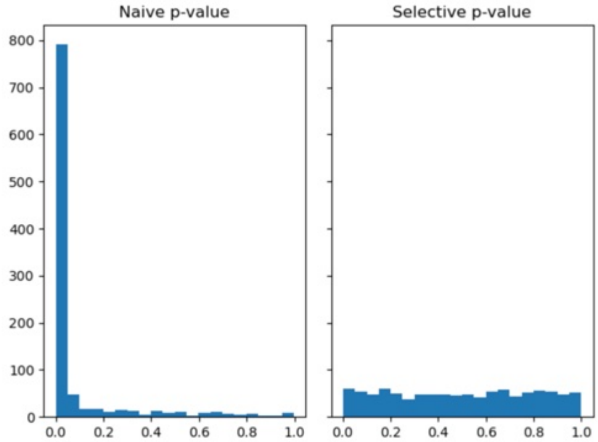

Fig. 3 p-value distribution under the null.

In addition to the naïve p-value, we calculate the adjusted p-values under the Bonferroni correction[27] as an alternative method for multiple testing. In Table 1, we compare the false discovery rate between the naïve, Bonferroni and SI, where the naïve and Bonferroni p-values are calculated using α=0.05 and SI values are calculated using α=[0.01, 0.05, 0.1]. As expected, the naïve method has a very high false discovery rate while Bonferroni has the lowest. We note here that SI controls the FDR well around the desired α at three different thresholds. In Table 2, we compare the power between the methods. We note power for the naïve method is not meaningful due to the high FDR. SI outperforms Bonferroni by a large margin and as α increases, the power of SI increases as expected from the FDR-power trade-off. We note here that SI's power is still not ideal, we suspect the input data may not provide a strong enough signal and will be a next step for this work.

Table 1. FDR comparison between methods

Held-out normal	Reject the null	Failed to reject	FDR
Naïve	74	26	0.74
Bonferroni	0	100	0
SI [α=0.05]	6	94	0.06
SI [α=0.01]	2	98	0.02
SI [α=0.1]	10	90	0.1

Table 2. Power comparison between methods

Alzheimer's cohort	Reject the null	Failed to reject	FDR
Naïve	93	17	0.85
Bonferroni	7	103	0.06
SI [α=0.05]	36	74	0.33
SI [α=0.01]	12	98	0.11
SI [α=0.1]	51	59	0.46

Lastly, we include some sample cases for visualization and comparison between the naïve and SI p-values in Fig. 4. For the extreme case where there is little to no anomaly detected, both the naïve and SI failed to reject the null. On the other hand, when there are large amounts of signals, both methods correctly identify the anomaly case of Alzheimer's. For cases in the middle, however, the naïve method overestimates the anomaly and the SI method underestimates the anomaly, which can be reflected by the high FDR of naïve and low power of SI.

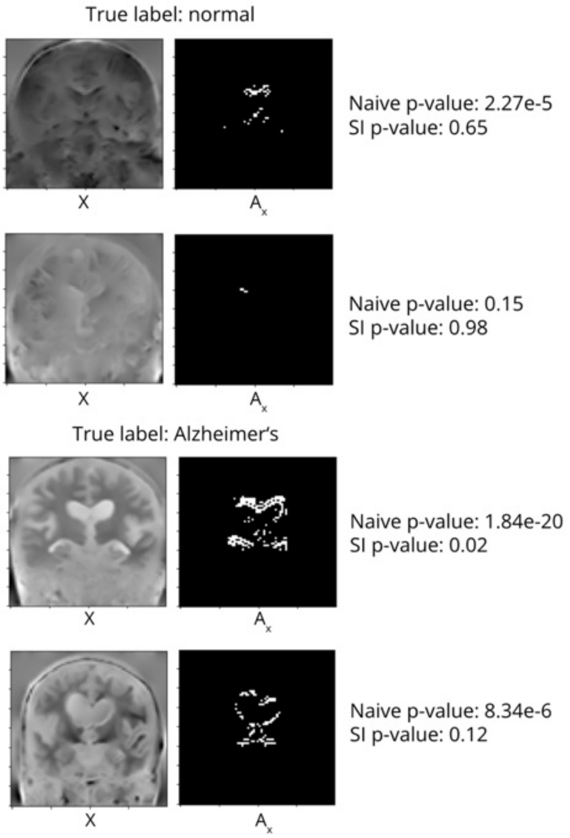

Fig. 4 Sample visualization and p-values.

4. DISCUSSION

In this work, we applied the selective inference framework onto anomaly detection for neurodegeneration in Alzheimer's patients to develop a reliable method for disease prediction. We show that selective inference controls the FDR well under three different α thresholds when the traditional hypothesis test fails. In addition, we show that compared to the more conservative Bonferroni method, SI has more power in detecting true anomalies, though SI's power should to be further improved upon for practical utilization. We suspect a few things could be done to improve the power. First, the dataset can be further improved and cleaned. Optical flow[14] estimates pixel change well over the short period of time, but does not work well for longer time elapses. For some patients, the time difference between MRIs could be on the magnitude of years and optical flow does not track this change well and does not provide enough signals. As alternative options for estimating the atrophy rate between pairs of images are explored, a better dataset could lead to better results. Secondly, hyperparameter choices can impact SI results. Finding a more appropriate anomaly threshold, instead of using the 95th percentile of the normal reconstruction error from the healthy test set, may help improve SI's power. Lastly, we took a 2D slice from a 3D image due to computational limitations, but in doing so greatly reduces the amount of information provided. An extension of the pipeline from 2D to 3D will incorporate more morphological changes in the brain and can potentially improve results. Another limitation of this work is that only two standard methods were compared, alternative solutions to double dipping such as data thinning[28] were not included. While all limitations listed above are also future directions of this work, this work provides an additional tool for anomaly detection using generative AI that can be statistically quantified reliability with just one dataset. As genAI tools face challenges including interpretability and reliability issues with integration into clinical practice, we hope this work serves as a starting point where more robust methods could be built upon for trustworthy AI-assisted clinical care.

ACKNOWLEDGEMENTS

This work is supported by the Japan Student Services Organization (JASSO) scholarship and Nagoya University JUACEP program.

REFERENCES

[1] C. R. Jack *et al.*, "A/T/N: An unbiased descriptive classification scheme for Alzheimer disease biomarkers," *Neurology*, vol. 87, no. 5, pp. 539–547, Aug. 2016, doi: 10.1212/WNL.0000000000002923.

[2] M. Bakator and D. Radosav, "Deep Learning and Medical Diagnosis: A Review of Literature," *Multimodal Technol. Interact.*, vol. 2, no. 3, Art. no. 3, Sep. 2018, doi: 10.3390/mti2030047.

[3] R. Y. He *et al.*, "Generative AI models in time varying biomedical data: a systematic review (Preprint)," Apr. 30, 2024. doi: 10.2196/preprints.59792.

[4] N. Kriegeskorte, W. K. Simmons, P. S. F. Bellgowan, and C. I. Baker, "Circular analysis in systems neuroscience: the dangers of double dipping," *Nat. Neurosci.*, vol. 12, no. 5, pp. 535–540, May 2009, doi: 10.1038/nn.2303.

[5] J. Taylor and R. J. Tibshirani, "Statistical learning and selective inference," *Proc. Natl. Acad. Sci.*, vol. 112, no. 25, pp. 7629–7634, Jun. 2015, doi: 10.1073/pnas.1507583112.

[6] D. Miwa, T. Shiraishi, V. N. L. Duy, T. Katsuoka, and I. Takeuchi, "Statistical Test for Anomaly Detections by Variational Auto-Encoders," Jun. 02, 2024, *arXiv*: arXiv:2402.03724. doi: 10.48550/arXiv.2402.03724.

[7] C. R. Jack Jr. *et al.*, "The Alzheimer's disease neuroimaging initiative (ADNI): MRI methods," *J. Magn. Reson. Imaging*, vol. 27, no. 4, pp. 685–691, 2008, doi: 10.1002/jmri.21049.

[8] D. S. Marcus, T. H. Wang, J. Parker, J. G. Csernansky, J. C. Morris, and R. L. Buckner, "Open Access Series of Imaging Studies (OASIS): Cross-sectional MRI Data in Young, Middle Aged, Nondemented, and Demented Older Adults," *J. Cogn. Neurosci.*, vol. 19, no. 9, pp. 1498–1507, Sep. 2007, doi: 10.1162/jocn.2007.19.9.1498.

[9] P. J. LaMontagne *et al.*, "OASIS-3: Longitudinal Neuroimaging, Clinical, and Cognitive Dataset for

Normal Aging and Alzheimer Disease," Dec. 15, 2019, *medRxiv*. doi: 10.1101/2019.12.13.19014902.

[10] J. S. Yoon, C. Zhang, H.-I. Suk, J. Guo, and X. Li, "SADM: Sequence-Aware Diffusion Model for Longitudinal Medical Image Generation," in *Information Processing in Medical Imaging*, A. Frangi, M. de Bruijne, D. Wassermann, and N. Navab, Eds., Cham: Springer Nature Switzerland, 2023, pp. 388–400. doi: 10.1007/978-3-031-34048-2_30.

[11] Q. Zhao, E. Adeli, N. Honnorat, T. Leng, and K. M. Pohl, "Variational AutoEncoder for Regression: Application to Brain Aging Analysis," in *Medical Image Computing and Computer Assisted Intervention – MICCAI 2019*, D. Shen, T. Liu, T. M. Peters, L. H. Staib, C. Essert, S. Zhou, P.-T. Yap, and A. Khan, Eds., Cham: Springer International Publishing, 2019, pp. 823–831. doi: 10.1007/978-3-030-32245-8_91.

[12] T. Xia, A. Chartsias, and S. A. Tsaftaris, "Consistent Brain Ageing Synthesis," in *Medical Image Computing and Computer Assisted Intervention – MICCAI 2019*, D. Shen, T. Liu, T. M. Peters, L. H. Staib, C. Essert, S. Zhou, P.-T. Yap, and A. Khan, Eds., Cham: Springer International Publishing, 2019, pp. 750–758. doi: 10.1007/978-3-030-32251-9_82.

[13] R. He, G. Ang, and D. Tward, "Individualized multi-horizon MRI trajectory prediction for Alzheimer's Disease," Aug. 04, 2024, *arXiv*: arXiv:2408.02018. doi: 10.48550/arXiv.2408.02018.

[14] B. K. P. Horn and B. G. Schunck, "Determining optical flow," *Artif. Intell.*, vol. 17, no. 1, pp. 185–203, Aug. 1981, doi: 10.1016/0004-3702(81)90024-2.

[15] "The computation of optical flow | ACM Computing Surveys." Accessed: Aug. 27, 2024. [Online]. Available: https://dl.acm.org/doi/abs/10.1145/212094.212141

[16] M. E. Tschuchnig and M. Gadermayr, "Anomaly Detection in Medical Imaging - A Mini Review," in *Data Science – Analytics and Applications*, P. Haber, T. J. Lampoltshammer, H. Leopold, and M. Mayr, Eds., Wiesbaden: Springer Fachmedien, 2022, pp. 33–38. doi: 10.1007/978-3-658-36295-9_5.

[17] J. Ehrhardt and M. Wilms, "Chapter 8 - Autoencoders and variational autoencoders in medical image analysis," in *Biomedical Image Synthesis and Simulation*, N. Burgos and D. Svoboda, Eds., in The MICCAI Society book Series. , Academic Press, 2022, pp. 129–162. doi: 10.1016/B978-0-12-824349-7.00015-3.

[18] O. Ronneberger, P. Fischer, and T. Brox, "U-Net: Convolutional Networks for Biomedical Image Segmentation," May 18, 2015, *arXiv*: arXiv:1505.04597. doi: 10.48550/arXiv.1505.04597.

[19] D. P. Kingma and M. Welling, "Auto-Encoding Variational Bayes," arXiv.org. Accessed: Mar. 11, 2024. [Online]. Available: https://arxiv.org/abs/1312.6114v11

[20] S. Kullback and R. A. Leibler, "On Information and Sufficiency," *Ann. Math. Stat.*, vol. 22, no. 1, pp. 79–86, 1951.

[21] K. Sohn, H. Lee, and X. Yan, "Learning Structured Output Representation using Deep Conditional Generative Models," in *Advances in Neural Information Processing Systems*, Curran Associates, Inc., 2015. Accessed: Mar. 11, 2024. [Online]. Available: https://proceedings.neurips.cc/paper_files/paper/2015/hash/8d55a249e6baa5c06772297520da2051-Abstract.html

[22] D. P. Kingma and J. Ba, "Adam: A Method for Stochastic Optimization," Jan. 29, 2017, *arXiv*: arXiv:1412.6980. doi: 10.48550/arXiv.1412.6980.

[23] V. N. L. Duy, S. Iwazaki, and I. Takeuchi, "Quantifying Statistical Significance of Neural Network-based Image Segmentation by Selective Inference," *Adv. Neural Inf. Process. Syst.*, vol. 35, pp. 31627–31639, Dec. 2022.

[24] D. Miwa, V. N. L. Duy, and I. Takeuchi, "Valid P-Value for Deep Learning-Driven Salient Region," Jan. 06, 2023, *arXiv*: arXiv:2301.02437. doi: 10.48550/arXiv.2301.02437.

[25] T. Katsuoka, T. Shiraishi, D. Miwa, V. N. L. Duy, and I. Takeuchi, "Statistical Test on Diffusion Model-based Generated Images by Selective Inference," Jul. 29, 2024, *arXiv*: arXiv:2402.11789. doi: 10.48550/arXiv.2402.11789.

[26] T. Katsuoka, *teruyukikatsuoka/DMAD-test*. (Jul. 10, 2024). Jupyter Notebook. Accessed: Aug. 28, 2024. [Online]. Available: https://github.com/teruyukikatsuoka/DMAD-test

[27] M. A. Napierala, "What is the Bonferroni correction?," *AAOS Now*, pp. 40–41, Apr. 2012.

[28] A. Dharamshi, A. Neufeld, K. Motwani, L. L. Gao, D. Witten, and J. Bien, "Generalized Data Thinning Using Sufficient Statistics," *J. Am. Stat. Assoc.*, vol. 0, no. 0, pp. 1–13, doi: 10.1080/01621459.2024.2353948.

2-2. Presentations

The 33rd JUACEP Workshop

for the summer research course students from the US and Canada

**10 minutes presentation + 4 minutes Q&A each*

【for Track A】 Date: Thursday, 8 August 2024 Venue: TEL Auditorium, EI Bldg.

13:30 – 13:35 Opening address by Prof. T. Matsumoto, JUACEP Committee

13:35 – 13:50 (1) **Seoyeong Park**, Advisor: Prof. N. Kawaguchi, Information & Communication Eng.
"Clustering-Based Multitask Classification for Predictive Consumer Behavior Modeling"

13:50 – 14:05 (2) **Utkarsh Srivastava**, Advisor: Prof. T. Fujii, Information & Communication Eng.
"Region of Interest Based Medical Image Compression"

14:05 – 14:20 (3) **Xiaoyue Wu**, Advisor: Assoc. Prof. K. Fujii, Intelligent Systems
"Optimization for Robust Lidar SLAM Framework for Predictive World Modeling Integration"

14:20 – 14:35 (4) **Raphaël Plante**, Advisor: Prof. T. Matsumoto, Mechanical Systems Eng.
"Educational Exploration of Topology Optimization: Key Concepts of the Exact Volume Constraint Method"

14:35 – 14:45 - Break time

14:45 – 15:00 (5) **Jacob Kokinda**, Advisor: Prof. N. Nishizawa, Electronics
"All-PM Tm-doped Ultra Short Pulse Fiber Laser Using SWNTs"

15:00 – 15:15 (6) **Gavin Silveira**, Advisor: Prof. T. Kato, Electrical Eng.
"Impact Assessment of Combination of Secondary and Tertiary Reserve Capacity Flexibility for Reducing Operating Costs in Power Systems with High Penetration of PhotoVoltaic Power in Japan"

15:15 – 15:30 (7) **Melody Polk**, Advisor: Advisor: Prof. H. Tomita, Applied Energy
"Improvements in Cavity Ring-Down Spectroscopy for Tritiated Water Analysis"

15:30 – 15:45 (8) **Maria Acuna**, Advisor: Assoc. Prof. K. Kinefuchi, Aerospace Eng.
"SWBLI Mitigation via Cryogenic Cooling: Numerical and Experimental Analysis"

15:45 – 15:55 - Break time

15:55 – 16:10 (9) **Edith Shear**, Advisor: Assoc. Prof. K. Kinefuchi, Aerospace Eng.
"Thrust Characteristics of Diverging Magnetic Field Thrusters"

16:10 – 16:25 (10) **Mohamed Diop**, Advisor: Prof. A. Yoshimura, Aerospace Eng.
"Comparative Study of Virgin and Recycled CFRPs Characteristics"

16:25 – 16:40 (11) **James Fernandez**, Advisor: Prof. J. Kasahara, Aerospace Eng.
"Synchronization of Dual Rotating Detonation Engines with Straight and Diverging Nozzles"

16:40 – 17:00 Completion ceremony: Address from Prof. M. Kobashi, Dean, Grad. School of Engineering

17:15 – Farewell banquet at Chez Jiroud

【for Track B】 Date: Thursday, 29 August 2024 Venue: TEL Auditorium, EI Bldg.

10:30 – 10:35 Opening address by Prof. Y. Ito, JUACEP Committee

10:35 – 10:50 (1) **Yukteshwar Ravi**, Advisor: Prof. T. Inoue, Mechanical Systems Eng.
"Development of a Novel Haptic System using a 3D Vibration Motor"

10:50 – 11:05 (2) **Rosemary He**, Advisor: Prof. I. Takeuchi, Mechanical Systems Eng.
"Statistical Testing on Generative AI Anomaly Detection Tools in Alzheimer's Disease Diagnosis"

11:05 – 11:15 Completion ceremony: Address from Prof. N. Umehara, JUACEP Committee

<3> Classes and Events

3-1. Orientation Sessions, Track A & B

JUACEP Summer Program 2024

[Track A] **Monday, June 3, 2024**

10:00 **Reception at ES Conference Room**
- Check-in. Distribution of the student ID card and Handbook
- Payment of the admission fee, tuition, campus insurance and Japanese textbook
- Scholarship

11:00 **Orientation at ES Conference Room**
- Welcome addresses from Dean, Prof. Kobashi, and JUACEP, Prof. Matsumoto
- Introduction of Faculty, Staff and Participants.

A) Schedule
B) Campus map
C) Japanese language class
D) Meet-up for JUACEP Students
E) Hands-on workshop
F) Excursion
G) Workshop
H) Reports and evaluation
I) Life information
    a) Nagoya University ID and Information security training
    b) University's security department warning
    c) Medical and health care: Medical services, Health precautions
    d) Dormitory, Transportations, Accidents, Compliance of law, etc.

11:45 **Introduction of the Lab Mentors and TAs**
12:00 **Adjournment and Settlement at each laboratory**
15:00 **Meeting at ES lobby and transfer to the dormitory**

[Track B] **Monday, June 17, 2024**

10:00 **Reception at ES Conference Room**
- Check-in. Distribution of the student ID card and Handbook
- Payment of the admission fee, tuition, campus insurance and Japanese textbook
- Scholarship

11:00 **Orientation at ES Conference Room**
- Welcome addresses from JUACEP, Prof. Umehara
- Introduction of Faculty, Staff and Participants.

J) Schedule
K) Campus map
L) Japanese language class
M) Meet-up for JUACEP Students
N) Hands-on workshop
O) Excursion
P) Workshop
Q) Reports and evaluation
R) Life information
    e) Nagoya University ID and Information security training
    f) University's security department warning
    g) Medical and health care: Medical services, Health precautions
    h) Dormitory, Transportations, Accidents, Compliance of law, etc.

11:45 **Introduction of the Lab Mentors and TAs**
11:55 **Photo shoot with all involved in Track A and B**
12:00 **Welcome Lunch for Track A and B**
13:00 **Adjournment and Settlement at each laboratory**
15:00 **Meeting at ES lobby and transfer to the dormitory**

3-2. Japanese Syllabus

JUACEP Summer Program 2024 Japanese Course Syllabus

Course name	Japanese Language
Teaching staff	Ms. YASUI, Sumie
Course period	June 18 - July 18, 2023
Weekly timetable	13:45 - 16:15, Tuesday and 13:45 - 16:15, Thursday
Classroom	NEOREX Pod B, 3F, Nagoya University Central Library >>> Location next page
Textbook	“GENKI An Integrated Course in Elementary Japanese” I (The Japan Times) This textbook is a comprehensive approach to developing the four basic language skills (listening, speaking, reading and writing) in order to cultivate overall Japanese-language ability. *Some teaching material will be given in class.
Course Contents	**Course outline** The purpose of this course is to introduce the most essential Japanese words and expressions for everyday life. Students will learn writing system (Hiragana & Katakana), the basic grammar, expressions of Japanese. **Classroom activities** Basic communication skills required in everyday life will be taught by introducing new vocabulary, new grammar, and practicing listening, conversation and role-playings. **Homework and Quiz** You are expected to submit your homework by the deadline. Quizzes will be given every day in class. 1. Hiragana 2. Katakana 3. Dictation 4. Conjugation
Evaluation	1. Homework 20% 2. Quizzes 30% 3. Oral exam. 50% 100% More than 80% attendance is required. You will be officially awarded 1 credit of Nagoya University. **A+: 100-95 A: 94-80 B: 79-70 C: 69-65 C-: 64-60 F(fail): 59-0**
	1. 6/18 (Tue) Greeting Expressions, Hiragana 1 Introducing yourself, Noun sentences 1, Occupation, Nationality, Age, Numbers 1-100 **2. 6/20 (Thu)** Classroom expressions, Hiragana 2 Shopping, Noun sentences 2, Price, Numbers 101-1,000,000 **3. 6/25 (Tue)** Hiragana 3 Describing where things are, Locations Placing an order at a restaurant **4. 6/27 (Thu)** Hiragana 4 Talking about your daily life Verbal sentences 1, Time reference, Adverbs **5. 7/2 (Tue)** Hiragana 5 Invitations, Suggestions, Desires Verbal sentences 2, Days/Weeks/Months/Years, Counting **6. 7/4 (Thu)** Katakana 1 Talking about your family Adjectives, Likes or Dislikes, Degree expressions, Family terms **7. 7/9 (Tue)** Katakana 2 Talking about your week-end, Past tense, Time words **8. 7/11 (Thu)** Katakana 3 Making a request (Verb-Te-form), Progressive actions, Describing your status **9. 7/16 (Tue)** Asking permission, Prohibition, Negative request Describing two things Talking about your interests Plain form **10. 7/18 (Thu)** **The Final Examination (speaking)**

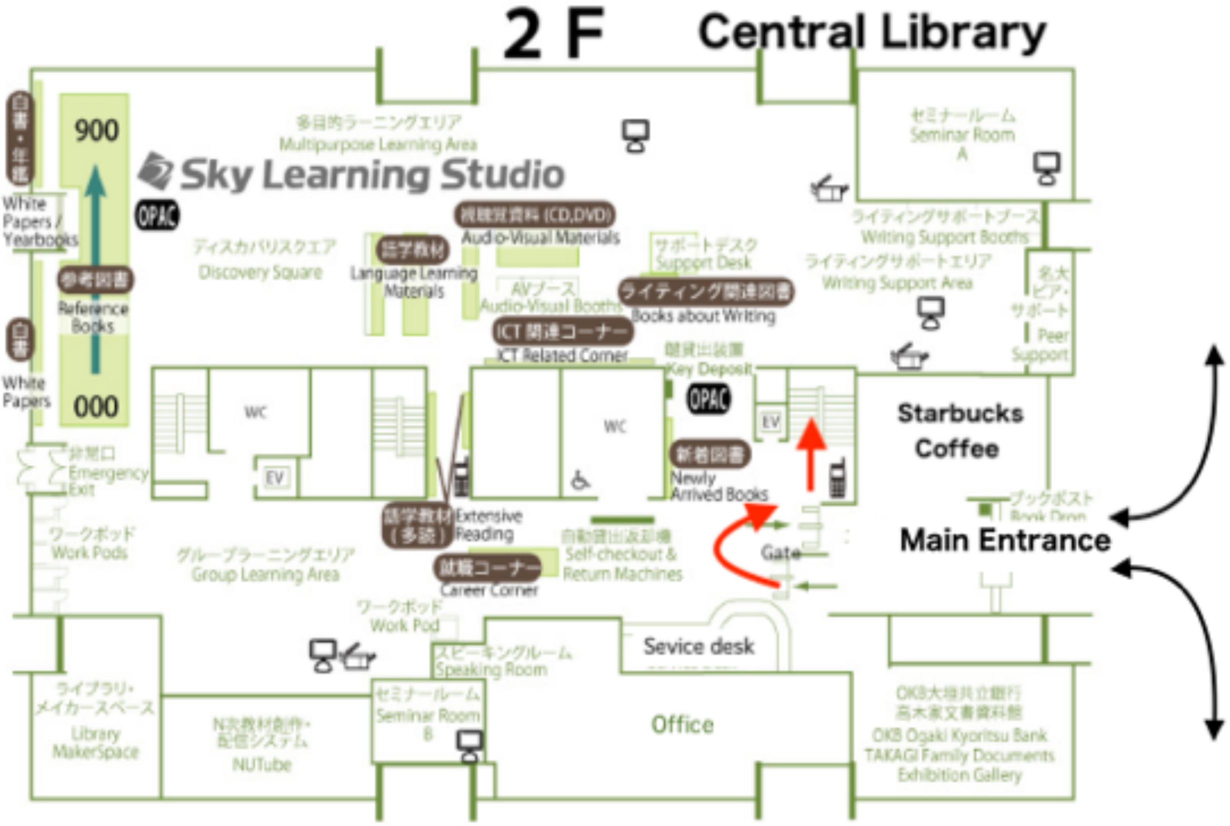
2 F
Central Library
900
000
白書・年鑑
White Papers / Yearbooks
参考図書
Reference Books
白書
White Papers
OPAC
Sky Learning Studio
多目的ラーニングエリア
Multipurpose Learning Area
ディスカバリスクエア
Discovery Square
語学教材
Language Learning Materials
視聴覚資料 (CD,DVD)
Audio-Visual Materials
AVブース
Audio-Visual Booths
ICT 関連コーナー
ICT Related Corner
サポートデスク
Support Desk
ライティング関連図書
Books about Writing
セミナールーム
Seminar Room
A
ライティングサポートブース
Writing Support Booths
ライティングサポートエリア
Writing Support Area
名大ピア・サポート
Peer Support
鍵貸出装置
Key Deposit
OPAC
WC
EV
WC
EV
新着図書
Newly Arrived Books
Starbucks Coffee
ブックポスト
Book Drop
Main Entrance
Gate
非常口
Emergency Exit
ワークポッド
Work Pods
語学教材（多読）
Extensive Reading
グループラーニングエリア
Group Learning Area
就職コーナー
Career Corner
自動貸出返却機
Self-checkout & Return Machines
ワークポッド
Work Pod
スピーキングルーム
Speaking Room
Sevice desk
ライブラリ・メイカースペース
Library MakerSpace
N式教材制作・配信システム
NUTube
セミナールーム
Seminar Room
B
Office
OKB大垣共立銀行高木家文書資料館
OKB Ogaki Kyoritsu Bank TAKAGI Family Documents Exhibition Gallery

3階


3 F
学習用図書
Books for Undergraduates
200
300
OPAC
400
500
600
伝記コーナー
Biography Corner
留学生用英語基本図書
Books for International Students
WC
EV
WC
学習用辞書
Dictionaries for Undergraduates
EV
自動貸出機
Self-Checkout Machine
OPAC
文庫
Bunko-Style Paperbacks
新書
Shinsho-Style Paperbacks
新着雑誌
Current Journals
ブラウジングルーム
Browsing Room
岩波ブックレット
Iwanami Booklet
100
000
OPAC
900
700
大型書・大型本（大型図書：美術・芸術）
Large Art Books
留学生コーナー
International Students Corner
旅行ガイド
Travel Guide
新着雑誌
Current Journals
ゆかり交流ラウンジ
Yukari Lounge
NEOREX Pods
B
A
C3
C2
C1
主要新聞（当日分）
Major Newspapers (Today's Issue)
ゆかり文庫
Yukari collection

3-3. Meet-up for JUACEP Students

Round-Table Discussion with JUACEP participants:

Information on study abroad in the U.S. & Canada and more!

16:30 Thursday
June 20, 2024

at Aerospace Meeting
Room #347, 3F, EB-2N

We invite the prospective JUACEP participants and engineering students interested in studying abroad to meet our guest students from the U.S and Canada, listen to their short talks, ask questions, and make new friends.

- To reduce anxieties of your life abroad
- To know what you need for the beginning of your life abroad
- To have dependable friends in your life abroad....

Inquiry
↓
office@juacep.engg.nagoya-u.ac.jp
phone +81-52-789-2799 (内線2799/3179)

Inquiry → office@juacep.engg.nagoya-u.ac.jp
phone +81-52-789-2799 (内線2799/3179)
https://www.juacep.engg.nagoya-u.ac.jp/

Round-Table Discussion for JUACEP Students

2024年6月20日（木）16:30～

工学部2号館3階　航空大会議室

海外留学を考えているみなさん、
JUACEP留学生と気軽に情報交換しませんか

- 現地生活での不安を減らしたい…
- 留学生活を始めるのに必要なものは…
- 現地で頼れる友達がいたらいいのに…

3-4. Field Trip

JUACEP Excursion

June 28, 2024

Date: Friday, June 28, 2024

Fee: 3,000 yen …Collect in cash in the morning. Lunch not included.

Destinations: JERA Park, Mizkan Museum, Toyota Commemorative Museum of Industry and Technology

*Wear casual clothes and sneakers as you will walk around factories.
*Bring NU student ID card.

Schedule:

Time	Visiting spots	Transportation
9:00	Meeting at Toyoda Auditorium and departure from campus	Hired bus
10:30	Arrival at JERA Park	
12:10	Departure from JERA Park	
	Lunch on the way, (Aoi Park, Hekinan)	
13:20	Arrival at Mizkan Museum	
14:30	Departure from Mizkan Museum	
15:30	Arrival at Toyota Commemorative Museum	
17:00	Departure from Toyota Museum	
17:30	Arrival at Nagoya University	
18:00	Dinner at GRAN PIATTO	
20:00	Adjournment	

*Schedule above is tentative and may be changed.

3-5. Hands-on Workshop

Date: 13:00 – 16:30, July 5th for Group 1 and July 8th for Group 2

Place: Creation Plaza, EI 201

Staff: Members of Creation Plaza
Members of Technical section
JUACEP TAs

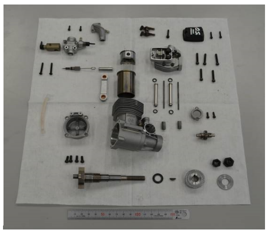

Contents:

1. Opening remarks
2. Introduction to the basis of the Internal Combustion Engine and other engines (History, Characteristics, Operation principle, Demonstration of engines)
3. Disassembling → Assembling → Adjustment
4. Performance test
5. Jet engine demonstration
6. Discussion, questionnaire

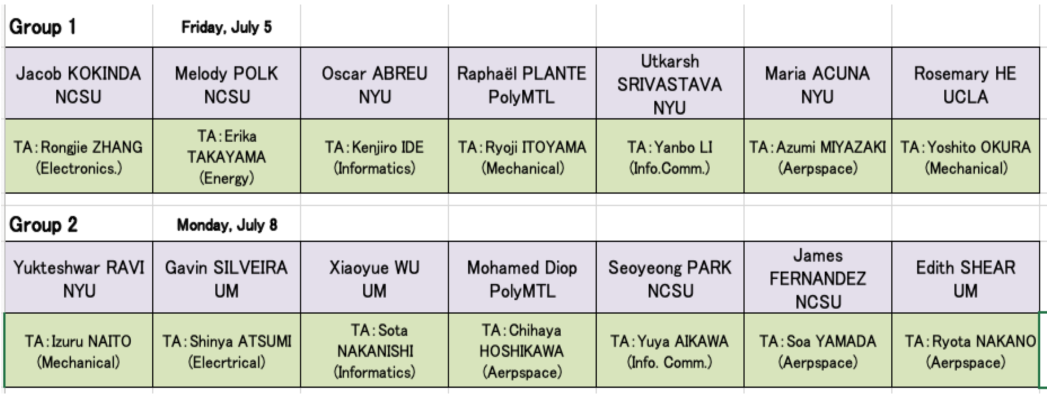

Group 1	**Friday, July 5**					
Jacob KOKINDA NCSU	Melody POLK NCSU	Oscar ABREU NYU	Raphaël PLANTE PolyMTL	Utkarsh SRIVASTAVA NYU	Maria ACUNA NYU	Rosemary HE UCLA
TA:Rongjie ZHANG (Electronics.)	TA:Erika TAKAYAMA (Energy)	TA:Kenjiro IDE (Informatics)	TA:Ryoji ITOYAMA (Mechanical)	TA:Yanbo LI (Info.Comm.)	TA:Azumi MIYAZAKI (Aerpspace)	TA:Yoshito OKURA (Mechanical)
Group 2	**Monday, July 8**					
Yukteshwar RAVI NYU	Gavin SILVEIRA UM	Xiaoyue WU UM	Mohamed Diop PolyMTL	Seoyeong PARK NCSU	James FERNANDEZ NCSU	Edith SHEAR UM
TA:Izuru NAITO (Mechanical)	TA:Shinya ATSUMI (Elecrtrical)	TA:Sota NAKANISHI (Informatics)	TA:Chihaya HOSHIKAWA (Aerpspace)	TA:Yuya AIKAWA (Info. Comm.)	TA:Soa YAMADA (Aerpspace)	TA:Ryota NAKANO (Aerpspace)

3-6. The 33rd JUACEP Workshop

The 33rd JUACEP Workshop

2024 Summer Research Course, Track A

Date **13:30 - 17:00** **August 8, 2024**

Venue **TEL Auditorium (3F, EI Bldg.)**

No prior registration required.

13:30 Opening address by Prof. T. Matsumoto, JUACEP Committee

13:35 (1) Seoyeong Park Advisor: Prof. N. Kawaguchi, Information & Communication Eng.
“Clustering-Based Multitask Classification for Predictive Consumer Behavior Modeling”

13:50 (2) Utkarsh Srivastava Advisor: Prof. T. Fujii, Information & Communication Eng.
“Region of Interest Based Medical Image Compression”

14:05 (3) Xiaoyue Wu Advisor: Assoc. Prof. K. Fujii, Intelligent Systems
“Optimization for Robust Lidar SLAM Framework for Predictive World Modeling Integration”

14:20 (4) Raphaël Plante Advisor: Prof. T. Matsumoto, Mechanical Systems Eng.
“Educational Exploration of Topology Optimization: Key Concepts of the Exact Volume Constraint Method”

14:35 Break time

14:45 (5) Jacob Kokinda Advisor: Prof. N. Nishizawa, Electronics
“All-PM Tm-doped Ultra Short Pulse Fiber Laser Using SWNTs”

15:00 (6) Gavin Silveira Advisor: Prof. T. Kato, Electrical Eng.
“Impact Assessment of Combination of Secondary and Tertiary Reserve Capacity Flexibility for Reducing Operating Costs in Power Systems with High Penetration of PhotoVoltaic Power in Japan”

15:15 (7) Melody Polk Advisor: Advisor: Prof. H. Tomita, Applied Energy
“Improvements in Cavity Ring-Down Spectroscopy for Tritiated Water Analysis”

15:30 (8) Maria Acuna Advisor: Assoc. Prof. K. Kinefuchi, Aerospace Eng.
“SWBLI Mitigation via Cryogenic Cooling: Numerical and Experimental Analysis”

15:45 Break time

15:55 (9) Edith Shear Advisor: Assoc. Prof. K. Kinefuchi, Aerospace Eng.
“Thrust Characteristics of Diverging Magnetic Field Thrusters”

16:10 (10) Mohamed Diop Advisor: Prof. A. Yoshimura, Aerospace Eng.
“Comparative Study of Virgin and Recycled CFRPs Characteristics”

16:25 (11) James Fernandez Advisor: Prof. J. Kasahara, Aerospace Eng.
“Synchronization of Dual Rotating Detonation Engines with Straight and Diverging Nozzles”

16:40 Completion ceremony: Address from Dean, Prof. M. Kobashi

The participants will deliver presentations (10mins. + Q&A 4mins.)
based on their research topics of the home universities and NU.

Inquiry: JUACEP Office
052-789-2799
office@juacep.engg.nagoya-u.ac.jp

名古屋大学
NAGOYA UNIVERSITY

Nagoya university
JUACEP
Japan-US-Canada Advanced
Collaborative Education program

Program Website

The 33rd JUACEP Workshop II

2024 Summer Research Course, Track B

Date:

10:30-11:15

August 29, 2024

Venue:

TEL Auditorium,
EI Bldg. 3F

名古屋大学
NAGOYA UNIVERSITY

Nagoya university
JUACEP

Japan-US-Canada Advanced
Collaborative Education program

10:30 – 10:35
Opening address: Prof. Yasumasa Ito, JUACEP Committee

10:35 – 10:50
(1) Yukteshwar Ravi, "Development of a Novel Haptic System using a 3D Vibration Motor"
Adviser: Prof. Tsuyoshi. Inoue, Mechanical Systems Engineering

10:50 – 11:05
(2) Rosemary He, “Statistical Testing on Generative AI Anomaly Detection Tools in Alzheimer's Disease Diagnosis”
Adviser: Prof. Ichiro Takeuchi, Mechanical Systems Engineering

11:05 – 11:15
Completion ceremony

The participants will deliver presentations (10mins. + Q&A 4mins.) based on their research topics of the home universities and NU.

Inquiry: JUACEP Office
052-789-2799
office@juacep.engg.nagoya-u.ac.jp

Program Website

<4> Participation Essays and Questionnaires

4-1. Findings through JUACEP

Findings through JUACEP

Name: Maria Acuña
Affiliation at home country: Department of Mechanical and Aerospace Engineering, New York University Tandon School of Engineering
Participated program: Summer Course 2024

Research theme: SWBLI Mitigation via Cryogenic Cooling: Numerical and Experimental Analysis
Advisor at Nagoya Univ: Assoc. Prof. K. Kinefuchi
Affiliation at Nagoya Univ.: Department of Aerospace Engineering, Graduate School of Engineering

Through JUACEP, I had the incredible opportunity to conduct research at Nagoya University whilst also being able to experience Japanese culture and travel around Japan. Nagoya University has been on my radar for a few years now. When I was an undergraduate, I was meant to do an exchange at Nagoya University as part of my degree, however, due to the pandemic, I was unable to do so. As such, when the opportunity was presented to study here as a graduate student, it was one that I could not turn down.

Prior to coming to Nagoya, I had limited research experience. I was excited to see the laboratory setup at the university, as my home university in New York does not have nearly as much emphasis on physical experimentation. As such, the work I have done here has provided me with much needed experience. From the first day of the program, the members of my lab were warm and welcoming. They always made an effort to make us feel included. The environment was a very kind one, and there was always someone to answer any question I might have, whether it be regarding research or life in Japan.

Furthermore, during my stay in Japan, I also was able to visit Kyoto, Osaka, and Tokyo. Through these trips, I was able to learn more about the rich history and traditions of Japan, as well as witness the vibrant culture unique to each city. From the shrines in Kyoto, to the nightlife of Osaka, to the vibrancy of Tokyo, Japan truly has incredible sights to behold. These experiences were priceless to me and will remain as very fond memories.

My stay in Japan

Name: Mohamed Mokhtar Diop
Affiliation at home country: Polytechnique Montréal
Participated program: Summer Course 2024
Research theme: Comparative study between recycled and virgin carbon fibers properties
Advisor at Nagoya Univ: Prof. YOSHIMURA Akinori
Affiliation at Nagoya Univ.: Aerospace Engineering

Having been able to come to Japan was an incredible opportunity for me. I liked the culture and most importantly the kindness and politeness of people, that's the main thing that sticks out for me.
I had the chance to visit a lot of beautiful places such as Nagoya, Kyoto, Gifu and Hamamatsu. They show the richness of the Japanese territory.
I will go back to Canada with a lot of good memories that will stay with me for the rest of my life. I don't forget to mention the people I shared these experiences with, who from now on will be part of my circle of friends.

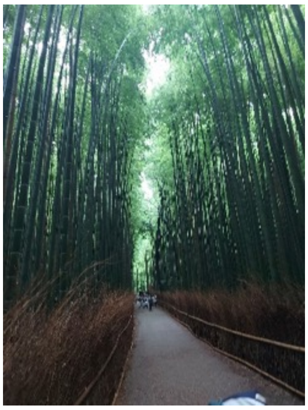

People are very welcoming, polite and kind. I knew a little bit about the characteristics of the Japanese but that doesn't keep from being amazed by it.

I would like to give a special shoutout to my advisor Pr. YOSHIMURA Akinori who agreed to welcome me, consider me as one of his students and shared his knowledge with me. His pieces of advice have been very helpful. I wouldn't be grateful if I didn't mention my labmates who helped me a lot throughout this journey. They helped me to find solutions to the issues I faced within the frame of this internship. They usually put their own work aside just to assist me in my research. I want also to extend my thanks to all the other students from the other university I have met along the way. Finally, my last words go to the JUACEP office without whom I wouldn't be able to live this experience.

Findings through JUACEP

Name: Edith Shear
Affiliation at home country: Department of Aerospace Engineering, The University of Michigan, Ann Arbor
Participated program: Summer 2024

Research theme: Small Scale Thrust Characteristics of Diverging Magnetic Field Thrusters
Advisor at Nagoya University: Assoc Prof. K. Kinefuchi
Affiliation at Nagoya University: Department of Aerospace Engineering, Graduate School of Engineering

From day one, I have enjoyed the environment of my laboratory. They have been very open and welcoming. I surprisingly ended up meeting someone who had also attended the same undergraduate university as me. Although we didn't know each other during our time there, we ended up crossing paths years later here on the other side of the world., what a sign from the universe! My PI has been very enthusiastic and helpful throughout my entire process, along with my lab supervisors. I have enjoyed the work that is done here deeply and it has pushed me to return to similar labs at my home university.

My experience in Japan has been nothing short of amazing. This is my second time going abroad for a summer research program and it has reminded me of everything I love about participating in international research along with exploring new cultures, interacting with new people, and seeing new places. I've cherished my cohort and have made many friends during this journey. It brings me joy to know that some of them will be coming back with me to my home university, and for those who won't it has been a definite pleasure knowing. We've shared a lot of memories, both in the lab and immersing ourselves in all the vibrant colors of Japan.

Over the weekends, I had the opportunity to travel from Nagoya to Kyoto, Osaka, and even Tokyo, and it's been an amazing experience overall. I truly believe that this program has further changed me, encouraging me to grow as a researcher and an individual. As a result of the lasting impression Japan has left on me, I will be bringing Japan's lasting imprint home.

Findings through JUACEP

Name: Rosemary He
Affiliation at home country: Computer Science, UCLA
Participated program: Summer Course 2024

Research theme: Statistical testing, generative AI
Advisor at Nagoya Univ: Prof. Takeuchi Ichiro
Affiliation at Nagoya Univ.: Department of Mechanical Systems Engineering

I applied to the program in hopes of gaining experience and insight into studying and working in Japan as a researcher. I had visited Japan before and enjoyed it so much that I began thinking the possibility of living in Japan long term. I had researched online and while there were different voices, the main theme was that Japan's culture and work environment are very different from the United States, which is something that cannot be discovered on a vacation. With that in mind, I started my program of 10 weeks in hopes to find out if living in Japan would be a good fit for me.

Though I was a bit nervous about starting research in a new environment and expectations, my professor at Nagoya University was so welcoming and thoughtful that the nervousness quickly went away. As my professor was well traveled and had studied abroad, I found my interactions with him very similar to my advisors back home. A difference I noticed between research labs in Japan and US is that Japanese labs are quite big (for example my lab had 40 members from undergraduates to professors) and you don't get to interact with most of the students often. For instance, my group worked on statistical testing methods while another group worked on computer vision. In the US, lab meetings are usually weekly and all students in the lab would join and share their research. As such, I mainly interacted with members of my research group, who were very kind in guiding my research and helping me through the project. Though there were some language barriers (I really wished I could speak better Japanese), everyone was so welcoming and accommodating that I wish I could stay in the lab for longer. As such, I would gladly return if given the opportunity.

Outside my research life, I traveled all over Japan [8 weekends + Obon] during my free time. It was so wonderful! The summer heat can be a bit much, but I visited so many beautiful places that I would not have had the chance to. From scuba diving in Okinawa to biking along the Shimanami Kaido, I got to appreciate Japan's beautiful nature and scenery, and best of which the food. Nagoya has so much to offer as well, from shopping in Osu to beautiful castles, I came to the program thinking I would travel solo but made many friends through the program that made the journey even more fun.

As 10 week flies by and I begin to reflect this summer, I am very glad to join the program and learned so much more than I expected. With limited experience, I would consider working and living in Japan and have become a little more confident in my ability to enjoy myself here.

Findings through JUACEP

Name: James Fernandez
Affiliation at home country: Department of Mechanical and Aerospace Engineering, North Carolina State University
Participated program: Summer Course 2024
Research theme: Synchronization of Dual Rotating Detonation Engines with Straight and Diverging Nozzles
Advisor at Nagoya Univ: Prof. Jiro Kasahara
Affiliation at Nagoya Univ.: Department of Aerospace Engineering, Graduate School of Engineering, Nagoya University

Beginning the application process for the JUACEP program I was very nervous, because I had never left the United States before and a 10-week trip seemed intimidating. Following the program, I can proudly say it was one of the best decisions I have ever made! This program provided me with both cultural and research related experiences I will always remember and appreciate.

I began this program very shortly after finishing my undergraduate degree at NC State and to this point had little to no experience with actual hands-on testing of detonation engines. My experiences in Prof. Kasahara's lab were very positive. My fellow lab mates happily and helpfully guided me through the testing process and aided me throughout my research. The lab environment was extremely accepting, filled with constant collaboration and enjoyable conversations. I was able to finish my tests with great results and feeling much more knowledgeable in the field.

I was very grateful to participate in the Japanese language course here as well. I found the class very enjoyable and felt more comfortable with general communication following each lecture. My favorite moment from the class was when I felt comfortable reading Katakana, and I would be able to recognize some English words while walking the streets of Japan.

My fellow JUACEP members in my group were very fun and adventurous people that I am very grateful to have met and explored Japan with. We tried to explore a new part of Japan every weekend. The first two weeks we explored Nagoya. We went to Nagoya Castle and Nagoya Port and saw the many beautiful things the city had to offer. After that we took a trip to Gifu and hiked throughout Yoro Falls admiring the beautiful waterfall and surroundings. One weekend we went to Kyoto and immersed ourselves in the culture by walking the historic streets and exploring shrines. At Fushimi Inari Taisha, our group was very happy to be interviewed by young Japanese students in an English class, curious about life in the America. Later, we explored Osaka, Nara, and Tokyo. Osaka was extremely vibrant and exciting, with great food and a very fun nightlife. Nara was my favorite experience. Walking throughout Nara Park and interacting with the deer was extremely peaceful and fun. Even reading about Nara Park, I had no idea how pleasant the experience would be. Tokyo was incredibly exciting. Walking through Shibuya crossing, shopping in the popular Japanese stores, and experiencing the nightlife was unforgettable. The most important realization I had through my time in Japan is that no matter where you are, the people are incredibly kind, and the food is going to be fantastic.

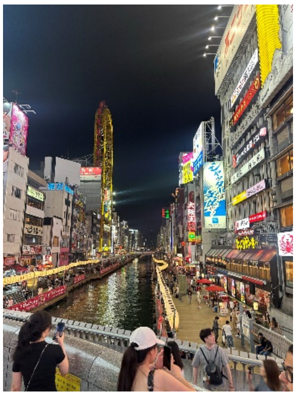

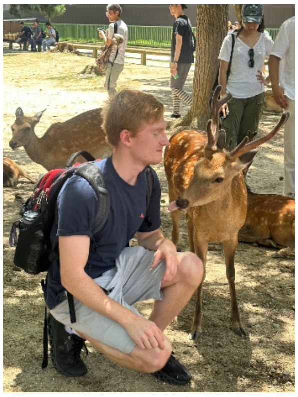

Findings through JUACEP

Name: Jacob Kokinda
Affiliation at home country: North Carolina State University,
Department of Electrical and Computer Engineering
Participated program: Summer Course 2024

Research theme: Ultra Short Pulse Fiber Lasers
Advisor at Nagoya Univ: Prof. Nishizawa Norihiko
Affiliation at Nagoya Univ.: Electronics Engineering

Having been to Japan before, as a tourist, I saw this program as an opportunity not only for my academic career but as a chance to experience what everyday life is like in Japan. I have always respected Japan for its lifestyle, societal structure, and cultural values. I have been studying the language for the past couple of years with the hopes of one day being able to stay in Japan for an extended period of time. Throughout my time here, I have been able to experience life as a local university student beyond just the fun things, including shopping for essentials at grocery/department stores, paying bills, taking daily public transportation, navigating communication with native people, etc. Having almost 3 months to think about how life is here in Japan, I have been able to confirm that it is a place in which I could see myself staying for a while and even calling home in the future.

Regarding my research experience in this program, it has been a great blessing working with talented people from a different background than mine. My research field, here at Nagoya University, is a slightly different but adjacent field to my own at North Carolina State University. I have learned a lot about this new field that will carry over to my projects back home and it has possibly even opened new doors for future career paths that I had not considered before.

In conclusion, this program has been infinitely valuable to my life beyond mere curiosity. It has helped me answer my own questions of where and how I want to continue my life after graduation and through what means will I achieve that. Perhaps the connections I have made and the knowledge I have gathered during my time with JUACEP, will one day be the key to reaching the life I have been searching for.

Findings through JUACEP

Name: Raphaël Plante
Affiliation at home country: Mechanical Engineering, Polytechnique Montréal
Participated program: Summer Course 2024

Research theme: Topological Optimization
Advisor at Nagoya Univ: Prof. T. Matsumoto
Affiliation at Nagoya Univ.: Computational Mechanics

Research: This program provided an opportunity for me to research a subject I was previously uncomfortable with. At such an advance academic level as that the research master is, it is rare to be able to completely change the subject of your study for the sake of personal knowledge. I had a lot of fun working on Topological Optimization. It reminded me of how much I loved calculus and helped me realize that I don't despise algebra as much as I thought.

Lectures: By attending a few seminars, I was able to see the different applications of Topological Optimization.

Nagoya University: Nagoya University offered me a glimpse of campus life. My home university is not located on a campus; I live far away from it, and there are not many things to do around it. NU provided me with a life with roommates, a 15 -minute walk from the residence to the school, and a lot of places to eat and hang out nearby.

Environment: I was pleased with the work environment. Air conditioning was essential due to the intense heat I wasn't used to. I was provided with a screen monitor, a desk and a nice new chair. On the first day, my advisor, Prof. Matsumoto and my TA, Ryoji, took the time to walk me around the campus, which really made me feel welcomed.

Excursion: The excursion prepared by JUACEP was an interesting opportunity, as it allowed us to visit places we might not have considered, such as the power plant at JERA park and Mizkan museum. Toyota museum was a must, and I would have visited it regardless.

Life in Nagoya: The life in Nagoya is efficient. The public transportation system is reliable, making it easy to travel between different parts of the city. The city is also diverse. If you want to go out, the nightlife of Sakae is the way to go. If you want to relax, a few onsens are accessible, such as the one near Ozone Station.

Life in Japan: Life in Japan has been enjoyable. The context of the exchange allowed me to explore the country on weekends. I was able to climb Fushimi-Inari in Kyoto, see Nara's sacred deer, eat Takoyaki in Osaka, and experience the nightlife of Tokyo. The Shinkansen is a great way to travel across the country, but be aware: while the train can take you anywhere, your wallet may not.

Cultural differences: A major cultural difference I notice was the way Japanese students handle the heat. It seems that appearance is more important than comfort. With the thermostat oscillating around 35 °C, people would use a fan to cool their face, and a towel to wipe the sweat, all while wearing nice looking baggy pants and long-sleeve shirts. This is a true testament to fashion!

Impact of the JUACEP on my future Career: This program broadened my search for opportunities worldwide. Before this, I never thought of working or doing research anywhere other than Montreal. I now know how welcoming people can be, even if you are unfamiliar with their culture or language. Although I want to grow old in my home country, I will be the first to volunteer for international assignments, such as visiting Japan to meet clients, knowing I can build meaningful relationships.

Findings through JUACEP 2024

Name: Melody Polk
Affiliation at home country: Department of Nuclear Engineering, North Carolina State University

Participated program: Summer Course 2024

Research theme: Detection of Trace Radioisotopes through Cavity Ring-Down Spectroscopy
Advisor at Nagoya Univ: Prof. Tomita
Affiliation at Nagoya Univ.: Department of Applied Energy

The JUACEP 2024 experience in Japan was an excellent opportunity to advance my nuclear research knowledge and immerse myself in a new culture and environment. I am grateful for the support provided by the Tomita group and for the connections I made with the other international students in the lab. Spending the summer in Japan this program allowed enough time to explore multiple cities, and I thoroughly enjoyed the beautiful and culturally rich locations. While I initially expected to enjoy the city locations the most, I found the serene mountainous areas to be fascinating and some of my favorite locations.

One thing I will miss upon returning to the US, is Japan's advanced transportation system which made it easy to visit multiple major cities as well as smaller beach and mountain areas within a short period of time. In terms of my research, my work on cavity ring-down laser spectroscopy has broadened my understanding of techniques for measuring trace radioisotopes, which is relevant to nuclear engineering. Overall, experiencing a different culture and research environment was incredibly enriching, and I am thankful for the JUACEP opportunity.

Findings through JUACEP

Name: Yukteshwar Ravi
Affiliation at home country: Mechatronics and Robotics & New York University
Participated program: Summer Course 2024
Research theme: Development of a Novel Haptic System Using a 3D Vibration Motor
Advisor at Nagoya Univ: Prof. Tsuyoshi Inoue
Affiliation at Nagoya Univ.: Mechanical Engineering

Choosing Japan for my summer internship is one of the best decisions I have made in my life.
As a kid growing up in India, watching *Dragon Ball Z* and Akira Kurosawa's movies, and being a huge fan of the infamous author Osamu Dazai, I always wanted to visit Japan. I was fascinated by their culture, the polite people, but never had the opportunity to actually visit the country. I was in my first year of a master's degree, chasing my American dream at NYU when I learned about the JUACEP program. When I received the acceptance, I was beyond thrilled, knowing that my dream of visiting Japan was finally going to come true.

When I first arrived, I discovered that almost no one knew English. This was both good and bad news for me. The bad news was that I would have to rely on others or phone apps; the good news was that I was finally going to be learning, or at least trying to learn, Japanese. Fortunately, the JUACEP program offered a 10-class Japanese course over 5 weeks, which was incredibly helpful, especially for navigating and ordering food in restaurants.

The research project was very engaging. My lab mates, along with my sensei who guided me step by step, helped me a lot. The lab environment was so friendly that it was hard to believe I was a foreign student. Whenever my sensei saw me working harder than usual, he would say, "Working and researching is fine, but please enjoy Japan, go around and explore the country, make yourself at home." And I took his advice very seriously. I worked in the lab with my fellow students five days a week, Monday to Friday, and we had breaks on Saturday and Sunday, during which, as my sensei suggested, I explored Japan and its rich culture. During my 3-month stay, I visited Tokyo, Kyoto, Gifu, Osaka, Kobe, Himeji, Hiroshima, Okinawa, Hokkaido, and fully explored Nagoya. Japan is more than just its world-famous places; it's the people and culture—the countless kabuki (Japanese drama) I attended, bunraku shows (puppetry), izakayas, food, tea ceremonies, geisha performances, samurai history and experiences, various palaces and castles, the mountains, nature, beaches, anime fandom, and most importantly, their food. The list goes on endlessly. The people I met through this program—my fellow JUACEP students, my lab mates, and the staff—are some of the best people I have ever met in my life. I am truly going to miss them. And after everything, I feel like no matter how many times I repeat this cycle, I will never get tired of it.

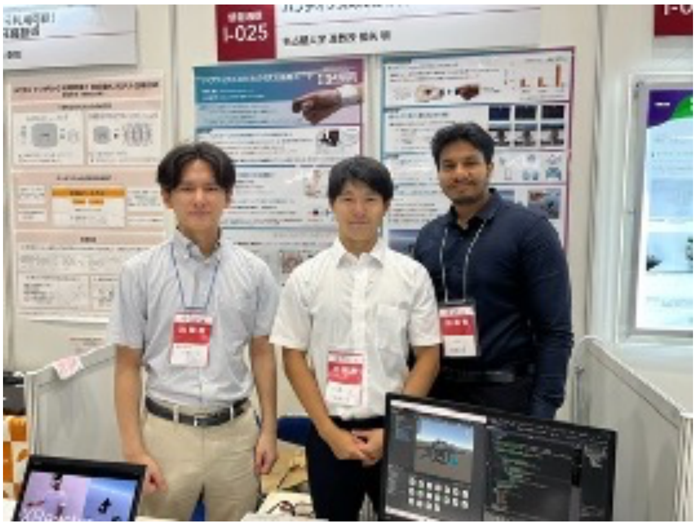

Looking back, the JUACEP program has not only fulfilled a lifelong dream but has also profoundly influenced my outlook on life and my future career. Immersing myself in Japan's rich culture, engaging in meaningful research, and forging connections with new friends have all contributed to my growth as an individual and a professional. This experience has sparked a deeper appreciation for cross-cultural exchange and reinforced my desire to continue exploring and learning in this vibrant and dynamic world. I am confident that the lessons I've learned and the skills I've developed will guide me as I pursue more ambitious challenges in the future.

Findings through JUACEP

Name: Seoyeong Park
Affiliation at home country: Department of Computer Science, North Carolina State University
Participated program: Summer Course 2024

Research theme: Clustering-Based Multitask Classification for Predictive Consumer Behavior Modeling
Advisor at Nagoya Univ: Prof. Nobuo Kawaguchi
Affiliation at Nagoya Univ.: Information and Communication Engineering

Ever since my first trip to Tokyo, it took five years to revisit Japan. I am incredibly thankful for the opportunity to return and experience life in Japan once more, this time as a researcher at a prestigious university. This summer at Nagoya, through the JUACEP program, I had the chance to significantly expand my research while working in the lab under the guidance of Professor Kawaguchi.

The time spent at Nagoya was transformative for my growth as a researcher. Under Professor Kawaguchi's mentorship, I delved deeply into my studies, generating ideas and achieving outcomes far beyond my initial expectations. The support from Professor Kawaguchi and Tahera was invaluable, as they provided extensive guidance and encouragement. My lab colleagues were incredibly welcoming, helping me to integrate into Japanese society and the lab environment. This program has undoubtedly solidified my future career path, giving me clarity and direction.

Balancing work and leisure, I made the most of my weekends by traveling extensively across Japan. I visited several fascinating cities, including Tokyo, Kyoto, Shizuoka, Uji, Nara, and, of course, Nagoya. The excursion organized by JUACEP was an extraordinary opportunity to explore places I might not have ventured to on my own. Despite the intense summer heat, Japan's beauty was ever-present, making each journey memorable.

Although my stay was just over two months, I immersed myself in daily life in Japan, gaining a profound appreciation for its culture and lifestyle. This experience was a blend of rigorous academic work and enriching cultural exploration, making it an unforgettable chapter in my life.

Findings through JUACEP

Name: Gavin Silveira
Affiliation at home country: Integrative Systems + Design, University of Michigan
Participated program: Summer 2024

Research theme: Energy Systems Engineering
Advisor at Nagoya Univ: Prof. Takeyoshi Kato
Affiliation at Nagoya Univ.: Electrical Engineering, Institute of Materials and Systems for Sustainability (IMaSS)

My research internship at Nagoya University was an exciting opportunity to collaborate with Japanese researchers working in the field of renewable energy systems. Despite the language barrier, my professors and labmates made sure to explain anything I needed to know so that I have a good understanding on the operation and standards of the Japanese power grid. This experience further enhanced my skill set and expertise to work on diverse energy projects in the future.

In addition, the internship allowed me to experience Japanese culture while living and working in Nagoya. Through Japanese language classes, I learned to read and write in Hiragana and Katakana, along with the basic reading and writing structure of Japanese.

Since Nagoya is centrally located in Japan, I was able to take advantage of the Shinkansen network of high speed trains to visit the nearby cities of Tokyo, Kyoto, and Osaka during down time and weekends. The areas around Nagoya are also beautiful, such as Yoro, Himakajima, and Hamamatsu, which are serviced by the regional JR lines. After the program, I will be traveling to Hiroshima and Kyushu before heading back to the US to finish my degree.

The JUACEP staff did a fantastic job in planning and executing all the logistics for the trip, including excursions and hands-on learning activities. All formalities including visa, housing, and university registration were handled efficiently.

The technical and cultural experience will be invaluable in my future career as I would like to work internationally on projects related to the development of renewable energy technologies. I expect that my career will allow me to return to Japan in the future, and I hope to be back soon!

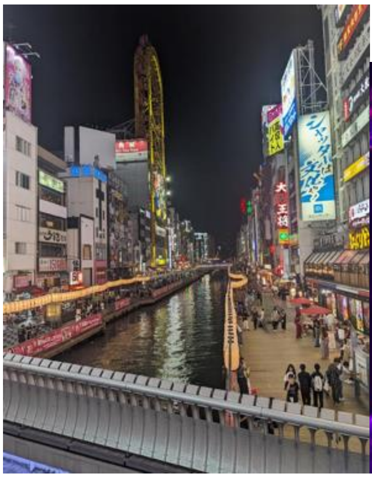

An Unforgettable Chapter of my Life

Name: Utkarsh Prakash Srivastava
Affiliation at home country: Department of Electrical and Computer Engineering, New York University
Participated program: Summer Course 2024

Research theme: Region of Interest based Medical Image Compression
Advisor at Nagoya Univ: Prof. Toshiaki Fujii
Affiliation at Nagoya Univ.: Department of Information and Communication Engineering

Researching at Nagoya University, Japan, has been an extraordinary and enriching experience. Visiting Japan has been a long-time dream of mine, and spending ten weeks here has surpassed all my expectations. Immersing myself in Japanese culture, I have gained insights and experiences far beyond what any tourist could. The discipline, respect, and intricate traditions of Japanese culture have left me in awe.

Moreover, my lab at Nagoya University has been incredibly welcoming. The atmosphere in the lab, fostered by both professors and students, is unlike any other lab I have previously worked in. The environment is collaborative and supportive, with everyone contributing to a positive and productive work atmosphere. The kindness and camaraderie of the people here, always accompanied by laughter and good spirits, have made my time in the lab enjoyable and fulfilling. My labmates have become not only colleagues but friends, sharing both professional and personal experiences that have enriched my time here, whether in the lab or exploring the wonders of Japan together.

Overall, this journey has been a blend of professional growth and cultural discovery, making it an unforgettable chapter in my life.

Findings through JUACEP

Name: Luna Xiaoyue Wu
Affiliation at home country: Department of Mechanical Engineering, University of Michigan, Ann Arbor, USA
Participated program: JUACEP Summer 2024

Research theme: Optimization of Robust Lidar SLAM framework for Predictive World Modeling Integration
Advisor at Nagoya Univ: Prof. Kazuya Takeda, Prof. Keisuke Fujii
Affiliation at Nagoya Univ.: Graduate School of Informatics, Nagoya University, Nagoya, Japan

Before coming to Japan, I had research experience in robotics and a strong interest in robot perception and Simultaneous Localization and Mapping (SLAM). However, my practical experience was limited to lecture slides. The University of Michigan is renowned for automotive research, and I knew Nagoya University was a top institution in Japan for transportation and automotive science. Over the past ten weeks, I gained extensive knowledge of 3D LiDAR SLAM both academically and practically. My research aimed to identify a suitable SLAM framework for a VAE predictive world model for road environments. I experimented with various SLAM frameworks in ROS 2 (Robot Operating System 2) and learned about the performance differences between ICP (Iterative Closest Point) and NDT (Normal Distributions Transform) scan matching.

During my research, I received tremendous support from my colleagues in the driver behavior group. Prof. Alexander Carballo provided invaluable guidance on SLAM, while Prof. Kento Ohtani from the machine learning group helped me settle into the lab. Thanks to Prof. Takeda and Prof. Ohtani, I also visited Map IV, a leading company in robotic mapping, where I received valuable advice on the SLAM framework I used.

For the excursion, the Toyota Commemorative Museum is my favorite. Staff explained functional sewing machines in detail, where some of them are over 90 years old. I learned how a car is being manufactured from the production line. As a student from Detroit the automotive city, I was thrilled to see huge molding machines running and robot arms soldering car parts.

Before arriving, I had heard that Nagoya was one of Japan's less exciting cities. However, I found its slower pace, lower living expenses, and convenient location between Tokaido and Kansai (Kyoto-Osaka) very appealing. Thanks to the Shinkansen, I visited various destinations like the Arashiyama bamboo forest in Kyoto, Uji's matcha parfaits, Toshodai-ji in Nara, the Hakone shrine, and Tokyo Disney Sea. In Nagoya, I enjoyed shopping in Osu, relaxing in Ozone onsen, and visiting nearby beaches with fellow JUACEP participants.

My experience in Japan has deepened my interest in pursuing a career here. I appreciate the respect for time and boundaries in Japanese work culture, which contrasts with the outgoing culture in the US. I am more determined to explore career opportunities in Japan, maybe starting with a Japanese internship next summer. I am grateful to Prof. Kazuya Takeda, Prof. Keisuke Fujii and the JUACEP staff for making this experience possible. I have been granted such a valuable and productive summer, and it’s been a rewarding and unforgettable journey.

4-2. Questionnaires

For Q1-4, we asked the same questions BEFORE and AFTER the program.

Q.1: Are you interested in studying at a Japanese university for PhD?

Q.2: Are you interested in working at a Japanese company in USA?

Q.3: Are you interested in working at a Japanese company in Japan?

Q.4: Are you interested in working at a non-Japanese company in Japan?

Q.5: Which activity did you like? ('Research internship', 'Field trip', 'Engine assembly', 'Japanese course', others)

- I enjoyed all of the JUACEP programs. I particularly enjoyed the excursion and the opportunity to see the different museums and facilities of Japan.
- I like all Research internship, field trip, engine workshop and Japanese class.
- I think that as someone with basic Japanese knowledge, a more advanced Japanese class would have been more beneficial to me [I did not take the Japanese lecture].
- I found the engine dis/assembly to be an enjoyable experience. The hands-on aspect and demonstration allowed for an in-depth view on how engines work that is not usually available in other settings.
- The research internship was a unique experience that is a good mix of a short introduction into a new field and a lengthy project that provides the student with responsibility and growth in their research skills.
- The thing I disliked was the Japanese classes. I dropped after two sessions. This is purely subjective. It doesn't mean that the professor is bad. It was just difficult for me to master all the alphabet syllables. What's more, I think that five weeks of Japanese classes is far from enough.
- Engine workshop was a fun!
- The Japanese classes were a bit difficult to understand as a beginner studying Japanese.

Q.6: In what did you find difficulty? What could be improved? (Excerpts)

- I didn't find any difficulty.
- I found it very difficult to make local friends at the university, even in my own laboratory. I think if there were a couple more organized activities where Japanese students are encouraged to join, it would help students like me make more meaningful connections.
- I think the field trip was a little bit rushed which caused us to be unable to finish all of the activities. Perhaps better planning or schedule management would allow for all the activities to be experienced in the fullest.
- There was a language barrier between me and my laboratory mates. They I could communicate except with a few of them. I hope that the university emphasizes on the foreign language learning and especially the English language.
- I found communicating with my lab mates a little difficult, but it is understandable because my Japanese language skills are very poor.
- The JUACEP office should consider offering courses during all the 10 weeks of the internship. In addition to that, I consider a 10-week internship short. I couldn't even get credits from my university because the minimum number of weeks for an internship is 13.
- I felt as if the Japanese class could have held more sessions and started earlier. It would have been beneficial to know more basic phrases coming in.
- I enjoyed the program very much, my lab was very welcoming and accommodating and I am very proud of what I have accomplished with their help. I enjoyed the field trips a lot as well, I wish we could have had more social events although I understand it may not fit the budget.
- All the programs were great! It would be nice if we could have picked the type of workshop we had as not all of us are mechanical engineering.
- Thank you for the opportunity! I greatly enjoyed my time here.

- The difficulty I faced was to find a proper research topic. The main reason for that was because I chose a subject I wanted to learn about, which limited the topics my advisor could give me. In the end, I was able to find a topic that would be meaningful.
- A challenge I personally faced was going to the hospital. I was lucky enough to be surrounded by competent beings, such as the nice lady in charge of the residence, the RA in duty that night, and a friend I made in the members of the program, Jake, that spoke Japanese, that took me to the hospital and helped me to get an appointment and to endure the night in the waiting room. Something that could be improved, would be to facilitate the link between our home insurance and the hospital, as it was difficult to get everything I needed to get reimbursed by my insurance. At the moment of writing this, I still don't have the proper documents.
- I found learning Japanese to be difficult, but the class was still very beneficial to me. I certainly did not leave Japan fluent, but I knew enough to communicate generally and ask basic questions. I enjoyed all the programs of JUACEP and do not think any part needs improvement.
- I think most issues would relate to my own inability to speak Japanese so overall things were not too difficult. At times, the availability of the host professor may be limited but there is only so much one can do along those lines.
- Engine dis/assembly was fun and exciting but since It was not something from my domain, I believe we could have added more activities from different domains as well.
- I enjoyed very much "Innovation Expo 2024" I took part in with my lab members in Tokyo, though this wasn't in the program.
- I hope the time span of the program can be given longer, for example for three or three and a half solid months, which allows the fellow to produce better research results, two months is a bit short before we fully understand the different lab settings and get ourselves into the research environment. I hope the Japanese class can be given with different difficulties, since the class provided is too easy for me, but I also wanted to learn higher level Japanese, however such option was not granted like the NUSIP program, where students were sorted with different Japanese level.

Q.7: Write comments freely.

- I think it would have been nice to be able to connect with students who are in the program beforehand.
- Overall, I think there was a healthy balance between structure and freedom within the program and academic responsibilities.
- Thank you very much for your hospitality and kindness in Japan! I wish the JUACEP team all the best in the future.
- Overall, I really liked the JUACEP program. I enjoyed every bit of it. Thank you so much.
- I would like to express my gratitude to Professors, Researchers, TA and my colleagues of the Behavior Signal Processing Lab for giving me the opportunity to participate in the JUACEP program. Throughout this experience, I learned a great deal about 3D LiDAR SLAM and gained valuable knowledge from both an academic and practical industry perspective.
- Thank you so much to everyone that organized the program, especially Dana and Tomoko for helping me apply to the program and adjusting well to the life here. I have enjoyed Japan and the program so much! THANK YOU!!!!

<5> Appendices

5-1. Photo collection

Orientations and Welcome Banquet, June 3 and 17

Meet up, June 20

Visitor from IPE, U. Michigan,
June 21

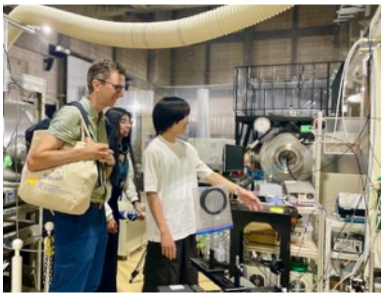

Japanese Language Class, June 18 - July 18

Excursion: JERA Park, Mizukan Museum, Toyota Commemorative Museum, June 28

Engine Workshop, July 5 & 8

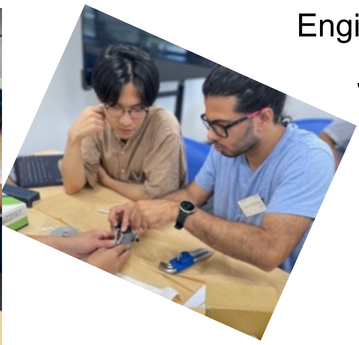

Final Workshops and Closing Ceremony, August 8 and 28

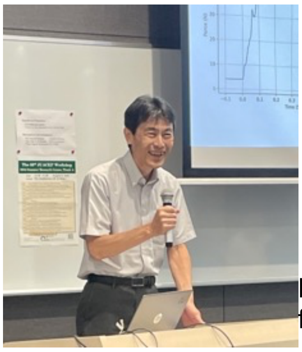

Encouraging message from Dean Prof. Kobashi

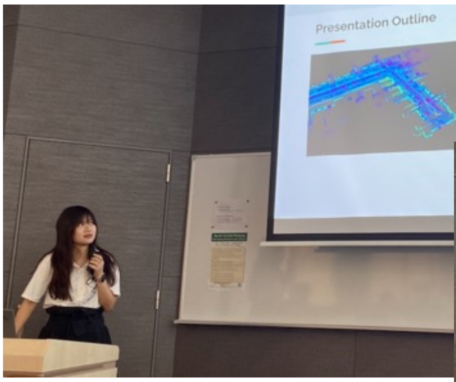

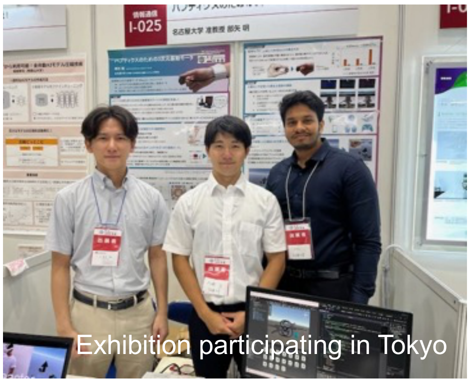

Exhibition participating in Tokyo

5-2. Building Locations

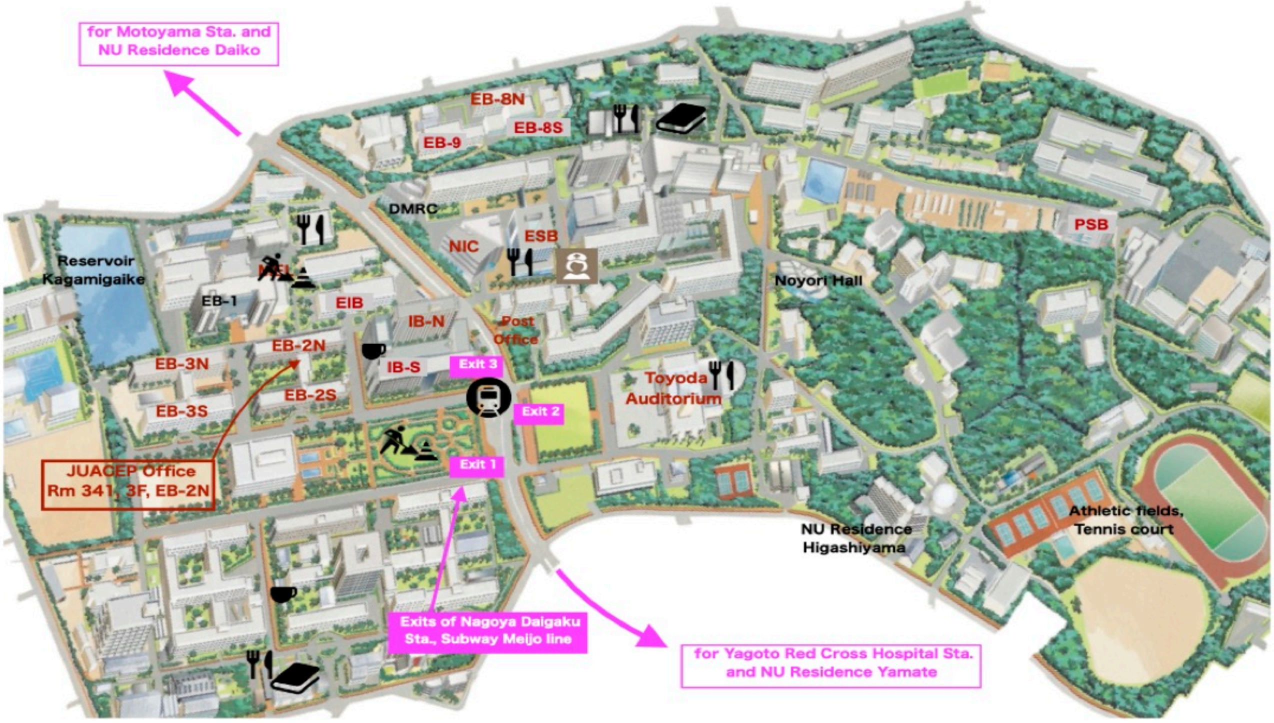

Bldg. icon on the map	Building name (in Japanese)	Important places for JUACEP	Lab locations for JUACEP students
EB-2N	Engineering Building 2 North (Kougakubu ni-gou-kan, Kita)	･JUACEP Office, Room 341, 3F for Stipend on July 3 & Aug. 4 ･Round-table Discussion on June 27 at Room 347, 3F	Matsumoto Lab, 3F, forArthur
EB-2S	Engineering Building 2 South (Kougakubu ni-gou-kan, Minami)		Hara Lab, 4F for Enzo
EB-3S	Engineering Building 3 South (Kougakubu san-gou-kan, Minami)	Japanese class at Room 572, 5F	Sogabe Lab, 4F for Mohamed
EB-9	Engineering Building 9 (Kougakubu kiu-gou-kan)		Tsubaki Lab, 2F for Herman
IB-N	Integrated Building North (IB Kita-kan)		Iwata Lab, 9F for Vi
IB-S	Integrated Building South (IB Minami-kan)		Ogawa Lab, GF for Catherine
PSB	Pharmaceutical Science Building		Kato Lab, 3F, for Hanane
ESB	Engineering & Science Building (E-S kan)	Orientations of June 2&16 at ES Conference Room, GF	
EIB	Emergent/Innovative Building (E-I kan)	Hands-on Execises, July 10, Creation Plaza, 201, 2F	
Toyoda Auditorium (Toyoda koudou)		Meeting point for the Field Trip, July 27, 9:00am	
Post Office		Money withdrawal, Postal affairs	
🍴	Cafeteria/Convenience Shop		
☕	Café		
📕	Book Store		
🚇	Subway Station	Nagoya Univ.: Nagoya Daigaku Sta. Dormitory Daiko: Sunadabashi Sta.	
⚕	Health Administration Office	Open hours: 9:00-12:00, 13:00-17:00, Mon.-Fri. (052)789-3970	

5-3. Mandatory Deliverables

★ All of following templates can be downloadable at
https://www.juacep.engg.nagoya-u.ac.jp/downloads/index.html

1. JUACEP Independent research report

See *Appendix-1.*
Deadline: **August 10, 2023 for Track A**
August 30, 2023 for Track B
Send to… office@juacep.engg.nagoya-u.ac.jp

2. JUACEP Research presentation slides

We will collect the PowerPoint/PDF slides at the workshop site on **August 9 from Track A students** and **August 25 from Track B students**. Also, we would appreciate you sending us a backup copy beforehand.

Evaluation: your final score is calculated by the points of the research report (1~50pts.) and the presentation at the workshop (1~50pts.) evaluated by your Nagoya Supervisor.

You will be officially awarded credits from Nagoya University and the transcript to be airmailed to your home university in September 2023.

A$^+$: 100~95
A : 94~80
B : 79~70
C : 69~65
C$^-$: 64~60
F(fail) : 59~0

Important:

(a) JUACEP will publish the participants' research reports and the presentation slides on the website and booklet. When you submit the report, Please LET US KNOW IF YOUR SUPERVISOR PERMITS THE PUBLICATION.
(b) If you are planning to transfer the credits, kindly discuss it with your home university office and submit the transcript to JUACEP Office.

3. Findings through JUACEP

See *Appendix-2.*
Deadline: **August 10, 2023 for Track A**
August 30, 2023 for Track B
Send to… office@juacep.engg.nagoya-u.ac.jp
Please write freely about your experience in Japan inserting pictures.

4. JASSO Scholarship obligatory questionnaires, H-1

See *Appendix-3.* There are "Pre-arrival" part which you already submitted and "After the program" part which you have to submit until **August 9 (Track A)** or **August 25 (Track B)**.
Send to… office@juacep.engg.nagoya-u.ac.jp

＊Please note that all program participants will be processed at the same time, so late submission will affect the certification process for others.

5-4. Campus Life Information

[Housing]

International Residence Daiko (on Daiko campus)

Address: 1-1-18, Daiko Minami, Higashi-ku, Nagoya 461-0047, Japan
Office Phone: (052)737-8470
Resident Assistant office: rm. 228
WiFi is available.
Please follow the residential guidelines.

[NU ID & information security]

Student ID Card

A student ID card is issued upon your arrival. You can use the university libraries with it. The card lets you get student discounts at museums, theatres and so on. This card is delivered at the orientation.

Internet on Campus

Wireless Internet connection (NUWNET) is available on campus as far as your Nagoya University ID is valid. To connect, at the beginning you have to access to 'Information and Communications Headquarters' <*https://ist.nagoya-u.ac.jp/portal* > using your ID and a default password that are shown in a sealed card delivered at the orientation, then take the online "Information Security Training" and "Information Security Check". To pass the check, you must score at least 80% or repeat the test until you clear 80%. Please do all of required steps described in the web like changing password, otherwise acquired wireless connection will be expired in a week.
See: *https://ist.nagoya-u.ac.jp/*

University Security Department Warning

Copyright infringement using P2P software is prohibited. University has been strongly warning to all of faculty, staff and students not to use P2P software like Gntella, Share, Winny, WinMX, Xunlei, and so on. It can be easily detected and reflects discredit on University and oneself who used it.
Please never use P2P in University, nor PC in which P2P is installed accessing to University network. You will be detected and warned.

[Everyday Life]

Refuse Disposal at Nagoya University

A sorting system for refuse disposal is used at Nagoya University. There are trash bins for "combustible refuse", "incombustible refuse", and recycle bins for "empty bottles", "empty cans", and "PET bottles" all over campus. Recycle companies collect papers and magazines. Used paper products such as used copy paper are collected and recycled. Students are kindly requested to be mindful when they throw away their rubbish and to use the correct bins to help waste reduction and the reuse of recyclable materials.
Also please follow the manners ruled in each laboratory.

Public Transportation of Nagoya City

1. MANACA マナカ is a pre-paid IC card that can be used for subway/ city bus/ most of train companies through Japan. It is also used at many shops, vending machines, restaurants, and so on.
2. The Student/Commuter Railway Pass allows you to take unlimited rides between stations on the specified route. (Only the person registered on the card may use this pass.)
   We recommend to purchase it or add it to your Manaca at a subway station counter by filling out a form and presenting your Student ID Card.
   A 3-month Student Railway pass between *Nagoya Daigaku* station and *Sunada-Bashi* or *Nagoya Dome-mae Yada* station will cost you JPY 15,680 (for your reference, round trip will cost you JPY 480 daily.)
3. ONE-DAY TICKETS allow for unlimited rides of city traffic for a day. One-day tickets for all bus, subway, and bus & subway routes are available. Ticket, Donichi-Eco-Kippu, that can be used on Saturdays, Sundays, holidays and the 8th of every month can be also purchased. These tickets include a discounted admission fee for some tourist facilities in Nagoya city such as Nagoya Castle or the Tokugawa Museum.
   They can be purchased at any subway station. For further information, refer to the website:
   http://www.kotsu.city.nagoya.jp/

(3) Besides the city-running transportation, trains and buses of JR, Meitetsu, Kintetsu, Aonami-sen will make your passage easier in/around Nagoya City.

Useful Links:

The following websites provide information on available transport services, time-tables, etc. HYPERDIA: *http://www.hyperdia.com/en/*

If involved in a Traffic Accident.

If you are involved in a traffic accident, remain calm and do the following:

1. Dial 119 for an ambulance.
2. Move any dangerous including vehicles, off the road to prevent other accidents.
3. Report the accident immediately, even if it is small, to a nearby police station and obtain a report of the accident.
4. Write down the license plate number of the car concerned as well as the name, address and age of the driver, after requesting to see his/her driver's license.
5. If there are witnesses, write down their names, addresses and telephone numbers.
6. Make detailed notes of the accident and take photographs, if possible.
7. See a doctor, even if you think that you are all right, because sometimes symptoms can take time to occur.
8. Consult your insurance company as soon as possible.

Smartphone zombies often cause accidents. Many cases are especially happened between bikers and walkers and some come fatal. Refrain from using mobile during walking.

Compliance with Japanese Law

During your stay in Japan, anyone who commits a crime, misdemeanor or any other illegal act, will be subject to legal procedures according to Japanese Law. Nagoya University also takes strict disciplinary measures against such person, and may expel the person from university.

1. Prohibition of Narcotics

   In Japan, the possession and sale, for personal use or otherwise, of all narcotics and any illegal substances are strictly prohibited. If offered, refuse them. If leaving Japan temporarily, never agree to look after a stranger's luggage at the airport.
2. Drinking and Smoking Restrictions

   In Japan, people aged under 20 are not allowed to drink or smoke. Smoking is not allowed in many places, including stations, public facilities and within the campus. Nagoya city has special zones where smoking on the street is banned. If found smoking there, you will be fined.

   Driving a car, riding a motorcycle or bicycle after drinking any amount of alcohol is a serious offence in Japan, and can also cause accidents. Never drive after drinking. Those who accept a ride in a car that is driven by a drunk driver or those who offer alcohol to a driver are all subject to punishment under Japanese law.
3. Others

   Whilst inside a shop, removing product wrapper and price tag or putting product into the pocket or the bag before actually paying for them are easily treated as a shoplift in Japan. Talking loudly on the street in the midnight should be refrain.

Safety Guide

Japan is not as safe as most people think. There is the risk of crime anywhere in the world, including Japan. Please pay attention to safety and security for yourself and your belongings in any scenes as you do in the US.

Culture Shock

Although "culture shock" is generally understood as a temporary shock felt when confronted by different cultural customs, ways of thinking and behavior patterns, it actually refers to a psychological state of depression caused by a succession of failure experiences in unfamiliar social situations. Culture shock is temporary, and everybody goes through it to some extent in the process of cultural adaptation. General symptoms of culture shock include negative feelings such as: losing self- confidence, feeling depressed, attributing all failure to yourself, feeling that nobody understands you, feeling inadequate, etc. Accordingly, you may lose all motivation to talk with Japanese people or to attend classes. Most of these psychological reactions are, again, very natural in the process of cultural adaptation. Please take time to cope with each single event in your life and to talk with friends, teammates and supervisor, and you will be able to overcome these emotions sooner or later.

Differences in "Academic Culture"

It is widely accepted that different values, behavioral and communication patterns exist from culture to culture. However, we often fail to realize that there are also differences in “academic culture”, such as expected roles of academic advisers and students, classroom communication, evaluation criteria, etc. Such differences can also be a major cause of your stress. For example, the relationship between academic adviser and advisee is considered particularly important at the graduate level education in Japan. Some knowledge of the Japanese academic culture will help you achieve your goal more smoothly.

Cope with Stress

If you feel pressured by stress or lose confidence in your ability to study, you should think about releasing yourself from these negative emotions. Achieving good results in your studies may take a certain amount of time, and ought to be views as accumulative process. Sometimes, you will need to take a break. If you feel tired, do not push yourself too hard and try to enjoy some of your favorite foods, recreation, and physical exercise. It is also recommended that you talk with your friends, academic adviser, or international students’ advisors/counselors. Moreover, please do not consider the process of cultural adaptation solely as a cause of stress; you can learn tremendously about various cultures, including your own, from this process.

<Visit the Global Engagement Center Support Team (Advising & Counseling Services)>

If you feel that you cannot deal with stress or feel a sense of isolation or frustration, do not hesitate to ask for help from international counselors at the Global Engagement Center Support Team. There is an international student counselor who will support your personal and psychological concerns. A discussion with an international student counselor can help achieve a useful perspective on culture shock and insights into Japanese culture.

Global Engagement Center Support Team (7th floor, West Wing of IB Bldg.)
https://acs.iee.nagoya-u.ac.jp

Harassment

Nagoya University has set up a Harassment Consultation Center to prevent and eliminate the occurrence of any kinds of harassment, such as sexual harassment and academic harassment. Professional counselors deal with inquiries with utmost respect for their clients’ feelings and wishes. For English language consultation, you may visit the representative at the Education Center for International Students (ECIS). All consultation will be kept confidential.

Nagoya University Harassment Consultation Center (Appointments by fax or E-mail)
Tel: (052) 789-5806 (9:30-16:00)
Fax: (052) 789-5968
sh-help@adm.nagoya-u.ac.jp
http://www.sh-help.provost.nagoya-u.ac.jp/english.html
Contact person at each School (including ECIS)

[Medical & Health Care]

Medical Services

If you suffer from continuous headaches, a loss of appetite, or you cannot sleep well, etc., you should seek the advice of a doctor before the condition gets serious. These symptoms may be signs of fatigue or exhaustion. They may also be psychological or psychosomatic symptoms, which are treatable by specialist doctors. In addition to taking care of your own health, please pay attention to your friends' health and encourage them to see a doctor, if they are feeling unwell.

(1) The Health Administration Office See Building Location map.

Students can undergo physical examinations, receive health advice, first-aid and arrange psychiatric counseling at this facility. There is no charge for using any of these services.

Appointments are necessary for psychiatric counseling services. Please call the office,
Tel: (052) 789-3970 or email to hokekan@htc.nagoya-u.ac.jp

[Office Hours for Health Services]

Treatment	Time	Mon	Tue	Wed	Thu	Fri
Physical Examinations & First-Aid	10:00 - 11:30	○	○	○	○	○
	13:30 - 16:30	○	○	○	○	○
Psychiatric Counseling	10:00 - 12:00	○	○	○	○	○
	13:30 - 16:30	○	○	-	○	○

(2) Calling an Ambulance

Telephone 119 or press the RED button on a public phone for connection. Free of charge.
This number is also used for requesting fire engine.

Precautions for Food Poisoning and Infectious Diseases

Great care should be taken with regard to eating habits during the extreme summer weather in Japan. To avoid food spoilage, check the expiration date before buying food, apply heat to raw foods and be careful not to keep food in the refrigerator for an excessive amount of time. To guard against food poisoning, always wash culinary items with hot water.
Also follow the basic hygienic rules to avoid being infected.
World Health organization: http://www.who.int/en/

[Hospitals around Nagoya University]

Nagoya Daini Red Cross Hospial (Yagoto Nisseki)	Address: 2-9 Myoken-cho, Showa-ku, Nagoya Tel: (052) 832-1121 Mon-Fri: 8:00-11:00 Closed on Sat, Sun, holidays
Watanabe Clinic [Internal medicine]	Address: 2F Nihonchouzai Yamate-dori Bldg, 3-8-1 Yamate-dori, Showa-ku, Nagoya Tel: (052) 861-3450 Mon-Sat: 9:00-12:00 Mon, Wed-Fri: 16:00-18:00 Closed on Sun, holidays
Kai Clinic [Internal medicine, Urology]	Address: 32-2 Myoken-cho, Shouwa-ku, Nagoya Tel: (052) 836-9136 Mon-Sat: 9:00-12:00 Mon-Wed, Fri: 18:00-20:30 Closed on Sun, holidays
Yamate Dermatologist	Address: 2F Habitacion Yamate, 2-9-1 Yamate-dori, Showa-ku Tel: (052) 836-4115 Mon, Tue, Thu-Sat: 9:30-12:30 Mon, Tue, Thu, Fri: 16:30-19:30 Sat: 14:30-17:30 Closed on Wed, Sun, holidays
Fujimi Dentist	Address: 139 Yagotohujimi, Showa-ku, Nagoya Tel: (052) 835-3200 Mon-Wed, Fri, Sat: 9:30-12:30 Mon-Wed, Fri, Sat: 14:00-19:00 Closed on Thu, Sun, holidays

Published in December 2024

Japan-US-Canada Advanced Collaborative Education Program (JUACEP)
Graduate School of Engineering
Nagoya University
Furo-cho, Chikusa-ku, Nagoya 464-8603, Japan
office@juacep.engg.nagoya-u.ac.jp
https://www.juacep.engg.nagoya-u.ac.jp